High-Fidelity Determination of Nuclide Inventories for Radioactive Waste Disposal

Thèse N° 8960

Présentée le 1er mars 2019

à la Faculté des sciences de base
Laboratoire de physique des réacteurs et de comportement des systèmes
Programme doctoral en energie

pour l’obtention du grade de Docteur ès Sciences

par

Valentyn BYKOV

Acceptée sur proposition du jury

Prof. S. Haussener, présidente du jury
Prof. A. Pautz, Dr B. Volmert, directeurs de thèse
Dr S. Mosher, rapporteur
Dr A. Vasiliev, rapporteur
Prof. H.-M. Prasser, rapporteur

2019

ÉCOLE POLYTECHNIQUE
FÉDÉRALE DE LAUSANNE

Valentyn Bykov
https://orcid.org/0000-0003-4726-1868
@ valentyn@vbykov.eu

VERSION INFO
Final release version.
Last update 2019-01-12

TEMPLATE
This thesis was created using the template ArsClassica, Lorenzo Pantieri's reworking of the ClassicThesis style designed by André Miede, inspired by *The Elements of Typographic Style* by Robert Bringhurst.

This thesis is dedicated to PhD students everywhere,
past, current, and future;
to those who have struggled, yet still finished,
and those who have not.

Dawn snuffs out star's spent wick
Even as love's dear fools cry evergreen,
And a languor of wax congeals the vein
No matter how fiercely lit; staunch contracts break
And recoil in the altering light: the radiant limb
Blows ash in each lover's eye; the ardent look
Blackens flesh to bone and devours them.
(Silvia Plath, "Epitaph For Fire And Flower")

What men must know, a boy must learn.
(Mike Krahulik and Jerry Holkins, "Lookouts")

ACKNOWLEDGMENTS

I would like to acknowledge those without whom this thesis and the work contained therein would not be possible.

First and foremost, I would like to sincerely thank Andreas Pautz and Ben Volmert for enabling this thesis and offering their valuable supervision and support.

Big thanks goes also to Sophia Haussener, Scott Mosher, Micha-Horst Prasser, and Alexander Vasiliev for agreeing to be serve on the jury for my defense.

A very *special* thanks goes to Manuel Pantelias, whose work and ideas were at the root of the many developments described in this thesis.

I would also like to recognize the support received from Erwin Neukäter, Denis Ablondi, and Frank Holzgrewe of BKW, Jörg Thiess of IGN Consult, and from Alejandro Noël, Teo Simeonov, Aydin Bashe, and Tamer Bahadir of Studsvik.

Stefano Caruso and Ahmed Shama, who have together taught me a great deal about SCALE and fuel calculations, and were always ready to offer advice.

The *big bosses* Harald Maxeiner (of Nagra) and Hakim Ferroukhi (of PSI) who supported this work in managerial, but also advisory capacity.

All whose work complimented this thesis work, specifically Alessandro Scolaro, Paolo Pisano, Aurelio Sulser, Stefano Canepa, Alexander Vasiliev, as well as Daniel Siefman, Valerio Ariu, and Marianna Papadionysiou.

The University of Illinois at Urbana-Champaign staff and professors, especially Rizwan Uddin (for mathematic problem-solving skills) and Stoyan Toshkov (for non-mathematical problem solving skills), for preparing me for all this.

A big, heartfelt thanks goes to my family for supporting all these adventures around the world.

Of course, this work would not be possible without the brilliant, strong, resourceful, and incredibly hard-working *Sisterhood* of Zelda, Alison, Betty, Cindy, Dory, Erika, Frida, Grace, but also Cassandra and Saskia.

I would also like to acknowledge the positive influence of role-playing games, which taught me how to simultaneously juggle a large number of projects, while also keeping track of the big picture and the many characters therein (each with their own personal agendas).

Last but not least, numerous numerous thanks go to EPFL as a whole for encouraging me to complete my PhD by sharing my university e-mail address with every possible student association, making graduation the only way to stop receiving over a dozen unsolicited e-mails every day.

ABSTRACT

The general license application (RBG) for the Swiss deep geological repository will be submitted in 2024. Furthermore, the decommissioning of the nuclear power plants (NPPs) is coming soon, with the Mühleberg NPP (KKM) scheduled to shut down in 2019. In support of the associated analyses and planning, availability of accurate descriptions of the nuclear waste streams is of paramount importance.

The work described in this thesis represents a significant improvement of Nagra's most important radioactive waste characterization methodologies: for spent fuel, NPP decommissioning waste, and reactor waste. The resulting high-fidelity nuclide inventories will decisively support the future waste disposal research and development, as well as serve the NPP decommissioning planning in general.

The spent fuel characterization demonstrated is based on Polaris. This approach is compared against the code sequence used in the industry (Studsvik CMS), in order to confirm that, when the necessary fuel data is available, either one of these codes can be used to provide detailed nuclide vector for the spent fuel. Afterwards, possible ways to produce the desired nuclide vectors in the future are identified.

For decommissioning waste, every step of the old characterization methodology has been further developed and improved upon. This includes a new, detailed, fully three-dimensional approach to NPP modeling and the development of a new activation sequence (based on the ORIGEN depletion solver), which outputs a highly-resolved component-wise activation distribution and visualization. Additionally, the methodology is extended to apply the method's results for algorithm-optimized packaging concepts and waste volume minimization through decay storage and free release analyses. At the end, recommendations for the future improvements are presented.

The decommissioning waste characterization methodology is then expanded to accommodate reactor waste, and the more complex nature of the non-stationary components of this waste stream (such as the control rods). A systematic general approach, based additionally on the component dose rate measurements, allows for a more efficient and flexible characterization of all reactor waste.

These developments serve as an important foundation in the ongoing transition from a conservative approach towards a best-estimate plus uncertainty (BEPU) waste characterization, which is vital for accurate safety analysis studies, as well as waste and cost minimization.

The results produced by these methodologies will form the basis for the next version of MIRAM (the Swiss Model Inventory of Radioactive Materials), MIRAM2020, which is to be used for the RBG. They will also be used as part of the next Swiss NPP decommissioning cost study, KS2021. At the same time, the obtained results are already being provided to the Swiss NPPs planning their decommissioning, specifically KKM and Beznau (KKB), allowing detailed component-wise segmentation strategies and packaging concepts decision making, finally leading to notable cost reduction for the utilities.

KEYWORDS:
component-wise characterization, cost study, decay storage, MCNP, neutron activation, NPP decommissioning, nuclear power plant, ORIGEN, packaging concept, Polaris, radioactive waste, SCALE, segmentation strategy, waste characterization, waste disposal, waste minimization

ZUSAMMENFASSUNG

Das Rahmenbewilligungsgesuch (RBG) für das geologische Tiefenlager für radioaktive Abfälle der Schweiz wird voraussichtlich 2024 eingereicht. Zudem wird schon bald, Ende 2019, mit Mühleberg (KKM) das erste Kernkraftwerk (KKW) endgültig seinen Leistungsbetrieb einstellen und damit die Stilllegung für kommerzielle KKW in der Schweiz einleiten. Vor diesem Hintergrund ist es von hoher Relevanz, über eine möglichst akkurate Beschreibung der resultierenden radiologischen Abfälle zu verfügen.

Die vorliegende Arbeit stellt eine massgebliche Verbesserung der bisherigen Methoden zur Abfallcharakterisierung der Nagra (Nationale Genossenschaft zur Lagerung radioaktiver Abfälle) für die drei wichtigsten Abfallkategorien dar: abgebrannte Brennelemente (BE), KKW-Stilllegungsabfälle und Reaktorabfälle. Die neu ermittelten, resultierenden Nuklidinventare fallen für alle Abfallkategorien erheblich realistischer aus. Sie unterstützen damit entscheidend die Forschung der nuklearen Entsorgung und stellen zudem eine wichtige, generelle Planungsgrundlage für die KKW-Stilllegung dar.

Die vorgestellte Charakterisierungsmethode für die abgebrannten Brennelemente basiert auf Polaris. Diese Methode wird derjenigen in der Industrie verwendeten Rechensystematik (Studsvik CMS) gegenübergestellt. Hierdurch wird bestätigt, dass generell beide Ansätze – sofern die nötigen BE-Daten zur Verfügung stehen – adäquat sind, um die gewünschten realistischen Nuklidinventare zu ermitteln. Anschliessend daran werden die verschiedenen Wege, diese Nuklidinventare zu ermitteln, im Detail identifiziert.

Die bisherige Methode für die Charakterisierung der Stilllegungsabfälle wurde in jedem relevanten Aspekt weiterentwickelt und verbessert. Hierzu zählt der detaillierte und komplett drei-dimensionale KKW-Modellierungsansatz, der seinerseits gekoppelt ist an eine neue Aktivierungssequenz (basierend auf dem ORIGEN-Abbrandprogramm). Damit wird eine komponentenweise, hochaufgelöste Bilanzierung und Visualisierung der Aktivierungsverteilungen ermöglicht. Zudem werden die Resultate mittels eines Optimierungsalgorithmus in effiziente Verpackungskonzepte überführt, und vertiefte Analysen hinsichtlich Abfallminimierung unter Nutzung maximaler Freigabe und Abklinglagerungsstrategien ermöglicht. Am Ende werden Empfehlungen für die künftige Entwicklungspotentiale diskutiert.

Die o. g. Methode für die Charakterisierung der KKW-Stilllegungsabfälle wird zudem erweitert, um den besonderen und oft komplexen Ansprüchen der Kategorie der Reaktorabfälle gerecht werden zu können – hier insbesondere mit Blick auf die im Strahlungsfeld des Reaktorkerns beweglichen Komponenten (beispielsweise Steuerstäbe). Ein neuer systematischer Ansatz, der sich parallel auf komponentenweise Dosismessungen abstützt, erlaubt generell eine effizientere und flexiblere Charakterisierung der gesamten Rubrik des Reaktorabfalls.

Alle o. g. Weiterentwicklungen stellen eine wichtige Grundlage dar für die angestrebte Transformation von einer zumeist konservativen, radiologischen Charakterisierung hin zu einer Realistischen inkl. Unsicherheiten («best-estimate plus uncertainty» (BEPU)). Eine solche Transformation ist entscheidend für erfolgreiche und akkurate Sicherheitsanalysen sowie für effiziente Abfall- und Kostenminimierung.

Die durch obige Methoden erzielten Resultate werden den Grundstein für die nächste MIRAM-Version (das Schweizer «Modellhafte Inventar radioaktiver Materialien»), MIRAM-2020, bilden, auf die sich das kommende RBG für das geologische Tiefenlager abstützt. Zudem stellen sie einen signifikanten Teil der Datengrundlage für die nächste Schweizer KKW-Stilllegungs- und Entsorgungskostenstudien, KS-2021, dar. Parallel hierzu liefern die Resultate einen wichtigen Input für die Stilllegungsplanung, insbesondere für die Kernkraftwerke Mühleberg und Beznau (KKB). Sie dienen einer Entscheidungsgrundlage für die Entwicklung detaillierter Zerlege-Szenarien für Kerneinbauten, Druckbehälter und weitere Reaktorkomponenten, und ermöglichen letztendlich eine merkliche Kostenreduktion für die Betreiber.

SCHLÜSSELWÖRTER:
komponentenweise Charakterisierung, Kostenstudie, Abklinglagerung, MCNP, Neutronenaktivierung, KKW-Stilllegung, Kernkraftwerk, ORIGEN, Verpackungskonzept, Polaris, radioaktiver Abfall, SCALE, Zerlege-Strategie, Abfallcharakterisierung, Abfallentsorgung, Abfallminimierung

CONTENTS

LIST OF FIGURES

LIST OF TABLES

NOMENCLATURE

ADVANTG	Automated Variance Reduction Generator
ALGOPACK	Algorithm-Optimized Packaging
API	Application Programming Interface
ARP	Automated Rapid Processing
ATW	Alpha-toxic Waste
BA	Operational Waste
BE	Spent Fuel
BEPU	Best Estimate Plus Uncertainty
BEVA	SF/HLW Encapsulation Plant (see also OFA)
BOC	Beginning of Cycle
BWR	Boiling Water Reactor
C/M	Calculated / Measured (value)
CAD	Computer-Aided Design
CADIS	Consistent Adjoint-Driven Importance Sampling
CENTRM	Continuous Energy Transport Model
CERN	European Organization for Nuclear Research
CMFD	Coarse Mesh Finite Difference
CMS	(Studsvik) Core Management System
CPU	Central Processing Unit (of a computer)
CR	Control Rod
CSV	Comma-Separated Values
DXTRAN	Deterministic Transport
ELFB	Disposability Certificate
ENSI	Swiss Federal Nuclear Safety Inspectorate
EOC	End of Cycle
EOL	End of Life
EPFL	Swiss Federal Institute of Technology in Lausanne
ESC	Extended Step Characteristic
ETH(Z)	Swiss Federal Institute of Technology in Zürich
EW	Exempt Waste
FA	Fuel Assembly
FW-CADIS	Forward-Weighted CADIS
GSAM	Generic Sample Activation Model
HLW	High-Level Waste
HM	Heavy Metals (elements with proton number > 89)
I/LLW	Low and Intermediate Level Waste
IAEA	International Atomic Energy Agency
ILW	Intermediate Level Waste
IR	Intermediate Resonance
ISRAM	Information System on Radioactive Materials
KEG	Swiss Nuclear Energy Act
KEV	Nuclear Energy Ordinance
KGG	NPP Gundremmingen

KKB	NNP Beznau
KKG	NNP Gösgen
KKL	NPP Leibstadt
KKM	NPP Mühleberg
KS	Cost Study
LLW	Low Level Waste
LPRM	Local Power Range Monitor
LWR	Light Water Reactor
MCNP	Monte Carlo N-Particle Transport
MDA	Minimum Detectable Activity
meshtal	Mesh tally (output filename)
MIR	Medicine, Industry, Research
MIRAM	Model Inventory of Radioactive Materials
MOC	Middle of Cycle
MoC	Method-of-Characteristics
MOX	Mixed Oxide (Fuel)
Nagra	National Cooperative for the Disposal of Radioactive Waste
NEWT	New Transport Algorithm
NPP	Nuclear Power Plant
NRC	Nuclear Regulatory Commission
OFA	Surface Facility (see also BEVA)
ORIGAMI	ORIGEN Assembly Isotopics
ORIGEN	Oak Ridge Isotope Generation
ORNL	Oak Ridge National Laboratory
PMC	Produce Multigroup Cross sections
PSI	Paul Scherrer Institute
PWR	Pressurized Water Reactor
RA	(NPP) Reactor Waste
RBG	Application for the general license (for deep geological repository)
RCCA	Rod Cluster Control Assembly
RPD	Relative Percent Difference
RPV	Reactor Pressure Vessel
SA	Specific Activity
SA	Decommissioning Waste
SCALE	Standardized Computer Analyses Licensing Evaluation
SEFV	Ordinance on Decommissioning and Waste Management Fund
SF	Spent Fuel Assemblies
SGT	Sectoral Plan for Deep Geological Repositories
STENFO	Administrative Commission of the Decommissioning and Waste Disposal Funds
StSV	Radiological Protection Ordinance
TRITON	Transport Rigor Implemented with Time-dependent Operation for Neutronic depletion
UOX	Uranium Oxide (Fuel)
VLLW	Very Low Level Waste
VoV	Variance of Variance
VSLW	Very Short Lived Waste
VR	Variance Reduction

WA	Reprocessing Waste
WW	Weight Windows
WWG	Weight Window Generator
ZWILAG	Interim Storage Facility.

1 INTRODUCTION

Worldwide, there are 448 nuclear power reactors in operation (as of December 31, 2017), 64% of which are older than 30 years [1]. With the expected average lifetime being around 50 years, the International Energy Agency (IEA) expects a wave of nuclear reactor retirements in the following decades [2]. The administrative and technical actions performed in preparation for the closure of a nuclear power plan (NPP), as well as the actual dismantling of the facility and the subsequent removal of the regulatory controls from the facility are collectively referred to as *decommissioning* [3].

1.1 RESPONSIBILITY

The international law states that the generation which benefited from the power generated by the NPPs should bear the responsibility for the cost of waste disposal and the decommissioning process as a whole [4]. This follows the spirit of the *polluter pays principle* (found in environmental protection laws), which states that the parties responsible for waste and pollution are responsible for the effect on the environment. As such, waste producers are directly responsible for the costs associated with waste disposal. In Switzerland this applies to both conventional waste [5] and radioactive waste [6].

To cover the associated costs, the Swiss Nuclear Energy Act (KEG) [6] and the Ordinance on the Decommissioning and Waste Disposal Fund for Nuclear Facilities (SEFV) [7] require the waste producers to set up two funds: the Decommissioning Fund and the Waste Disposal Fund. These funds are supervised by the Administrative Commission of the Decommissioning and Waste Disposal Funds (STENFO) [8]. In order to ensure that the contributions to these funds are sufficient to cover the decommissioning and waste disposal costs, the cost predictions are reviewed every five years in so-called cost studies (KS). As of the writing of this thesis, the last cost study is KS2016 [9].

The majority of the waste comes from the NPPs. In Switzerland, there are four NPPs with five nuclear reactors in total. In (descending) order of age, these are: Beznau NPP (KKB) with two pressurized water reactors (PWR) producing 380 MW_e each, Mühleberg NPP (KKM) with one boiling water reactor (BWR) producing 372 MW_e, Gösgen NPP (KKG) with one 1020 MW_e PWR, and Leibstadt NPP (KKL) with one 1245 MW_e BWR.

Both decommissioning and waste disposal must be planned ahead of time. The decommissioning process is largely plant-specific, and as such is planned by each NPP operator individually. Waste disposal on the other hand is common for all waste producers, as all waste will be disposed together. For this reason the Swiss waste producers have in 1972 established a cooperative called *Nagra*—the Swiss National Cooperative for the Disposal of Radioactive Waste (*Nationale Genossenschaft für die Lagerung radioaktiver Abfälle*)—with the mandate to develop and implement the waste disposal solution. Specifically, to plan, construct, and operate two deep geological repositories —one for low and intermediate level waste (LLW and ILW, respectively), and one for high-level waste (HLW)—or one combined repository for all waste categories. The cooperative is composed of the nuclear power plant operators, interim waste storage facility ZWILAG, and the Swiss Confederation (representing waste producers from medicine, industry, and research (MIR)) [10].

1.2 RADIOACTIVE WASTE INVENTORIES

Within the scope of its mandate, Nagra performs characterization of radioactive materials in order to produce inventories of radioactive waste, as well as consult the waste producer on issues pertaining to waste conditioning (into forms suitable for deep geological disposal). These inventories are stored in a database called *ISRAM* (Information System on Radioactive Materials). Furthermore, ISRAM data is condensed to a certain degree and extended by modeled predictions for the future waste in a database system called *MIRAM* (Model Inventory of Radioactive Materials).

The waste in ISRAM and MIRAM inventories is divided in a number of different ways: radioactive waste categorization based on the Swiss laws, waste stream classification, and provenance classification.

The international radioactive waste categorization list, produced by IAEA [11], defines the following categories:

- Exempt waste (EW): Waste which meets the clearance or exemption criteria [12, 13] and is thus excluded from radiation protection regulatory control—that is, EW is not considered radioactive waste and is only included here for completeness.

- Very short lived waste (VSLW): Waste which can be placed in decay storage and within a few years would decay sufficiently to fall into the EW category.

- Very low level waste (VLLW): Waste which doesn't require significant isolation and as such can be disposed of in a manner similar to non-radioactive hazardous waste.

- Low level waste (LLW): Waste with low amount of long-lived radionuclides, which thus requires isolation in the order of hundreds of years, in engineered near-surface facilities.

- Intermediate level waste (ILW): Waste which contains significant amount of long-lived radionuclides, and therefore required a greater degree of isolation than LLW. That is, ILW is not suitable for near-surface facility disposal and must instead be disposed of underground. On the other hand, ILW doesn't produce significant amounts of heat.

- High level waste (HLW): Waste which contains large amount of long-lived radionuclides, or whose radiotoxicity generates significant amounts of decay heat.

These international categories have been adopted and adapted by the Swiss legislature, with the waste categories defined by the *Nuclear Energy Ordinance* (KEV) [14], and directly implemented into ISRAM and MIRAM [15]. These are:

- High level waste (HLW): Spent nuclear fuel, and vitrified high-level waste arising from the reprocessing of the spent nuclear fuel.

- Alpha-toxic waste (ATW): Waste with a specific activity of alpha emitters larger than 20'000 Bq/g.

- Low and intermediate level waste (L/ILW): All other radioactive waste. This includes the ILW from fuel reprocessing, packed into coquilles: hulls and ends (*CSD-C*) and vitrified sludges (*CSD-B*).

It bears pointing out that the ATW category defined in KEV do not comprise a separate category in the IAEA list, where it's included as part of ILW.

Another criterion used by ISRAM and MIRAM to group waste is based on the associated waste stream. Five generic waste streams are defined:

- Spent fuel assemblies (BE or also FA).

- Reprocessing waste (WA): concentrated fission products (and actinides) immobilized in a low-solubility glass matrix, as well as hulls and ends (CSD-C) and vitrified sludges (CSD-B).

- Operational waste (BA): Waste generated during normal NPP operation, such as resins from ion exchange filters, filters from cleaning systems, and contaminated protective clothing.

- Reactor waste (RA): Various components used inside the reactor vessel, such as control rods, various neutron flux detectors, and neutron sources.

- Decommissioning waste (SA): Waste arising during the NPP decommissioning, from dismantling of the plant—for example, the reactor pressure vessel (RPV), reactor internals (core plates, core barrel, etc.), bioshield concrete. The radiation is induced by both activation and contamination.

When employing the polluter pays principle and assessing the costs associated with the waste disposal and how they ought to be divided, it's important to keep track of the provenance of the waste.

- Nuclear power plants, with this category further divided into the four Swiss NPPs: KKB, KKM, KKG, KKL.
- ZWILAG, the interim waste storage facility.
- Medicine, industry, and research (MIR)—for example, PSI (Paul Scherrer Institute) or CERN (European Organization for Nuclear Research).
- Surface (encapsulation) facility (OFA).

The surface facility (located on top of the deep geological repositories) will produce operational and decommissioning waste, as it will contain facilities for the encapsulation of spent fuel and reprocessing waste, decontamination of dry storage casks.

MIRAM inventories provide the basis for long-term safety analyses, as well as input information required for deep geological repository planning. The included predictions of future inventories are based on defined scenarios. The basis scenario is defined assuming 60 years lifetime for all NPPs (except KKM, for which the already-known [16] lifetime of 47 years is taken) and maximum 30 years of decay storage. Other scenarios are defined to explore the range of potential waste volumes. The waste volumes and activities associated with the base scenario, given for the reference year 2075, can be seen in tables 1 and 2, respectively.

Table 1: Total volume of the conditioned (and in parentheses packaged for the final disposal) radioactive waste in Switzerland in m^3 for the reference year 2075 [15]

[m^3]	SF	WA	BA	RA	SA	MIR	OFA	Total
HLW	1′363 (8′125)	112 (381)				1 (9)		1′479 (8′515)
ATW		102 (634)			24 (24)	211 (783)		337 (1′441)
L/ILW			8′465 (31′302)	473 (1′807)	23′024 (31′459)	21′005 (25′775)	646 (2′293)	53′613 (92′636)
Total	1′363 (8′125)	217 (1′015)	8′465 (31′302)	473 (1′807)	23′048 (31′483)	21′217 (26′567)	646 (2′293)	55′429 (102′592)

Table 2: Total activity of the radioactive waste in Switzerland in Bq for reference year 2075 [15]

[Bq]	SF	WA	BA	RA	SA	MIR	OFA	Total
HLW	1.7e19	1.9e18				2.1e10		1.9e19
ATW		1.9e16			3.6e12	3.4e15		2.2e16
L/ILW			4.3e14	5.5e15	6.3e16	1.0e16	2.8e13	7.9e16
Total	1.7e19	1.9e18	4.3e14	5.5e15	6.3e16	1.3e16	2.8e13	1.9e19

The volumes are reported for conditioned waste, which includes the volume of the waste and the current (intermediate storage) container, and for waste packaged for the final disposal, which is based on the volume of the filled final disposal canisters. For example, if the operational waste is currently packaged in 200-liter drums, the conditioned volume is based on the volume of these drums. Later on, a number of these drums will be placed into a concrete container (in this example the LC-86 container) with mortar poured around the drums as the fill material. This is shown in figure 1. The corresponding (final disposal) volume is then based on the volume of the LC-86 container.

Figure 1: LC-86 container filled with 200-liter drums and mortar. (Image provided by Nagra.)

The total volume of radioactive waste is a quantity, which is not trivial to calculate. For many types of waste, it is certain that they will have to be treated as radioactive waste—for example, most of reactor internals. However, for a number of components there is a chance that they (or their parts) can be treated as conventional waste. For example, concrete structures surrounding the RPV are activated only to a small extent. The assessment whether a particular component is to be considered as radioactive waste or not is done by regarding the masses (or respectively surfaces) of the materials and evaluating their nuclide inventories against clearance levels. These are defined in the Radiological Protection Ordinance (StSV) [13].

Specifically, for each nuclide a specific activity clearance limit is defined. The fraction of the limit usage, defined as the specific activity divided by the corresponding clearance limit, is then summed over all the nuclides. That is,

$$\sum_{i=\text{nucl.}}^{\text{all nucl.}} \frac{a_i}{LL_i} < 1, \tag{1}$$

where a_i is the specific activity (in Bq/g) and LL_i is the clearance limit (also in Bq/g) for nuclide i. This is referred to as the *sum rule*.

If the sum is 1 or greater, the material is treated as radioactive waste (to be disposed) rather than conventional industrial waste. Exceptions exist for conditional release of materials exceeding the sum rule, governed by the guidelines defined by the Swiss Federal Nuclear Safety Inspectorate (ENSI) [17]. For example, article 115 of StSV defines an exception for radioactive waste to be recycled, allowing for the sum value of up to 10, as long as the recycling products do not exceed the clearance limits (sum lower than 1).

In order to calculate the exact value of the sum rule, detailed knowledge about the complete radionuclide vector is required. This is also the case for safety analysis, where different nuclides are important for its different aspects, such as long-term radiotoxicity, decay heat production, and gas production. As such, it's crucial to have a detailed knowledge about the complete radionuclide inventory in each waste stream.

In order to reduce the burden on the NPP operators, Nagra actively participates in characterization of waste streams, calculating the corresponding nuclide inventories, as well as volumes.

The next major version of MIRAM will be released in 2020—referred to as *MIRAM20*. This version will be used for calculations and analyses to be used for the repository general license application (RBG), which will be developed from 2022 until 2024, in accordance with the Sectoral Plan for Deep Geological Repositories (SGT) [18], as well as for the next cost study (KS2021).

1.3 SCOPE OF THIS THESIS

The existing individual methodologies for characterization of the different waste streams make various assumptions. Often they only focus on a small number of *key* nuclides (defined for example as nuclides most exceeding the clearance limits), or they introduce assumptions simplifying the characterization calculations. In the end, these decisions affect the quality and degree of detail of the resulting inventories, and therefore their applicability. However, as the deep geological repository project planning is progressing (and, for example, the surface (encapsulation) facility is being designed), more detailed information about the waste inventories is required. Additionally, the Swiss NPPs are now preparing for decommissioning (with KKM planned to shutdown in 2019 [16]), a process which will generate a significant amount of radioactive waste. New questions arise in connection with this planning, questions which cannot be satisfactorily answered using the existing methodologies. This represents a new goal for the Nagra waste characterization efforts—to characterize radioactive waste with high fidelity, allowing these inventories to support informed decision making during decommissioning planning and the decommissioning itself.

The work described in this thesis aimed to improve on the existing characterization methodology for selected waste streams entering MIRAM, such that the newly-developed methodology delivers a detailed and accurate (i.e., high fidelity) nuclide inventory, which would also significantly support the decommissioning and waste disposal planning.

The waste streams were selected based primarily on their contribution to the total activity (as shown in table 2), but also their connection with one another. These are: spent fuel, decommissioning waste, and reactor waste. Understanding of the fuel depletion is important because of its large contribution to the total waste activity, but also because it has a strong impact on the decommissioning waste, generated primarily by neutron activation (by neutrons leaking from the aforementioned fuel). Reactor waste, which generally arises through activation when in close proximity to the fuel, is characterized in a way similar to the decommissioning waste (as both result from neutron activation). Unlike decommissioning waste, the location of the components which form reactor waste was changing during operation, and the activation methodology must be extended to accommodate for this inherent difference. However, at its core, it retains its basis in the characterization methodology applies for the decommissioning waste, and a complete new methodology doesn't have to be developed from scratch. The thesis is structured to reflect this focus, with chapter 2 looking at the spent fuel, chapter 3 describing the new methodology for characterizing the decommissioning waste, and chapter 4 focusing on the extension of this methodology for reactor waste.

This thesis focuses on the development of methodologies rather than the analysis of the results obtained with these methodologies. The methodology was applied in work which is generally not public, using confidential data, thereby restricting the amount of concrete examples which could have been included in this thesis. Attempts were made to provide general descriptions of the applications, as well as to reference publicly available sources providing further details and context.

At the end, chapter 5 provides a future outlook and recommendations for the further developments of these methodologies.

2 SPENT FUEL

Spent nuclear fuel represents more than 95% of the activity at the time of the final NPP shutdown [19]. As such, detailed information about the fuel is essential for waste disposal planning—specifically, an accurate description of the nuclide inventory and the associated source terms (especially for nuclides deemed important by the safety analysis modeling), decay heat, and criticality. Short- and medium-lived nuclides are important for fuel handling and encapsulation (when they contribute to the associated dose rates), while long-lived nuclides are most relevant for the long-term safety assessment of the repository itself.

Over their life, the four Swiss NPPs will produce in total approximately 12,000 FAs (assuming MIRAM base scenario, as defined in section 1.2). Until 2006, Switzerland was sending spent fuel for reprocessing to La Hague, France and Sellafield, United Kingdom. In total, 771 tHM were reprocessed, producing 634 vitrified residue canisters (of HLW), all of which have now been sent back to Switzerland [20]. Additionally, ILW was produces and packed in *CSD-B* and *CSD-C* coquilles, containing vitrified sludges and compacted FA structural components, respectively. In the end, for repository planning, it is necessary to characterize also this vitrified waste, as well as all the FAs. However, this chapter will focus on the not-reprocessed spent fuel.

The methodology presently employed at Nagra to calculate fuel depletion is described in section 2.1. The ongoing developments of this methodology, and the motivations behind these developments, are discussed in section 2.2. Accurate knowledge of the behavior and evolution of the core are essential for NPP operators, making fuel depletion also essential for them. The codes used by the NPP operators in this context and the applications of their results are explained in section 2.3. These two methodologies (i.e., the one used at Nara and the one used by the utilities) are then benchmarked against each other for their ability to deliver detailed (and consistent with one another) nuclide vectors for spent fuel. That is, to assess whether (provided access to the necessary input data) both of the methodologies could be used to deliver a high fidelity nuclide vector for the spent fuel. The benchmark is defined and the results are presented in section 2.4. Finally, the possible future use of these methodologies to obtain the desired nuclide vectors, and the resulting implications, are discussed in section 2.5.

2.1 NAGRA FUEL CHARACTERIZATION METHODOLOGY

The utilities are required to declare the radiologically-relevant nuclide vectors of fuel assemblies sent to dry cask (intermediate) storage such as Zwilag. However, this requirement doesn't apply to the FAs in wet storage at the NPPs, since they could theoretically still be reused. Additionally, utilities are not asked to report the nuclide vector prognoses for the future fuel. Since for the purposes of waste disposal planning it's desirable to include these additional fuel assemblies, as well as provide information about additional nuclides (not tracked by the utilities, such as the long-lived nuclides), Nagra employs its own fuel characterization methodology to provide this fuel data, including the future forecast based on MIRAM-defined scenarios [20, 21].

The Nagra fuel characterization methodology [21, 22] is based on the SCALE 6.1 package developed by Oak Ridge National Lab (ORNL) [23], specifically on TRITON, a multi-purpose control module with discrete-ordinates-based lattice-physics capabilities. TRITON is used to create two-dimensional fuel assembly model *families* for each specific FA design and plutonium loading, each with a range of enrichments and moderator densities. These are all depleted (assuming ideal cycles) until a high burnup—higher than the highest expected fuel burnup—so that the resulting library covers the full range of expected fuel parameters. The produced output includes the *f33*-type files, which are mixture-wise flux-weighted 1-group cross sections. These are used by the ORIGEN-ARP module for the depletion and decay calculations. Any specific FA can then be characterized by interpolating the given parameter branches of this library, which the code accomplishes near-instantaneously. This way the user doesn't have to repeat the computationally-intensive self-shielding and neutron transport calculations for each FA. This approach is also used to perform the activation calculations for the fuel cladding [24].

2.1.1 TRITON Sequence

The TRITON control module automates calculation sequences of coupled SCALE modules to carry out multi-group cross section processing, neutron transport calculations, and isotopic depletion and decay [23, 25].

The depletion calculation sequence used by Nagra is summarized in figure 2. It utilizes BONAMI, CENTRM (Continuous Energy Transport Model), and PMC (Produce Multi-group Cross sections) modules for the processing of (resolved and unresolved) resonance cross sections, NEWT (New Transport Algorithm) for two-dimensional discrete ordinates neutron transport calculation, COUPLE for the updating of the cross section library, ORIGEN for material depletion and decay, and OPUS for output processing.

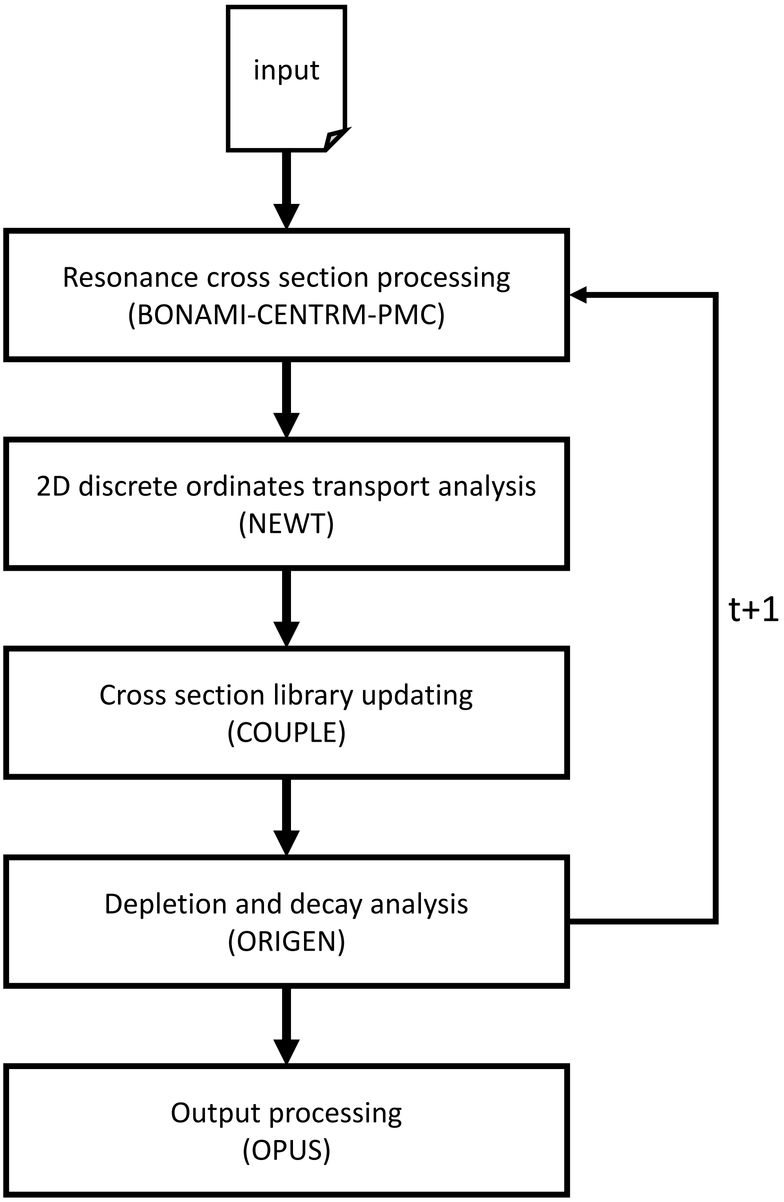

Figure 2: TRITON sequence

Resonance cross section processing

The TRITON sequences utilizes the BONAMI module to control the resonance cross section processing operations. Bondarenko resonance self-shielding calculations [26] are performed in the unresolved range. CENTRM and PMC modules are used in the resolved range.

The CENTRM module is designed to calculate continuous-energy zero- and one-dimensional neutron spectra on a very fine energy mesh. In this case, the self-shielded multi-group cross sections are generated by first performing a CENTRM calculation on an equivalent pin cell, and then using PMC to read the resulting continuous spectra and calculate the group-averaged cross sections. That is, the neutron spectra are used as weighting functions for the multi-group cross section averaging.

The resulting cross section libraries and mixing tables are then automatically read and used by the NEWT calculations, without the need for the user to define any mixing tables.

Neutron Transport

In order to calculate the weighted burnup-dependent cross sections and localized fluxes for the individual depletion regions, the NEWT module is used. This module is based on a two-dimensional, unstructured-mesh discrete ordinates solver, which can carry out multi-group neutron transport calculations for any general geometry (i.e., including atypical lattice designs and non-lattice fuel configurations).

The NEWT mesh is automatically defined using arbitrary polygons on top of the user-defined problem geometry. Polygons cannot exactly reproduce curved surfaces, such as cylindrical fuel and cladding surfaces. These are approximated using a (user-defined) number of lined segments. In order to calculate the neutron transport between the boundaries of these arbitrary polygons, the ESC (Extended Step Characteristic) [27] discretization is utilized, subdividing the mesh cells into trapezoids as a function of the angle discretization. Additionally, the problem domain is further sub-divided using an overlay grid in order to address the mesh size limitations resulting from the assumption (made in the ESC discretization) of a constant source within each computational cell. The computational cells are thus defined by both the (rectangular) overlay grid and the bodies (representing individual materials).

The transport calculations are performed in a two-dimensional representation, with reflective, white, or periodic boundary conditions. The resulting flux is therefore representative of an infinite system (in the axial direction). As such, before this flux can be passed on to the depletion calculation, it should be corrected for leakage. This is accomplished by calculating the buckling for the homogenized system, to find a value representative of a critical system.

Instead of NEWT, the user can use the KENO module in the sequence, performing the transport calculation using three-dimensional Monte Carlo methods. However, due to the high computational intensity, this is generally not done in the Nagra fuel analysis methodology.

Material Depletion and Decay

The nuclide transmutation calculations (depletion and decay) are carried out using the ORIGEN module. ORIGEN offers tools for comprehensive analysis of nuclide compositions, decay heat, and radiation (γ and neutron) source terms. ORIGEN included with SCALE 6.1 tracks 1119 fission products, 129 actinides, and 698 activation-relevant isotopes.

Once the transport calculation is complete, NEWT generates a three-group library based on the calculated fluxes for each mixture. COUPLE reads this library and collapses the multi-group cross sections using the provided (leakage-corrected) fluxes. It then uses these to update the ORIGEN cross section library.

Being a point-depletion code, ORIGEN depletes each mixture individually (instead of treating the FA as a whole). As such, it's necessary to use the fluxes across the FA to determine the point fluxes inside each depletion region.

COUPLE-ORIGEN calculations are repeated for each mixture being depleted, as specified by the user, using mixture-specific cross-section data and fluxes.

ORIGEN is designed to adjust flux levels to maintain the user-defined power level (unless it is operated in flux mode). However, since the relevant cross sections and spatial fluxes change as a function of burnup and operating conditions, the TRITON sequence employs an iterative approach to estimate fluxes and cross sections. The cross sections are updated using a transport calculation based on predicted concentrations at a mid-point of the given depletion period. These cross sections and the associated mid-point fluxes are used to perform depletion calculations, which are then extended to a mid-point of the next cycle. At this point the next half-point transport calculation is performed. These iterations are repeated until all depletion calculation cycles are completed.

As a default, a single cross section library at the mid-point of each cycle is used to approximate cross sections for the full cycle. In cases of significant isotopic changes during the cycle (e.g., at low burnup, particularly if there are poison rods present), the user can refine the cross section update interval by introducing additional steps within each cycle.

2.1.2 Model Assumptions and Optimization

The computational intensity of TRITON has been a challenge from the inception of the Nagra methodology [21]. The (two-dimensional) neutron transport calculation is performed using the discrete ordinates method [28] and is associated with significantly longer computational time than the Method of Characteristic [29] based codes (such as CASMO and Polaris introduced in the subsequent sections). For this reason, several modeling assumptions were introduced in order to reduce the computational time [20, 21]: symmetry, the *assign* function, and the *addnux* option.

Symmetry is a classic and frequently-used model simplification. Since many FAs are symmetric (typically 1/8 symmetry for PWR and 1/2 for BWR assemblies), it's possible to only model this fraction of the geometry and use the reflected boundary conditions for the axes of reflection. The impact of this simplification was explored in [21], where a PWR FA was modeled with 1/4 symmetry, leading to a deviation of 9 pcm. (1/4 symmetry was used instead of 1/8 symmetry, because the latter would require a definition of a triangular outer boundary, which is not trivial to implement in TRITON.) While this evaluation is not necessarily representative of all conditions, and the effect was only quantified on criticality (rather than the number densities of the individual nuclides), it still offers a useful insight into the overall magnitude of the effect on the results. In this case the computational time was reduced by a factor of 1.5.

The *assign* function allows the usage of the self-shielded microscopic cross sections calculated for a particular rod to be assigned to other rods. In order to minimize the resulting error, this is done for rods with the same initial enrichment and similar Dancoff factors [20]. The impact of this simplification was quantified (for a PWR FA) in [21], where it introduced a deviation of up to 600 pcm, but reduced computational times by a factor of 3 to 4.

The *addnux* option sets whether the code will track all the nuclides defined in the nuclear data library (*addnux=4*) or only a subset. When fewer nuclides are tracked, the computational time of cross section processing is reduced. However, as evaluated in [20], this introduces unacceptably large simplifications of the model, which significantly affect the calculated k_{eff} value. For this reason *addnux* is always set to 4 in the Nagra methodology. The exact impact on the computational time was not quantified.

2.1.3 Validation

In order for the model outputs to be useful, it's necessary to assess the *accuracy* of the model. This is done through *verification* and *validation*. As defined in [30], verification is “ensuring that the computer program of the computerized model and its implementation are correct”. That is, making sure that the model is in fact solving the defined problem correctly. This can be done by comparing the results with the analytical calculations or other codes (as long as they are solving the same type of problem), as well as by analyzing the results obtained with various mesh sizes and levels of convergence. Validation is defined [30] as “substantiation that a computerized model within its domain of applicability possesses a satisfactory range of accuracy consistent with the intended application of the model”. That is, making sure that the model is actually (sufficiently) descriptive of reality. This is done by comparing the evaluations produced by the model with experimental measurements. Just as models are developed for a specific purpose, so are verification and validation determined with respect to that purpose.

The aforementioned TRITON FA models were validated against numerous isotopic measurements in fuel samples, with results presented generally in internal Nagra reports, but also in published works. See [21] for validation against measurements performed in the scope of PSI LWR-PROTEUS Phase II campaign [31]. These samples were analyzed non-destructively at PSI-PROTEUS (using neutron measurements and gamma-ray emission and transmission tomography) [32] and destructively at the PSI Hotlab (using HPLC-MC-ICP-MS) [33]. The measured nuclide concentrations were compared to the calculated ones, showing an overall good agreement.

The successful validation has demonstrated that when provided with the detailed history parameters (such as axial power distributions, void profiles, and control rod movements over the life of each FA), this methodology delivers quality results. However, presently, such information about fuel assemblies is generally not available to Nagra. As such, the Nagra calculations are based on assumptions about the typical FA operating history.

2.2 ONGOING DEVELOPMENTS OF THE NAGRA FUEL CHARACTERIZATION METHODOLOGY

The computational requirements of TRITON, even after simplification introduced in section 2.1.2, have shaped the degree of detail targeted by the Nagra fuel characterization methodology. Therefore, following the release of SCALE 6.2 [34], exploratory work has begun to consider the replacement of TRITON with the new Polaris MOC-based lattice physics code [35], expected to be significantly faster.

Another new code released as part of SCALE 6.2 is ORIGAMI [34], which aims to replace ORIGEN-ARP. The biggest improvement between these codes is that ORIGAMI can perform multiple ORIGEN calculations at once in order to facilitate three-dimensional (i.e., node-wise axial and pin-wise radial) depletion and decay calculations. With ORIGAMI retailing all of the capabilities of ORIGEN-ARP and offering additional features, it was chosen as the preferred code for the Nagra fuel characterization methodology.

2.2.1 Polaris Methods

Recognizing that although TRITON offered superior modeling flexibility, it came at the expense of large computational intensity and long, error-prone input requirements, the US Nuclear Regulatory Commission (NRC) has tasked ORNL with the development of a new tool to replace TRITON. The result of this development is Polaris.

Polaris is based on a multi-group self-shielding method called the Embedded Self-Shielding Method (ESSM) [36] and the Insilico method of characteristics (MoC) solver [37]. It provides a simplified input, where tens of lines describe the whole model.

ESSM is used to calculate the self-shielded multi-group cross sections required by the transport calculation. Specifically, in order to solve the continuous energy slowing down equation, first the intermediate resonance (IR) approximation is used, and then the equivalence-theory-based expression for each spatial region of the problem is defined. This is then iteratively solved using a series of fixed-source MoC calculations to obtain the background cross sections.

These background cross sections are then used to calculate the total, scattering, ν-fission (representing the average number of neutrons produced per fission), and χ (representing fission yield) macroscopic cross sections for each material, as required for the transport calculation. The MoC solver is then used to iteratively calculate the k_{eff} and flux.

Afterwards, Polaris performs a critical buckling search by calculating the critical spectrum for the homogenized FA, accounting for the FA leakage effects.

Polaris retains the use of ORIGEN for depletion and decay calculations just like TRITON did. However, unlike TRITON, Polaris utilizes the API of ORIGEN to set the initial nuclide concentrations, set the solver method and decay time steps, retrieve the nuclide concentrations at the end of each time step, and set or retrieve nuclear data from the transition matrix.

The remainder of this section describes the aforementioned calculation procedure in more detail.

MoC General Theory

MoC represents an approach to solving the steady state neutron transport equation [38, 39]. In the neutron reference frame, the transport equation can be written as

$$\frac{d\Phi^g_{m,i}}{ds_m} + \Sigma^g_{tr,i}\Phi^g_{m,i} = Q^g_{m,i}, \tag{2}$$

where i and g are indices for mesh and energy group, respectively, Φ is the scalar flux, Q is an (angular) source in direction m, and s_m is the track length in the direction of neutron motion. This is the characteristic form of the neutron transport equation. Note that unlike the integro-differential form of the transport equation, this form features no partial derivative (in the streaming term of the equation). This is because in this frame of reference, this partial derivative can be reduced to a total derivative (along the neutron motion).

In order to solve this equation, it is integrated along s_m, assuming that the material properties (represented by Σ_{tr}) are constant in the whole mesh cell (m), and assuming that Q is spatially constant. The resulting equation expresses the flux at any point along the path in the mesh cell in terms of the flux at the entry border of the mesh cell, such that

$$\Phi^g_{m,i}(s_m) = \Phi^g_{m,i}(0)e^{-\Sigma^g_{tr,i}s_m} + \frac{Q^g_{m,i}}{\Sigma^g_{tr,i}}(1 - e^{-\Sigma^g_{tr,i}s_m}). \tag{3}$$

The full derivation of these equations can be found in [38].

In MoC flux calculations, neutrons are only allowed to move in a selected number of directions, this dividing the calculations into discrete directions. The directions not explicitly modeled are taken into account via a weight association with each direction. That is, the flux in a particular direction actually represents the neutron motion in a whole range of directions (about the given particular direction of motion).

The full set of (appropriately weighted) angles combines into a quadrature set, which is used to integrate the flux. That is,

$$\phi_i^g = \int_{4\pi} \Phi_i^g(\Omega)\, d\Omega = 4\pi \sum_m \Phi_{m,i}^g \omega_m, \tag{4}$$

where ω_m is the weight association with the direction m.

As such, the flux is calculated as the average flux value within the mesh cell i, for each discrete direction. As illustrated in figure 3, a set of parallel, equidistant (but not equally long) track paths is defined and traced over the problem geometry for each direction in the aforementioned quadrature set.

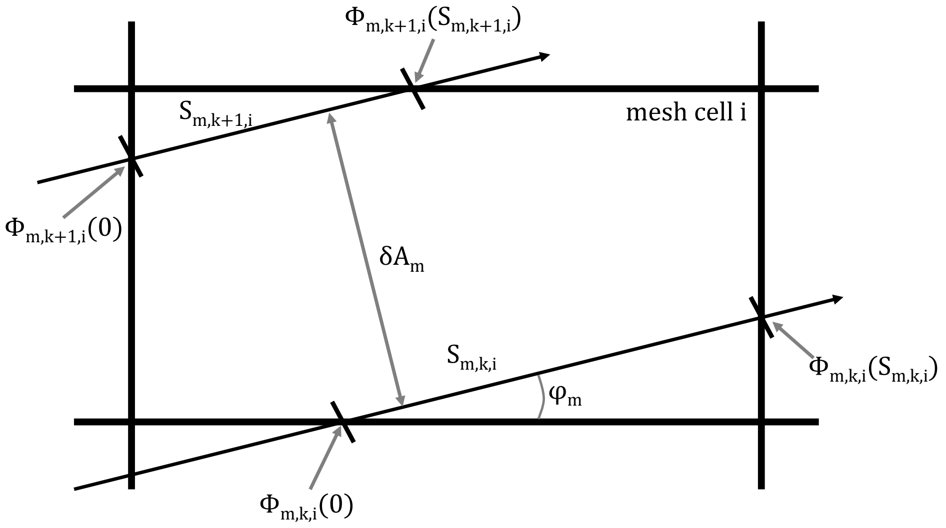

Figure 3: Characteristic tracks passing through a mesh cell

In reality, neutrons may also move in the space in between the individual tracks. This is taken into account by defining a width for each track, so that they represent a range of the cell's volume. (This is indicated as δA_m in figure 3.) As such, the accuracy of the MoC solution depends on this track width, as well as the aforementioned track weight, and mesh cell size (representing area of constant source).

MoC Solver

The aforementioned MoC theory is incorporated into a solver, capable of solving the transport equation problems. Polaris utilizes the Insilico package MoC solver, which is part of the Exnihilo code base [37]. As with the other modules, Polaris communicates with the MoC solver through an API, exchanging flux, cross sections, and source information.

The solver is used for both the ESSM (one-group) and the k_{eff} transport (multi-group) calculations. The employed iterative methods (GMRES or BiCGSTAB [34, 35]) are accelerated by the coarse mesh finite difference (CMFD) method.

The particle track lengths are calculated using the SCALE ray-tracing package, ATLAS [34]. Originally, ATLAS was used for ray-tracing KENO-VI geometries for the purpose of model visualization and verification. However, the same routines can be utilized for the MoC particle tracking. Since ATLAS is designed for the use with KENO-VI, in order to use it, Insilico first needs to use the problem geometry (provided by Polaris over the API) to generate a KENO-VI model. As of SCALE 6.2, this conversion can only be done for square light water reactor (LWR) lattices.

Self-shielded Cross Section Calculation with ESSM

Consider the continuous energy slowing-down equation for an energy group g. When the intermediate resonance (IR) approximation is applied and the equation is integrated over the bounds of the energy group g, the slowing-down equation for an energy group g can be written as

$$\boldsymbol{\Omega} \cdot \nabla\psi_g(\boldsymbol{r}, \boldsymbol{\Omega}) + \Sigma_{t,g}(\boldsymbol{r})\psi_g(\boldsymbol{r}, \boldsymbol{\Omega}) = \frac{1}{4\pi}\Sigma_{wr,g}(\boldsymbol{r})\phi_g(\boldsymbol{r}) + \frac{1}{4\pi}\Sigma_{nr,g}(\boldsymbol{r})\Delta u_g, \tag{5}$$

where r is the position vector, Ω is the angular direction, and g is the energy group index. Furthermore, ψ is the angular flux, ϕ is the scalar flux, Σ_{wr} and Σ_{nr} are the wide- and narrow-resonance material-wise cross sections, respectively, Σ_t is the self-shielded multi-group total cross section (defined as the continuous-energy total cross section collapsed with the continuous-energy scalar flux), and Δu_g is the lethargy width of group g.

Note that:

$$\Sigma_{t,g}(\boldsymbol{r}) = \Sigma_{a,g}(\boldsymbol{r}) + \Sigma_{wr,g}(\boldsymbol{r}) + \Sigma_{nr,g}(\boldsymbol{r}). \tag{6}$$

As the next step, the equivalence-theory expression is introduced for each spatial region in the problem domain. This allows the definition of the equivalence cross section, denoted Σ_{eq}:

$$\Sigma_{eq,g}(\boldsymbol{r}) = \frac{\Sigma_{a,g}(\boldsymbol{r})\phi_g(\boldsymbol{r})}{\Delta u_g - \phi_g(\boldsymbol{r})} - \Sigma_{nr,g}(\boldsymbol{r}), \tag{7}$$

where

$$\Sigma_{a,g}(\boldsymbol{r}) \equiv \sum_i N_i(\boldsymbol{r})\sigma_{a,g,i}(\boldsymbol{r}), \tag{8}$$

$$\sigma_{a,g,i}(\boldsymbol{r}) \equiv \sigma^{ref}_{a,g,i}\boldsymbol{F}_{a,g,i}(\sigma_{b,g,i}(\boldsymbol{r}), T(\boldsymbol{r})), \tag{9}$$

$$\sigma_{b,g,i}(\boldsymbol{r}) \equiv \frac{1}{N(\boldsymbol{r})}(\Sigma_{nr,g}(\boldsymbol{r}) + \Sigma_{eq,g}(\boldsymbol{r})) - \lambda_{g,i}\sigma_{p,i}, \tag{10}$$

where $\boldsymbol{F}$ denotes the Bondarenko interpolation, which is used to determine the nuclide-specific self-shielded multi-group absorption cross section, and is a function of the nuclide-specific background cross section (σ_b) and the spatial temperature distribution (T).

Note that equation 10 is dependent on the equivalence cross section. Due to this non-linear dependency, equation 5 must be solved iteratively.

The iterative procedure is set up as follows:

1. Initialize $\Sigma_{eq,g}$ to a guess value.
2. Calculate $\Sigma_{wr,g}$ and $\Sigma_{nr,g}$
3. Calculate $\Sigma_{a,g}$ using equations 8, 9, and 10. From this, compute $\Sigma_{t,g}$ (using equation 6).
4. Solve equation 5 for ϕ_g.
5. Calculate the new $\Sigma_{eq,g}$ from ϕ_g using equation 7 for each spatial region (or, alternatively, for each material region).
6. Is $\Sigma_{eq,g}$ converged? If not, go to step 3.

Note that this (1-group fixed source) calculation is performed for each energy group separately, and as such can be parallelized. It should also be noted that while Polaris applies this methodology to two-dimensional problems and uses MoC transport solver, this iterative procedure is applicable independent of the problem geometry (one-, two-, or even three-dimensional) and the underlying transport method (MoC, S_n).

A full description of ESSM with additional details can be found in its original publication [36].

Coupling between ESSM and Transport Calculation

ESSM calculation yields the equivalence cross sections, which can be used to calculate the material cross sections, required by the MoC solver for the transport calculation. For a mesh cell c with equivalence cross section $\Sigma_{eq,g,c}$, the background cross section for nuclide i is given by

$$\sigma_{b,g,i,c} = \frac{1}{N_{i,m}}(\Sigma_{eq,g,c} + \Sigma^{BI}_{g,c}) - \sigma^{BI}_{g,i,c}, \tag{11}$$

where i and m are nuclide and material indices, respectively. Here $\Sigma^{BI}_{g,c}$ represents the *homogeneous* component of the background cross section.

There are several ways that $\Sigma^{BI}_{g,c}$ can be computed in Polaris:

$$\Sigma^{BI}_{g,c} \equiv \sum_i N_{i,m}\sigma^{BI}_{g,i,c}, \tag{12}$$

$$\sigma^{BI}_{g,i,c} \equiv \begin{cases} \lambda_{g,i}\sigma_{p,i}, \\ \lambda_{g,i}\sigma_{p,i} + \sigma_{a,g,i,c}, \text{ or} \\ \lambda_{g,i}\sigma_{s,g,i,c} + \sigma_{a,g,i,c}. \end{cases} \tag{13}$$

Note that the second and third way of calculating $\sigma^{BI}_{g,i,c}$ shown in equation 13 depends on the self-shielded cross sections ($\sigma_{a,g,i,c}$ and $\sigma_{s,g,i,c}$). In these cases, Bondarenko iteration must be used.

The self-shielded microscopic cross sections can be determined from $\sigma_{b,g,i,c}$ using the Bondarenko interpolation:

$$\sigma_{x,g,i,c} \equiv \sigma^{ref}_{x,g,i}\boldsymbol{F}_{x,g,i}(\sigma_{b,g,i,c}, T_m), \tag{14}$$

where the index x denotes any particular reaction, T is temperature, and $\boldsymbol{F}$ is the Bondarenko interpolation function (which appeared previously in equation 9).

Flux-volume weighting is then used to determine the self-shielded cross sections from $\sigma_{x,g,i,c}$:

$$\sigma_{x,g,i,m} = \frac{\sum_{c\in m}\sigma_{x,g,i,c}\phi_{g,c}V_c}{\phi_{g,m}V_m}, \tag{15}$$

where $\phi_{g,c}$ and V_c are the cell flux and volume, respectively, such that:

$$V_m \equiv \sum_{c\in m} V_c, \tag{16}$$

$$\phi_{g,m} \equiv \frac{1}{V_m}\sum_{c\in m}\phi_{g,c}V_c. \tag{17}$$

The fission production terms $\nu\Sigma_{f,g,m}$ and $\chi_{g,m}$ can then be expressed as

$$\nu\Sigma_{f,g,m} = \sum_i N_{i,m}\nu_{g,i}\sigma_{f,g,i,m}, \tag{18}$$

$$\chi_{g,m} = \frac{\sum_i N_{i,m}\sum_{g'}\chi_i^{g'\to g}\nu_{g',i}\sigma_{f,g',i,m}\phi_{g',m}}{\sum_g \nu\Sigma_{f,g,m}\phi_{g,m}}. \tag{19}$$

The macroscopic cross section $\Sigma_{t,g,m}$ is expressed as

$$\Sigma_{t,g,m} = \Sigma_{t_0,g,m} + \sum_i N_{i,m}\sum_x \sigma_{x,g,i,m}, \tag{20}$$

where $\Sigma_{t_0,g,m}$ represents reaction cross sections which are *not* self-shielded:

$$\Sigma_{t_0,g,m} \equiv \sum_i N_{i,m}\sigma_{t_0,g,i}, \tag{21}$$

$$\sigma_{t_0,g,i} \equiv \sigma_{(n,2n),i,g} + \sigma_{(n,n'),i,g} + \sigma_{(n,\alpha),i,g} + \cdots \tag{22}$$

Then the macroscopic cross section $\Sigma_{l,m}^{g'\to g}$ can be expressed as

$$\Sigma_{l,m}^{g'\to g} = \Sigma_{0,l,m}^{g'\to g} + \sum_{i} N_{i,m}\sigma_{s,g',i,m}\boldsymbol{G}_{s,l,i}^{g'\to g}(T_m), \tag{23}$$

where l is the scattering order, $\boldsymbol{G}_{s,l,i}^{g'\to g}$ is the temperature interpolation function, and $\Sigma_{0,l,m}^{g'\to g}$ represents the sum of all not self-shielded temperature-independent cross sections, such that

$$\Sigma_{0,l,m}^{g'\to g} \equiv \sum_{i} N_{i,m}\sigma_{0,l,i}^{g'\to g}, \tag{24}$$

$$\sigma_{0,l,i}^{g'\to g} \equiv 2\sigma_{(n,2n),l,i}^{g'\to g} + 3\sigma_{(n,3n),l,i}^{g'\to g} + \sigma_{(n,n'),l,i}^{g'\to g} + \cdots \tag{25}$$

Note that $\sigma_{t_0,g,i}$ in equation 22, and $\sigma_{0,l,i}^{g'\to g}$ in equation 25 are independent of material (m). As such, they each are only calculated once for each nuclide.

All these equations are then incorporated into an iteration procedure to calculate k_{eff}, set up as follows:

1. Initialize $\phi_{g,c}$ to a guess value.
2. Use equations 21, 22, 24, and 25 to calculate $\sigma_{t_0,g,m}$ and $\sigma_{0,l,m}^{g'\to g}$.
3. For each material m:
    a) Bondarenko iteration: use equations 11, 12, and 13 to calculate the background cross section $(\sigma_{b,g,i,c})$ for each c $(\in m)$.
    b) Bondarenko interpolation: use equation 14 to calculate the self-shielded microscopic cross sections $(\sigma_{x,g,i,c})$ for each c $(\in m)$.
    c) Use equation 15 (flux-volume weighting) to calculate $\sigma_{x,g,i,m}$.
4. For fissionable materials only: use equations 18 and 19 (microscopic cross section mixing) to calculate the $\nu\Sigma_{f,g,m}$ and $\chi_{g,m}$.
5. Use equation 20 to add the unshielded component to the self-shielded cross section, thus calculating the total cross section.
6. Use equation 23 to add the unshielded component to the self-shielded scattering cross section, thus calculating the scattering cross section.
7. Calculate k_{eff} and $\phi_{g,c}$.
8. Are k_{eff} and $\phi_{g,c}$ both converged? If not, go to step 3.

2.2.2 Speed comparison between TRITON and Polaris

The version of TRITON shipped with SCALE 6.2 was significantly optimized compared to the SCALE 6.1 version, offering speed-ups in the order of factor 2 [34]. However, the Polaris code was expected to be faster yet. These significant increases in speed allow a departure from accuracy-affecting simplifications, such as the *assign* function.

In order to provide a qualitative speed comparison between SCALE 6.1 TRITON, SCALE 6.2 TRITON, a burnup calculation of an 8x8 BWR FA was performed. Specifically, the Fukushima Daini 2 DN23 FA from SFCOMPO, a database of measured spent fuel isotopic concentrations [40, 41], with a decay time of 120 years was calculated. No nuclides were excluded, thereby using all the nuclides available in the SCALE library were considered.

Polaris by default tracks the material vector of every fuel rod independently. Therefore, even though the input defined only six materials (i.e., six different enrichments), the calculation tracked 62 different material vectors ($8 \times 8 - 2$ water rods). Ray spacing was set to 0.05 cm, the nuclear data library used was *252g SCALE*. In total 36 depletion steps were defined: $30 +$ time $0 + 5$ decay steps.

TRITON was also set up with 6 different enrichments, but because of lattice symmetry, only 19 materials were used for depletion and cross section processing. S_N order of 8 was used. In total 41 depletion steps were defined: $30 +$ time $0 + 5$ low-power steps $+ 5$ decay steps. Low-power steps were used because TRITON cannot process zero power steps. The SCALE 6.1 calculation used the *238g SCALE* while the SCALE 6.2 calculation used the *252g SCALE* library.

The computational times taken to run the model with each code are summarized in table 3.

Table 3: Speed comparison between TRITON (SCALE 6.2.3 and 6.1.3) and Polaris (SCALE 6.2.3) for a Fukushima Daini 2 DN23 FA

Code	Time [hours]
TRITON (S6.1.3)	40.94
TRITON (S6.2.3)	17.02
Polaris (S6.2.3)	7.63

It can be seen from these results that the speed up of TRITON in SCALE 6.2 is indeed significant (and in this case even greater than the approximate factor two described in [34]). Polaris is then a further factor two faster than SCALE 6.2 TRITON. This is despite the fact that the TRITON calculation processed less than a third of the materials of the Polaris calculation. Theoretically, in order to compare the speeds completely fairly, the TRITON calculation would have to be modified to process all 62 materials individually. However, this would not be representative of the way TRITON is used in any application.

2.2.3 Outstanding challenges

Since Polaris is a new code, there are not many published validation studies for it. However, efforts to validate Polaris in-house against numerous

SFCOMPO sample sets is currently ongoing.

As of SCALE 6.2.3, Polaris still cannot create the microscopic cross section library for ORIGAMI (or ORIGEN-ARP). This feature is expected to be shipped with SCALE 6.3 [35].

2.3 SWISS NUCLEAR POWER PLANTS: STUDSVIK CMS

For many applications, the Swiss NPPs rely on the well-established coupled transport-diffusion code sequence developed by Studsvik. The lattice physics code CASMO [39] is used to solve the neutron transport equation (as a function of space, angle, energy, and time) for 2D slices (*lattices*) of each individual FA design. These calculations solve for the neutron spectrum and the multi-group self-shielded cross sections within the FA as a function of burnup, time, and operating conditions. The results are then post-processed by another Studsvik code, (*CMSLINK*), which formats them into a binary library of cell data (such as homogenized cross sections, diffusion coefficients, and assembly discontinuity factors) [42]. This library is then used by a diffusion-based nodal core code, such as SIMULATE [43]. This code sequence is sometimes (e.g., in KKB [44, 45]) extended by an on-line core monitoring and reactivity management application GARDEL [46, 47], which provides an automated core tracking system (with an archival database) which updates the core model throughout the cycle based on changes in operating conditions reported by the various sensors. The overall code sequence is referred to as Studsvik Core Management System (CMS) [48, 49].

These calculations are performed to demonstrate the compliance with the safety, operational, and design criteria in the context of fuel reload analysis, fuel safety [50], and periodic safety reviews [51].

The strength of the CMS code sequence is the integration between the codes, which allows one to perform core-follow calculations on the core level. In order to get familiarized with, and to test the capabilities of the sequence, the PWR-based *BEAVRS* benchmark [52] was solved using CMS [53] for the purposes of this thesis. The results obtained were on par with high-fidelity multi-physics core simulation code *nTRACER*, which performs sub-pin level transport calculation and on-the-fly resonance self-shielding treatment [54].

As these codes focus on reactivity calculations and nuclear reactor operation, they primarily track nuclides relevant to these activities. As of CASMO5 2.03 (first released 2012), the library chains include 250 nuclides [55]. In order to address the back-end of the fuel cycle calculations, Studsvik offers to extend the CMS sequence with an additional code called SNF.

SNF is a spent nuclear fuel analysis code, which can calculate isotopic concentrations, photon and neutron source terms, and decay heat of spent fuel [56]. The SNF isotopic concentrations are based on final burnup, spectrum history, and power density history of each axial node of a given fuel assembly, as well as nodal operating history (from SIMULATE). The nuclide concentrations at discharge are used as initial conditions for solving the full decay chains. The corresponding buildup and decay chains are integrated over the entire core lifetime to obtain EOL nuclide concentrations [57]. SNF has been previously validated against ORIGEN-S and numerous decay heat measurement campaigns [57–60].

As of version 1.07, SNF can calculate the concentrations for 889 nuclides [61]. When compared with the list of nuclides identified as potentially relevant for long-term repository safety assessment by different agencies, the SNF contains all nuclides from some lists [62], but misses some nuclides from others [63]. Specifically, the following thirteen (potentially) safety-relevant nuclides are currently missing in SNF: ^{10}Be, ^{32}Si, ^{40}K, ^{41}Ca, ^{171}Tm, ^{182}Hf, ^{192}Ir, ^{193}Pt, ^{194}Os, ^{204}Tl, ^{205}Pb, and ^{208}Bi. However, with the list growing with each code version, should these nuclides indeed be required for the safety assessment, it is likely that they will eventually be implemented. As such, SNF, backed by the corresponding files from the CMS sequence, represents a suitable method to obtain the nuclide information needed for waste disposal.

2.4 BENCHMARK OF SNF AGAINST POLARIS

With SCALE and Studsvik CMS both being concurrently used fuel characterization code families, it is desirable to compare them against each other and assess the degree of agreement and identify the sources of any differences. For this purpose a benchmark between SCALE's Polaris and the full Studsvik CMS sequence (CASMO - SIMULATE - SNF) was defined and carried out between Nagra and Studsvik.

2.4.1 Scope

The benchmark was supported by KKM, which agreed to provide the necessary information on five FAs, representing four different FA designs: GE8, GE11, GE14, and GNF2.

In order to compare the two code sequences, common operational parameters had to be used. For this purpose, the necessary information was extracted from SIMULATE for each of the five FAs. Specifically, for each irradiation step (300-500 steps for each FA), the following parameters were reported: duration (of the given irradiation step) in days, nodal power, nodal moderator density, nodal fuel temperature, presence of control rod (Boolean: yes or no). Material definitions were also based on the definitions provided by Studsvik, with impurities being neglected.

This information was used to construct Polaris models, which mirror the CMS operational parameters. This way the differences will arise from the codes themselves and the associated nuclear data libraries rather than any differences in the operating history parameters.

The nuclide vectors (in mass per FA node) were defined as the main point of comparison. Decay heat, photon source term and neutron source term were also identified as quantities of interest, albeit acknowledging that these quantities are directly linked to the nuclide vector. The comparison was agreed to be made at several different points in time. Specifically, at 0 years, 10 years, 50 years, 100 years, 1000 years, and 10000 years from a reference date, defined by Studsvik as 2019-08-01.

2.4.2 Code sequences

The CMS calculation was based on CAS-5 version 2.11.00, SIM-3 version v6.09.29 (KKM-2), and SNF version v1.07.00, with the nuclear data taken from the E7R1LIB library (version E7R1.202-130121).

Polaris calculations were based on code versions and (ENDF/B-VII.1 based) nuclear libraries included in the SCALE 6.2.3 release. Specifically, the 56 energy group library was used.

2.4.3 Results

The full comparison will be published in a separate scientific publication. However, a selection of results is included in this section.

Specifically, the calculated mass for 40 selected nuclides is compared. Table 4 shows the mass calculated by Polaris (in g/tHM), as well as the relative percent difference (RPD) between Polaris and SNF calculated masses, defined as (Polaris-SNF)/SNF. All results are shown for 0 and 50 years from the reference date.

Overall the results are satisfactory. The Nd-148 agreement confirms that the exact burnup was matched well. The energy spectrum can be inferred from the differences in actinides. In this case, while the calculated masses of U-235 and Pu-239 show good agreements, Pb-210, Po-210, Th-229, and especially Th-232—that is, the decay products of the transmuted actinides—show large deviations (up to 147.7% for Th-232). The differences for latter nuclides are caused by higher order spectral effects. It's also worth noting that since in real calculations impurities will be considered, the Th impurity in the fuel will dominate the Th production captured in this benchmark. Therefore, while it provides an insight into this code comparison, the exact result for Th-232 is of low concern.

Looking at the fission products, Nb-94, Mo-93, Sn-121m, and Sn-126 also show significant differences. (Please note that while the RPD for Mo-93 is

Table 4: Polaris-SNF comparison for GE8 FA. Polaris results (in g/tHM) and relative percentage difference (RPD), defined as (Polaris-SNF)/SNF, between Polaris and SNF for the reference date and reference date + 50 years.

Nuclide	2019		2069	
	Polaris (g/tHM)	RPD (%)	Polaris (g/tHM)	RPD (%)
Sr-90	3.8e+02	+1.8	1.1e+02	+1.8
Zr-93	8.8e+02	+0.5	8.8e+02	+0.5
Nb-94	4.0e–03	+168	4.0e–03	+168
Mo-93	1.7e–04	+35′149	1.7e–04	+35′152
Tc-99	9.8e+02	+0.7	9.8e+02	+0.7
Ru-101	9.8e+02	+0.9	9.8e+02	+0.9
Rh-103	5.7e+02	+1.3	5.7e+02	+1.3
Pd-107	3.0e+02	+1.7	3.0e+02	+1.7
Sn-121m	3.4e–01	+61	1.6e–01	+61
Sn-126	2.7e+01	+13	2.7e+01	+13
I-129	2.0e+02	+7.4	2.0e+02	+7.4
Cs-135	5.0e+02	+2.0	5.0e+02	+2.0
Cs-137	9.2e+02	–1.3	2.9e+02	–1.3
Nd-148	4.7e+02	+0.8	4.7e+02	+0.8
Sm-151	8.6e+00	–2.1	5.9e+00	–2.1
Eu-151	1.6e+00	–4.8	4.3e+00	–3.1
Eu-153	1.4e+02	–1.0	1.4e+02	–1.0
Gd-155	1.2e+01	–6.9	1.2e+01	–6.0
Pb-210	5.0e–09	+19	8.3e–08	–3.6
Po-210	8.6e–11	+27	1.4e–09	–1.6
Ra-226	1.4e–06	–6.8	1.4e–05	–3.3
Ac-227	2.5e–07	+1.4	5.5e–07	–0.3
Th-229	2.5e–06	+21	4.6e–06	+8.8
Th-230	1.2e–02	–5.0	4.5e–02	–2.0
Th-232	8.0e–03	+148	1.5e–02	+51
Pa-231	7.9e–04	+1.4	1.1e–03	–0.8
Pa-234	2.5e–10	+0.0	2.5e–10	+0.0
U-234	2.0e+02	–2.4	2.7e+02	+0.2
U-235	6.0e+03	–0.3	6.0e+03	–0.3
U-236	4.6e+03	+2.7	4.6e+03	+2.7
Np-237	4.8e+02	+3.8	5.6e+02	+3.5
Pu-238	2.1e+02	+9.2	1.4e+02	+9.2
Pu-239	4.5e+03	–0.6	4.5e+03	–0.6
Pu-240	2.6e+03	–1.1	2.6e+03	–1.0
Pu-241	4.2e+02	+4.9	3.7e+01	+4.9
Pu-242	8.3e+02	+4.9	8.3e+02	+4.9
Am-241	8.0e+02	+0.9	1.1e+03	+2.1
Am-243	1.6e+02	–0.7	1.6e+02	–0.7
Cm-244	3.3e+01	+2.5	4.9e+00	+2.5
Cm-245	3.9e+00	+2.3	3.9e+00	+2.3

extremely large, its absolute mass is very low.) Given that the fission yield fraction for these nuclides varies significantly between U-235 and Pu-239 (for example, the fission yield fraction for Nb-94 is 1.5*e*–9 for U-235 but 9.6*e*–8 for Pu-239 [64]), the aforementioned spectrum effect also plays a significant role here, as do any differences in the underlying nuclear data (fission yields in particular).

The comparison between 2019 and 2069 results is also worthy of attention, as it exhibits some interesting phenomena. For most nuclides, the percentage agreement doesn't change between the two time points. This is because the half-lives of these nuclides are well known, and there is no difference in the decay calculated by either one of the codes. However, not all nuclides simply decay. Some are in fact produced from the decay of other nuclides. For example, Eu-151 increases from –4.8% to –3.1%, U-234 increased from –2.4% to +0.2%, Am-241 increases from +0.9% to +2.1%, and Np-237 decreases from +3.8% to +3.5%. Eu-151 is produced through beta decay of Sm-151, for which the RPD is only –2.1%. As such, the RPD of Eu-151 approaches towards that of Sm-151. Similarly, U-234 is produced by alpha decay of Pu-238, which has RPD of +9.2%. Am-241 and Np-237 are both affected by the decay chain of Pu-241, which decays into Am-241 (though alpha decay), which then decays into Np-237. In all these cases the RPD of the daughter again approaches the RPD of the mother.

2.5 APPROACHES TO HIGH-FIDELITY FUEL CHARACTERIZATION FOR WASTE DISPOSAL

In the past, given the lack of detailed cycle information available to Nagra and the limited speed of TRITON, the fuel characterization contained a lot of conservatism. This proved sufficient for long-term safety assessments, which were then the primary aim of the fuel characterization calculations. However, nowadays it is envisioned that the calculated inventory will also be used for the safety assessment of the OFA and short-term repository safety. Therefore, in order to avoid excess conservativeness which would lead to additional shielding design, waiting time between OFA operations, and excessive fuel storage time, all of which impact the cost, it is highly desirable to transition towards a *best estimate plus uncertainty* methodology.

As was shown in this chapter, both SCALE (as utilized by the Nagra fuel characterization methodology) and Studsvik CMS code sequences can deliver the necessary results at the needed level of fidelity (*best-estimate*). However, since Nagra doesn't have the information needed to carry out the calculations for the existing spent fuel (nodal power and void distribution, detailed operating power history), either of these two approaches can be taken to obtain the desired results:

- the nuclear power plants will use their existing CASMO models and SIMULATE restart files and use SNF to generate the required nuclide vectors for each FA, or

- the data necessary to carry out the calculations will be extracted from the existing CMS models and provided to Nagra, with the final nuclide vectors calculated using SCALE.

For both options, the data may be requested within the context of the disposability certificate (ELFB) application, whose procedure and requirements remain to be defined.

The quantification of uncertainty associated with these calculations is the subject of another EPFL PhD thesis with a (preliminary) title "Uncertainty Quantification for the Swiss Model Inventory." The best estimate burnup credit calculations (and also the associated uncertainty quantification), carried out for the purposes of optimizing final storage cask loadings, are the subject of another project, carried out by PSI [65].

3 DECOMMISSIONING WASTE

The radiological characterization of the NPPs forms an integral part for the estimation of the decommissioning costs. In this context, a detailed understanding of the activity distribution within the NPP at time of shutdown is essential for the planning of the decommissioning process and the corresponding segmentation strategy, choice of waste containers, packaging concepts and logistics considerations.

The most important pathways towards the creation of radioactive waste are neutron activation and contamination. With almost 10^{17} neutrons released per second per MW (of thermal power), despite the many layers of shielding, a fraction of them successfully leaks out of the core, and eventually the RPV. These neutrons then interact with the nuclei in the surrounding materials (including their impurities). Most of the products created in these neutron reactions are radioactive. This process is referred to as neutron activation. Contamination results from direct contact with radioactive substances, generally within the primary loop, for example core support plate or steam separators pipes coming in contact with fission products released into the coolant by leaking fuel rods [66]. At time of shutdown, a 1000 MW_e PWR would be expected to have a neutron-activated inventory in the order of 10^{17} Bq and contamination inventory in the order of 10^{15} Bq [67].

Once the concentration of radionuclides increases beyond a regulatory limit [13] the material has to be treated as radioactive waste. The prediction of the extent of the material activation and contamination is therefore directly related to the calculation of the volume of the radioactive waste. Furthermore, the extent of the activation determines the shielding requirements for the waste containers to be used, making activation analysis also essential for the packaging concept development.

In this context, Nagra regularly updates its studies for the radiological characterization of all Swiss NPPs. Such efforts include the estimation of radioactivity in the NPP through neutron activation and radioactive contamination of structures and components within the controlled area of the reactor facility.

For this purpose, Nagra has over the past ten years developed an NPP activation analysis methodology, which has been successfully applied to all Swiss NPPs [68]. This thesis aims to provide an overview of the evolution of the Nagra methodology and the latest developments spanning the methods used and the insights gained through application.

Contamination is generally determined through direct measurements [69] and is considered beyond the scope of this thesis.

3.1 PREVIOUS APPROACHES

Material activation was always understood to be important. However, the ability to model the phenomenon accurately required gradual understanding of the nature of neutron transport in complex geometries, as well as improvements in the commercially available computational power. As such, the approach to activation analysis has gone from simple calculations to increasingly complex (and with it, increasingly computationally intensive) simulations.

3.1.1 Interpolated Isolines Approach

The early approaches to activation analysis at Nagra were simple. As shown in figure 4, a one-dimensional (three energy group) flux attenuation calculation was performed in two axial directions (up and down) and the radial direction, with the result represented in the form of isolines.

The isolines calculated for the three directions were then interpolated in-between, forming a three-dimensional flux field for each one of the three neutron energy groups. This information was then input into the activation code *GRSAKTIV* [70], which carried out the activation calculations.

This approach involved many simplification and assumptions. One had to assume the shape of the isoline in between the calculated directions. This was done by linear interpolation of the relative distance between the individual isolines between the values calculated for the axial and the radial direction. Most importantly, this approach completely neglected the phenomenon of neutron streaming—that is, the transport of neutrons through different (even very small) gaps in shielding—allowing them to travel *around* various shielding barriers. The uncertainties and known limitations of the approach were compensated by a great degree of conservatism.

3.1.2 Rotationally-symmetric Monte Carlo Approach

Following a feasibility study in 2010 [71], which showed that it was computationally affordable to use rotationally-symmetric three-dimensional Monte Carlo models of neutrons transport, a methodology based on a Monte Carlo particle transport code *MCNP* [72] was developed [68]. This methodology is summarized in figure 5.

Initially, technical documentation for the NPP in question is obtained from the utility, detailing the geometry and material composition of all the components, together with the reactor core parameters, such as the fuel assembly type, distribution of power and void in the core, and the plant

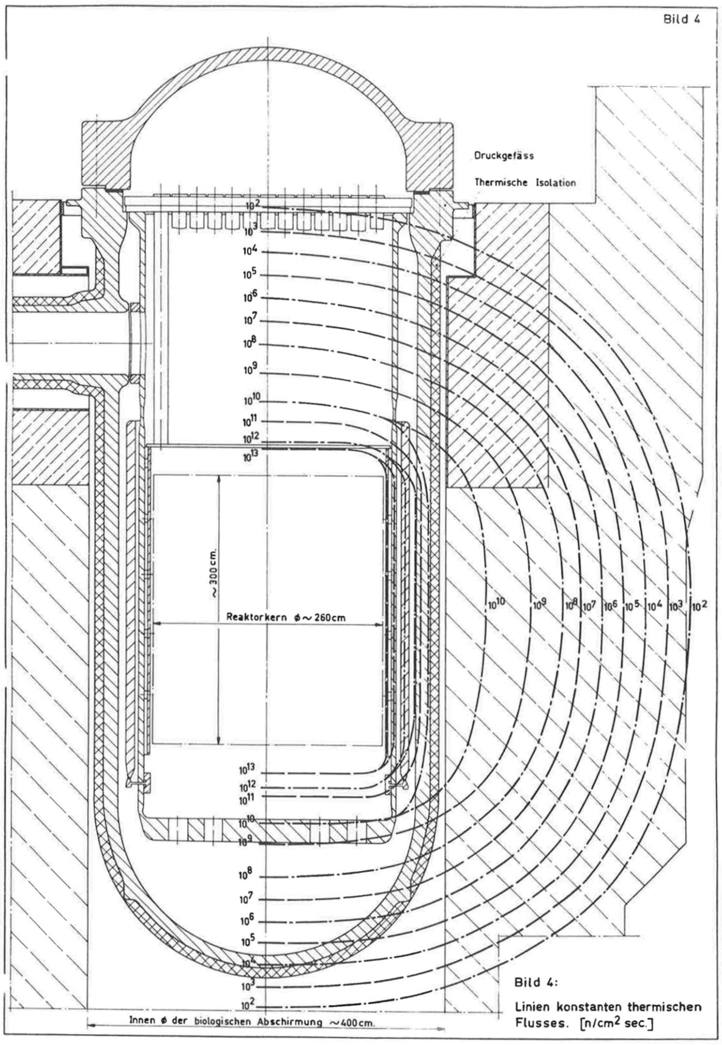

Figure 4: Activation analysis using interpolated isolines

operation history throughout its whole lifetime.

This information is then used to create an MCNP model of the whole plant. The extent of the model is based on an approximation of the extent of the activation. That is, zones where activation is very unlikely to reach the release limits are not modeled. The model is then used to determine neutron flux and spectrum in areas of interest, which is in turn used to carry out the activation calculations.

In order to limit computational intensity, the models of all NPPs were made rotationally symmetric. Furthermore, the shapes of all components, including the core and core internals, were approximated using basic geometrical shapes (mostly cylinders). Modeling of the rooms surrounding the RPV is a very challenging tasks. It is possible to implement static components—this is in fact done when they are large and important for shielding. However, much of the content of these rooms changes with time, with generally no record of the room contents existing. As such, it's impossible to accurately capture the exact shielding in these areas.

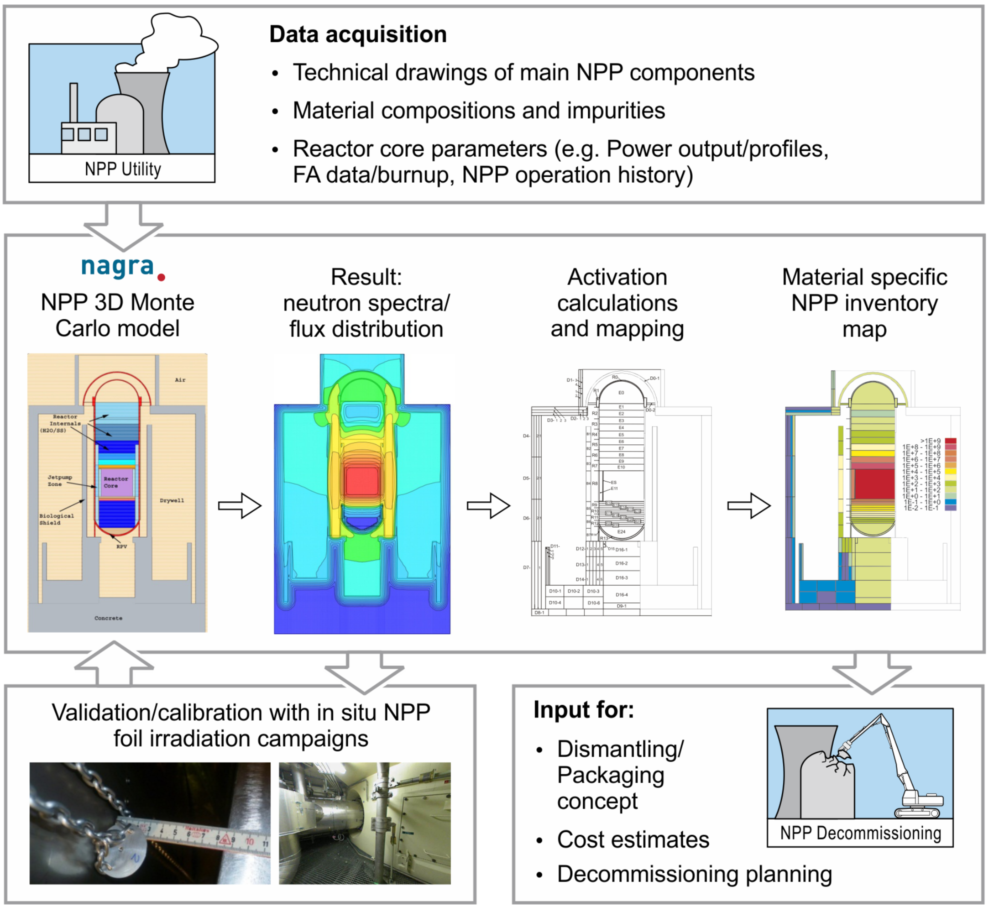

Figure 5: Nagra 2011 Activation Analysis Methodology

Investigations into the homogenization of the shielding materials into the room (air cell) showed an overestimation of the shielding and therefore underestimation of the flux (making it a non-conservative assumption). This is because spearing of the material blocks all the possible streaming paths, which would normally contribute significantly to the neutron flux. Furthermore, the exact mixing ratio of air and various metal representing the room contents is difficult to estimate (especially given the lack of information about the room content over the plant life), thereby adding to the uncertainty of the homogenization approach. A decision was therefore made to model the rooms as empty, underestimating the neutron shielding, and thus (conservatively) overestimating the neutron flux in these areas. This assumption is sometimes referred to as the *empty room assumption*. Note that this systematic underestimation of the neutron shielding causes the flux overestimation to grow with distance (from the core—i.e., through the empty rooms), as the neglected amount of shielding accumulates.

The MCNP source particle emission distribution was also adjusted to speed up the calculations. As an example, consider the core of KKM, originally formulated in [71]. As illustrated in figure 6, the active core was modeled as a cylinder (with radius defined to conserve the total volume of the active zone).

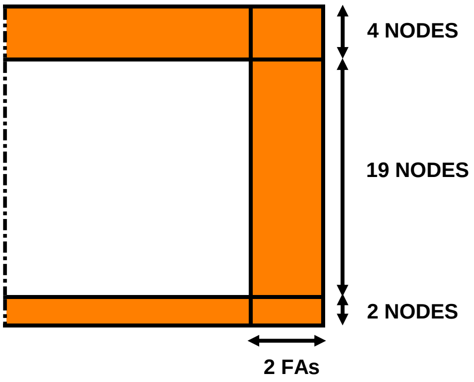

Figure 6: KKM core design (2011 model)

Since the majority of the neutrons leaking radially from the core come from the outermost row of FAs, the core cell was split radially into two regions, such that the two outer FAs are in the outer region and the remainder of FAs are in the inner region. Furthermore, to account for the axial leakage, the same procedure was followed, splitting the core cell axially into the upper region (4 topmost nodes), lower region (2 bottommost nodes), and middle region (with the remaining 19 nodes). As a result, the core cell was split into six cells. The central cell (representing the inner region radially and the middle region axially) was then set as inactive. (Figure 6 shows active cells in orange.) That is, no source particles are created in this cell (with the emission rate adjusted accordingly). This way particles most unlikely to contribute to the leakage from the core did not have to to be tracked, reducing computational time. Note that more nodes are considered at the top, because for a BWR such as KKM, the higher void fraction in the upper region results in lower shielding.

In order to capture the power distribution within the KKM core, the source particle emission probability was adjusted for each cell, capturing the power in each given region. Furthermore, the axial power profiles in the top and bottom cells were manually defined to match the (nodal average) axial power distribution provided by KKM. The middle region cell was assumed to have a homogeneous power distribution [71].

Despite these numerous approximations, the models successfully captured much of the neutron streaming behavior—see the KKM flux distribution map shown in figure 7.

The transport calculations were accelerated by employing various variance reduction methods. These are described in section 3.3, together with the new developments in this area.

For the purpose of activation calculation the model is split into a number of (rotationally-symmetric) cells, each assigned a reference name. The KKM zoning can be seen in figure 8. In each cell, 84-energy-group neutron flux is captured using a type-4 tally [72]. This energy group structure was a requirement of the activation code used—*GRSAKTIV-II* [74], an updated

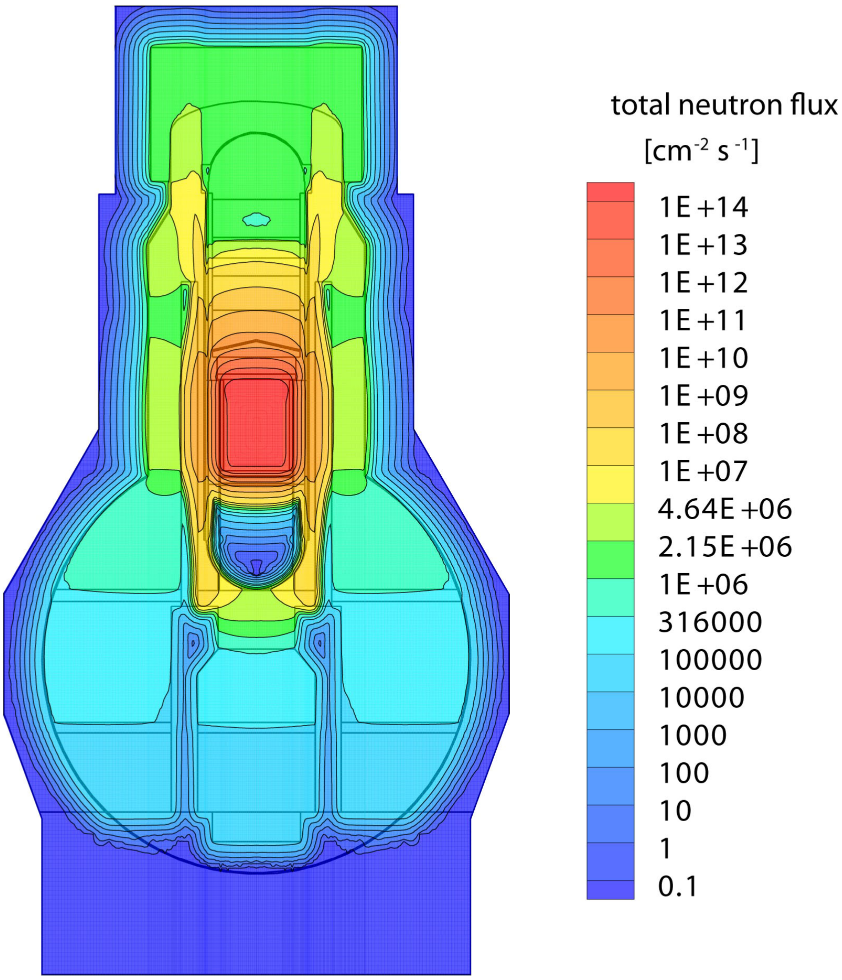

Figure 7: Total neutron flux distribution in KKM (2011 model) [73]

version of previously-used GRSAKTIV [70], developed specifically for Nagra.

Cells composed of mixed materials, such as reinforced concrete, would be activated several times, once for each material (in this example, concrete and steel). The final result was the specific activity for all nuclides with significant activities listed for each cell and each associated material, output in CSV file format. As an overview, the results for Co-60 specific activity were also presented graphically, with each cell (as defined in figure 8) shaded according to a selected color map.

As illustrated in figure 5, these models are validated for neutron transport accuracy using foil activation campaigns. This is described in section 3.4.

This methodology was applied in 2011 to characterize the decommissioning waste associated with all four Swiss NPPs[75–78]. These results were then used for KS2011 and KS2016.

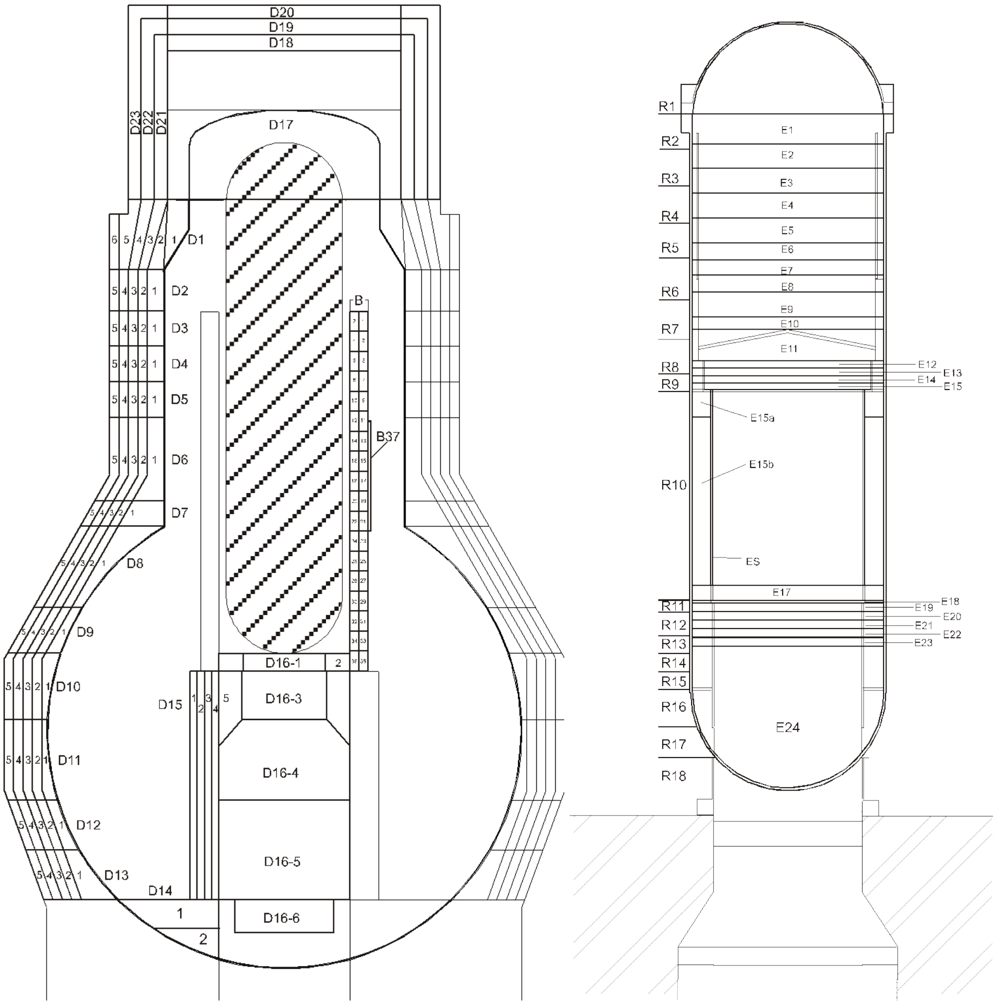

(a) Bioshield and drywell

(b) RPV and reactor internals

Figure 8: KKM activation zone map (as used for KS2011) [75]

3.2 NEW ACTIVATION CODE SEQUENCE

The methodology described in section 3.1.2 already delivers much of the desired characterization results described in the introduction. The activation calculations produce full nuclide vectors (not just the lead nuclides). The associated models have captured major streaming paths, delivering more accurate results than the previous methodology (from section 3.1.1), thus reducing the need for conservatism.

However, several areas of improvement were identified since the first definition of the methodology:

- **Fully three-dimensional models.** The rotationally-symmetric models of NPPs by definition leave out the details that vary with the angle. This includes many important streaming paths, such as bioshield openings, which are essential for the neutron transport beyond the bioshield.

- **Detailed component-wise activation distribution.** Especially when core internals (being highly activated components) are homogenized, one cannot properly describe the distribution of the activation in each component. This is essential for planning of the segmentation strategy, where a high resolution of the activity distribution is necessary for informed decision making.

- **Detailed core model.** The shape of the core has a significant influence on the activation of nearby components. Given the FA arrangement in the core, and the variation of their burnup and neutron poison loadings, the real power distribution is heterogeneous. When the power distribution is averaged over all nodes (of a particular axial level) this heterogeneity is not captured. Therefore, the core needs to be modeled on the nodal level to address these points. Furthermore, for BWRs, the void distribution in the core is also highly heterogeneous and too must be captured on the nodal level. This is essential for accurate transport calculations in BWRs to capture the radial and axial neutron leakage.

- **Transition to a new depletion code.** GRSAKTIV-II is an old code, which is no longer maintained. Furthermore, a comparison of depletion codes conducted at Nagra [79] identified ORIGEN [23] to be a better choice, based on numerical stability and overall performance.

- **More automation.** The methodology described in section 3.1.2 delivered results in CSV format. All further post-processing of results had to be manually, with direct manipulation of data sets. Similarly, the data transfers between codes were handled manually. This increased the time intensity of the analysis and created plentiful opportunities for user error. As such, a more automated solution is desired.

- **Optimized component segmentation strategy.** Once each component is characterized in detail, it's possible to suggest a more realistic segmentation strategy and develop a more efficient packaging concept. This will yield a reduced and optimized number of waste containers and types.

- **Rapid waste volume determination** In order to plan for the decay storage, it's necessary to know the total waste volume following decay periods of varying length. To address this, it's desirable to have a capability to quickly (and with minimal user effort) calculate the volume of waste fulfilling user-defined criteria, such as specific activity or the sum rule value range. The results ought to be available in numerical format (calculated volume or percentage of each component mass) as well as graphically (in form of isolines).

- **Extension of the validation** In the past, the flux distribution has been validated using foil activation campaigns in a number of Nagra models. In order to have high degree of confidence in the new models, it's desirable to extend the validation. This will include additional foil activation campaigns, as well as direct activity measurements of the actual activated components (see section 3.4).

- **Dose Rate Calculations** Some of the activation products emit high energy gammas, which can lead to a significant gamma dose rate arising from an activated component. As part of decommissioning planning (for shielding design, working dose predictions) it's desirable to have the capability to calculate the gamma dose rates fields surrounding the activated components based on the nuclide inventory.

All of these improvements have now been implemented into the activation methodology. Its new, updated form is summarized in figure 9 and described in this section. The developments of the MCNP models (including the detailed core modeling) are described in section 3.2.1. The new coupled code sequence for activation (using ORIGEN and offering increased automation) is presented in section 3.2.2. The methodology developed for optimized component segmentation is explained in section 3.2.3. The validation campaigns carried out so far, and the ones planned for the future, are described in section 3.4. The waste volume calculation capability and the dose rate calculations are both presented in section 3.5.

3.2.1 Detailed three-dimensional models

With the gradual improvements in the implementation of variance reduction (VR), described in section 3.3, it became possible to extend the NPP MCNP models and increase the level of detail of components (in cases where it affected the transport or accuracy of activation results) while keeping the computational intensity at a reasonable level.

MCNP is a versatile code that allows the addition of any desired level of detail. The limiting factor, and the biggest challenge with regard to NPP modeling, is the availability of the supporting documentation—that is, detailed technical drawings and material information. In cases where documentation wasn't sufficient (or completely missing), the information pool was extended during in-person NPP visits by conversations with corresponding NPP experts, photographing the reactor building compartments, as well as by comparisons with technical documentation from other (preferably similar) plants.

The lack of information was particularly problematic with material information. While the NPP operators generally know the base material for each (large) component, there is very little knowledge about the impurities within these materials. These impurities are essential for activation characterization [68].

For some components (e.g., drywell concrete) it was possible to organize material characterization studies, extracting a sample and measuring the base elemental composition and the concentration of impurities through chemical analysis techniques. However, many components cannot be accessed (most RPV internals) or a sample cannot be extracted from them for safety reasons for an NPP still in operation (e.g. the RPV wall). In the

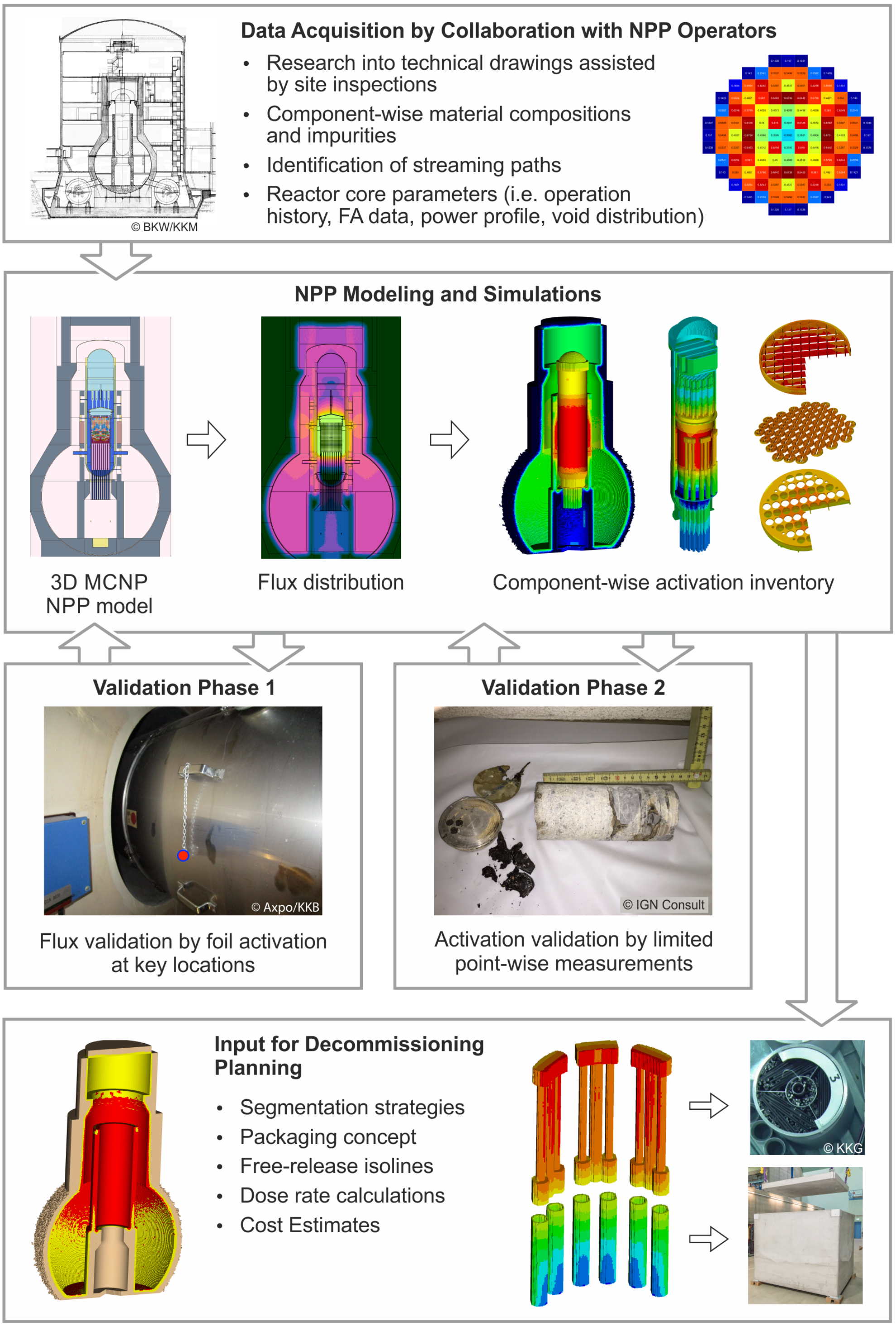

Figure 9: Nagra 2018 Activation Analysis Methodology

end, the following sources of material description were used (in decreasing order of accuracy):

- direct chemical measurements
- measurements done in similar NPPs for the same material
- impurity measurements for other, but similar, materials (e.g. impurities in RPV steel based on carbon steel found in rebar)
- literature values (particularly from [80], providing an overview of numerous measurements from components of decommissioned US NPPs, but also general material definitions [81] and standards [82])

Note that literature values for any given impurity sometimes vary by as much as an order of magnitude. Additionally, the variation of impurity concentration throughout each component is also generally unknown. While this is not expected to lead to large additional uncertainties, it does represent an additional (albeit limited) influence on the final result. Overall, the material definition represents the biggest source of uncertainty for the activation calculations. In comparison, the uncertainty due to nuclear data has a comparatively minor impact [83].

While it's possible to have a high level of geometric detail throughout the NPP model, this is not the optimal approach. For components located close to the active core (internals, RPV), it's very desirable to model them in detail, since this increases the detail of the final activation distribution result, to be used for choosing the segmentation strategy. However, rooms or areas located far away from the core, whose activity levels are near the release limit, and where (because of the empty room assumption) the uncertainty (i.e., the overestimation) of the flux is greater [73], don't necessarily have to be modeled in detail. Most importantly, the general shape of the surrounding (or intersecting) walls must be captured. On the other hand, gaps and openings serving as streaming paths for neutrons need to be modeled in the maximum possible degree of detail, in order to accurately capture neutron transport through these areas. Overall, visually, the improved models generally appear to be very detailed near the core, with the degree of detail decreasing with the increasing distance from the core. This can be seen for example in figure 10, showing the latest version of the KKM MCNP model.

Following this design approach, the MCNP models of all Swiss NPPs have been updated. Firstly, a side room was added to the model of the KKG [84], and the flux calculated there was validated using foil activation [85]. Afterwards, the MCNP model of the KKM was updated to include many non-symmetrical features, including pipe openings in the RPV (reactor pressure vessel) and bioshield [73, 86]. These new details improved the accuracy of the neutron transport (since additional significant streaming paths were now modeled explicitly), and at the same time improved the accuracy of the activation calculations of these components, which were now represented in greater detail. The latest version of the model can be

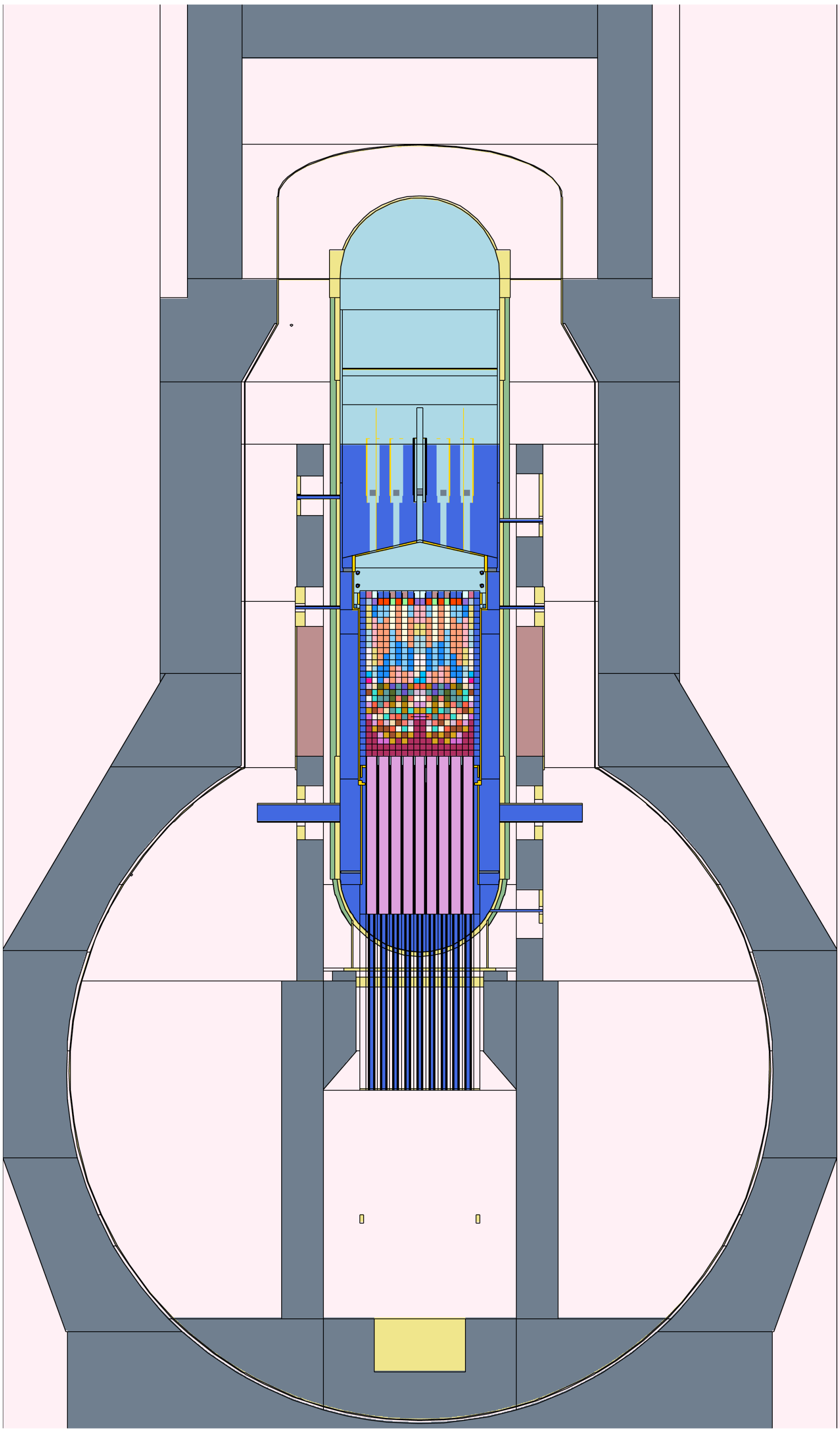

Figure 10: MCNP model of KKM [75] (2018 version, to be used for KS2021)

seen in figure 10. Similarly, the KKB model was updated to a higher degree of detail [87]. The updates of the KKL and the KKG models are currently ongoing, scheduled to deliver results in 2019.

In connection with these model updates, numerous flux validation campaigns, based on foil activation measurements, have been carried out in KKM (twice), KKG, and KKB. The KKL and a second KKG validation campaigns are currently in progress, with samples already placed into KKL, and KKG samples ready for placement. The exact validation approach is described in section 3.4. These validation campaigns are crucial to the understanding of which parts of the NPP are important to be modeled in detail, as well as to assess the overall accuracy of the simulated neutron transport.

With the components modeled explicitly with a larger degree of detail than before, it became necessary to also improve the modeling of the active core. As was explored in [88], both real core shape and accurate power profile have a strong impact on the total flux at the core boundary. This effect has a particularly significant impact on nearby components. Looking at the (BWR) core barrel, when comparing the real core shape and a cylindrical core (as was the case in 2011 models), the circumferentially-averaged total flux was twice as high for the real core shape case, due to strong contribution of the core areas much closer to the core barrel than the radius of the cylindrical core. Similarly, when comparing the real core shape with a nodal power distribution to a core of the same (real) shape, but with homogeneous power distribution, the circumferentially-averaged total flux at the core barrel was half as high for the nodal power distribution. This was caused by the fact that the outermost assemblies, which contribute the most to the radial leakage, have lower power than the assemblies in the middle of the core. Furthermore, axial leakage was similarly affected, particularly in the top part of the core, where the difference was approximately factor 3. As such, accurate modeling of the core shape and power distribution is paramount.

For these new detailed models, the active core is modeled to fully capture the information provided on nodal level by the NPP operators [73, 88]. As such, the core is defined as a repeating structure (i.e., an MCNP lattice) made of rectangular elements representing the FA nodes. Each FA is then split into a number of axial nodes (typically around 25). Each node has its own power value (or MCNP particle emission probability), which exactly matches the provided data, but it can share the same material card with any other distant node (i.e., there is no need to create one material card per node). Naturally, due to the MCNP lattice syntax, the input lines for the source term become very long and complex. For this reason, an automated script has been developed, significantly reducing the engineering work necessary for creating the core model. At first, the script user must provide the core shape, the nodal void fraction data, the nodal power data, and the geometrical details of a reference FA type (i.e., the most common in the core). The latter include the number of fuel pins, water rods, and partial length fuel rods, as well as the diameter of the pellet, gap and cladding, and the dimensions of the FA box. In reality, the burnup varies strongly between assemblies, with the distribution in the core being highly heterogeneous. However, as was explored in [68, 73], when the model is run is source-term mode and criticality is disabled (using the MCNP *nonu* card), the burnup of the fuel is of low importance. This is because without fission, only the total neutron absorption cross section is important. This cross section doesn't change significantly between fresh and highly-depleted fuel. For this reason, for the purposes of these calculations, the same fuel composition is used for all fuel rods in all fuel assemblies in the core. For consistency, the composition was chosen to be representative of the (high-burnup) assemblies in the outermost parts of the core, which are responsible for the majority of the radial neutron leakage. With fuel composition and the lattice taken as constant for all fuel assemblies, the overall (homogenized) material composition of each node is only a function of the (coolant) void fraction. (That is, other than the void fraction, all other parameters remain constant.)

Using the received information, the script performs a volume balance and obtains the nodal density for each node. While the lattice materials are always the same, the void fraction changes across the nodes, causing the density to vary. At this point, the script user has the freedom to decide the number of MCNP material cards to be devoted to the core. Each node will be assigned the MCNP material which most closely matches its homogenized material composition. It's therefore necessary to choose a sufficient number of materials, in order to accurately capture the variation of nodal density (caused by the variations in the void fractions). If desired, the core can be axially split into two parts, with top and bottom parts each getting their own set of separate material cards. In this way, it is possible to take into account the partial length rods.

Each element of the lattice is then assigned a corresponding material card and its own nodal power value, reproducing the nodal power profile exactly matching the provided data. Figure 11 shows the relative probabilities of a new particle being created (by MCNP) assigned to each node by the core script.

Finally, the script automatically generates the MCNP input necessary to model such a complex source term, ready to be pasted into the MCNP input file. As such, it's possible to test different core configurations with minimal effort and engineering time investment.

In the past core design, such as the one described in section 3.1.2, a large portion of the core was set to be inactive. That is, only the two outermost FA rows emitted particles, except for a number of top and bottom nodes, which were deemed important for axial leakage. This was done to increase computational efficiency, since virtually all of the neutrons which reach the RPV come from these regions. However, this assumption is not as suitable for activation of reactor internals, some of which are located very close to the core (e.g. core support grid or the core barrel). Additionally, the presently employed variance reduction tools, described in section 3.3.5, automatically account for the relative importance of individual regions for the tally result. As such, presently, the whole core is modeled as active.

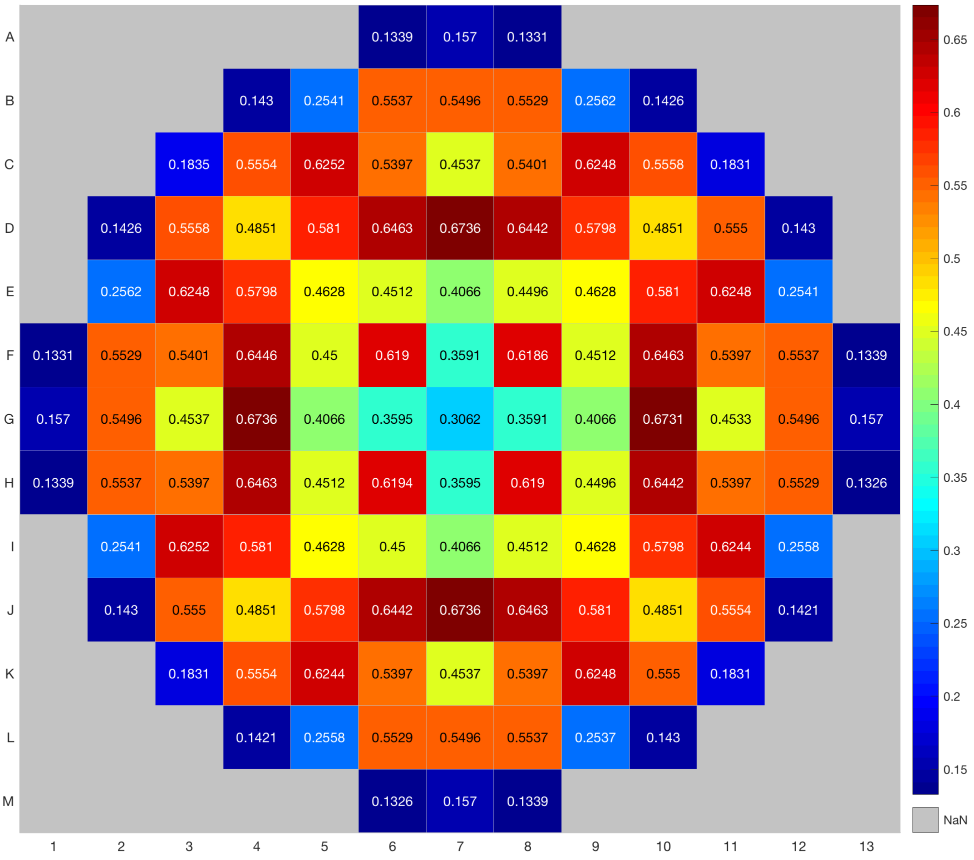

	1	2	3	4	5	6	7	8	9	10	11	12	13
A						0.1339	0.157	0.1331					
B				0.143	0.2541	0.5537	0.5496	0.5529	0.2562	0.1426			
C			0.1835	0.5554	0.6252	0.5397	0.4537	0.5401	0.6248	0.5558	0.1831		
D		0.1426	0.5558	0.4851	0.581	0.6463	0.6736	0.6442	0.5798	0.4851	0.555	0.143	
E		0.2562	0.6248	0.5798	0.4628	0.4512	0.4066	0.4496	0.4628	0.581	0.6248	0.2541	
F	0.1331	0.5529	0.5401	0.6446	0.45	0.619	0.3591	0.6186	0.4512	0.6463	0.5397	0.5537	0.1339
G	0.157	0.5496	0.4537	0.6736	0.4066	0.3595	0.3062	0.3591	0.4066	0.6731	0.4533	0.5496	0.157
H	0.1339	0.5537	0.5397	0.6463	0.4512	0.6194	0.3595	0.619	0.4496	0.6442	0.5397	0.5529	0.1326
I		0.2541	0.6252	0.581	0.4628	0.45	0.4066	0.4512	0.4628	0.5798	0.6244	0.2558	
J		0.143	0.555	0.4851	0.5798	0.6442	0.6736	0.6463	0.581	0.4851	0.5554	0.1421	
K			0.1831	0.5554	0.6244	0.5397	0.4537	0.5397	0.6248	0.555	0.1831		
L				0.1421	0.2558	0.5529	0.5496	0.5537	0.2537	0.143			
M						0.1326	0.157	0.1339					

Figure 11: core power distribution, as assigned by the core script [87]

3.2.2 New Hybrid Activation Methodology

In order to address the objectives described at the beginning of section 3.2, specifically the usage of a new depletion code and increased automation, allowing quick processing of large results data sets and therefore detailed component-wise activation characterization, a new cooperation project was initiated with the Oak Ridge National Laboratory (ORNL) to develop such a functionality.

ORNL has previously developed a methodology for shutdown dose rate calculations using hybrid Monte Carlo and deterministic techniques, where Monte Carlo neutron transport results are passed to ORIGEN for activation calculations and definition of a photon source for a subsequent Monte Carlo photon transport (to calculate the dose rate) [89]. For the purposes of the Nagra Activation Analysis Methodology, the first part of this methodology (i.e., neutron transport and activation) was taken and adjusted to output nuclide number densities instead of a photon source definition. Furthermore, a new module was developed to post process these number densities into other units of interest (e.g. nuclide-specific activity (in Bq) and specific activity (in Bq/g)) and graphical output [90].

Code Sequence

In order to explain the full code sequence, first consider the diagram shown in figure 12, which illustrates that activation calculations require three types of input: flux information, material definition (including impurities), and the NPP operation history.

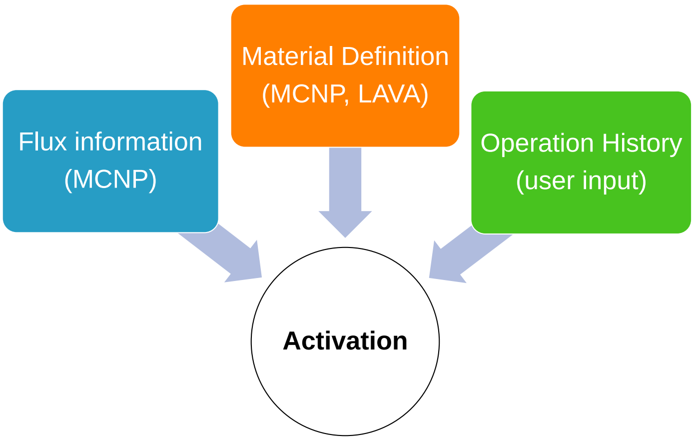

Figure 12: NPP activation calculation inputs

The flux information is captured from the MCNP model of the NPP in question using a rectangular type-4 mesh tally, which records flux information in a number of energy bins. The neutron transport uses the default MCNP 6.2 ENDF/B-VII.1 cross section library. The present methodology is energy group structure agnostic and can work with any energy bin definition the user chooses. Since the MCNP calculation is steady state, the source definition used for this calculation needs to be representative of the nominal NPP operation conditions. If that is not possible (e.g. high-leakage cycles during early cycles), the solution can be split into two separate calculations, with these other cycles treated separately and final results being the sum of the two parts (with appropriate decay times applied to the early cycle results). Alternatively, the difference in leakage could be approximated using a factor, applied to the real power. For the case of high-leakage, the factor is approximately 2 [91]. Naturally, variance reduction (as described in section 3.3) is used here to improve the efficiency of the calculation. The output for this information type is an ASCII meshtal file.

Material definition is based on LAVA, the ray-tracing module included with ADVANTG [92] code. For the purposes of this calculation, standard ADVANTG executables are used. The input is set to ray-tracing-only mode (dx) on a mesh that exactly matches the mesh tally from the aforementioned MCNP run. Note that while it is possible to use the same MCNP input for both, it is generally desirable to use a modified MCNP input file for the material definition. Since only the material definition of the investigated component is needed here, it's useful to change the other surrounding materials to void, so that their mass is not considered for the activation calculation. For example, this allows the removal of surrounding water (which is only important for transport). This approach also allows the use a simplified material definition for the transport calculation and include the impurities only during this material definition ray-tracing run (or even vary their concentration for a sensitivity study). The output for this information type is a series of files automatically output by an ADVANTG run.

The operating history is provided by the user via an input file, where two vectors are defined: time-step vector and the corresponding power-level vector. The time-step vector has units of seconds, while the power-level vector has units of neutron source strength (corresponding to the MCNP flux information calculation), for each time step. There is an option to define a multiplier constant for either vector that will be applied to all its values. This can be used to for example convert time from seconds to days, or power from neutrons per second to MW.

The activation code sequence reads the meshtal file for flux information, ADVANTG-generated files for material information, and the input file for operating history. All this information is sent to ORIGEN via an API (Application Programming Interface) [93]. ORIGEN carries out the calculations and returns the resulting number densities for all nuclides. At this point, no specific nuclides are selected – all nuclides present in the ORIGEN library are considered.

A post-processing module is available to process these results and convert number densities to activity (Bq) or specific activity (Bq/g), whichever suits best to the task at hand. (For example, the specific activity directly reveals whether a material can be freely released, based on regulatory limits, defined in Bq/g.) The results are output, in the desired units, for each nuclide defined by the user (in the input for the post-processing code) in the form of a CSV file, following the structure of the mesh tally. That is, a table showing the results for each x and y bin is printed for each z bin. For example, a mesh tally with 10 bins in x, 20 bins in y, and 50 bins in z will result in a CSV file (for each nuclide of interest) containing 50 tables with 20 rows and 10 columns each. These CSV files allow for a convenient data analysis using standard spreadsheet software packages, including the calculation of the total and average activity, as well as find the maximum (component hotspot) and the (non-zero) minimum.

At the same time, the post-processing code converts the results (again in either unit) to a 3D graphical format in the form of a SILO file, readable using the VisIt software [94], where the results can be represented in a variety of ways. This is very useful to get an overview about the investigated component, see the hotspots and the variation of the magnitude of activation.

Example Results

In order to demonstrate the aforementioned graphical output capability, and at the same time describe the typical activation distributions, it's useful to take a closer look at example results.

This section will focus on the activation distribution inside KKM, as described in [90, 95]. All figures show the specific activity of Co-60, the lead nuclide for immediate dismantling and packaging concepts.

As a first example, consider the core support plate (shown in figure 13). This stainless-steel component is located just below the active core. The circular plate is perforated with holes, which house FA feet, to which the FAs are connected. Below the horizontal circular plate are vertical plates arranged into a grid. This can be seen at the bottom of figure 13, where the plate is hidden from view. As KKM is a BWR, control rod blades pass through this bottom part, with each FA foot having a special cross-shaped opening for them.

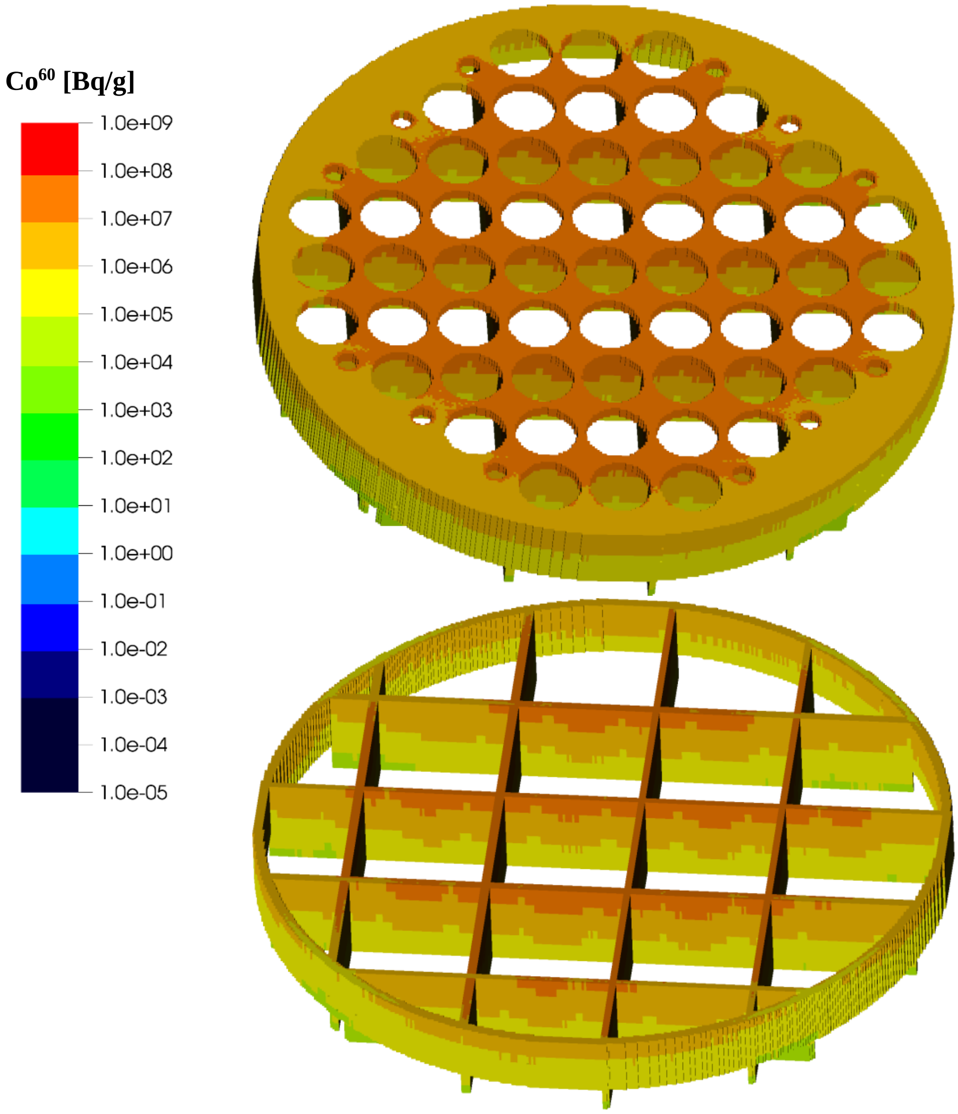

Figure 13: Co-60 activity distribution in the KKM core grid, shown with and without the top plate

Given the close proximity to the active core, this component is highly activated. The mean Co-60 specific activity is 6.41e6 Bq/g. The maximum is 7.26*e*7 Bq/g resulting in a component max-to-mean ratio, referred to as the *hotspot factor*, of 11.3. This factor quantifies the risk of a local hotspot appearing in a cask loaded with segments of the component in question, as compared to an idealized homogeneous loading based on perfect mixing of all the component segments. The minimum is 1.44*e*4 Bq/g, so the activity varies by 3.7 orders of magnitude.

Compared to other RPV internals, this activation is relatively homogeneous. Given the total weight of the component of around 3 t, which means that it will be subdivided into several casks, the hotspot factor of 3.7 is manageable with an adequate segmentation and loading strategy. Overall, this kind of a rather homogeneous activation profile has only a limited potential for segmentation optimization (and therefore savings in the number of casks), as all parts of this component will likely be loaded into the same type of cask with the same level of shielding.

The core shroud (shown in figure 14), on the other hand, shows a much larger variation in its activity distribution. This component surrounds the active core, separating it from the downcomer (located on its outer side). As such, parts of it are very close to FAs. However, the component extends down below the active core, to the region containing control rod blades and a lot of water, leading to very low neutron fluxes and therefore low activation.

The mean specific Co-60 activity is 8.16*e*7 Bq/g, but the maximum is 5.08*e*8 Bq/g—the highest value of any KKM RPV internal! This results in a component hotspot factor of 6.2. The minimum is 1.38*e*–4 Bq/g—that is, 0.14% of the release limit. Overall the Co-60 activity varies by 12.6 orders of magnitude.

As can be seen in figure 14, this huge variation is distributed axially, with component parts surrounding the active core being more active than the component parts surrounding the control rod blade region (as one would expect). Consequently, the upper part of the component ought to be packaged into a different type of cask than the lower part (which could even be free released, assuming no contamination). Therefore, unlike the core grid before, this component has a large potential for segmentation and packaging optimization.

One approach is to manually split the component into several sub-components, based on the observation of the results. In this case, one could for example divide the component into two sub-components at the axial height corresponding to the bottom end of the active core, and consider each of them separately, picking a different type of cask for each. This leads to a much more optimal solution than when considering the component as a whole, but it’s still far from the global optimum solution. For components with this much variation in activity, a lot of trial and error attempts would be needed to find this "best" solution through manual methods. To address this, the segmentation of such components is analyzed using an algorithm.

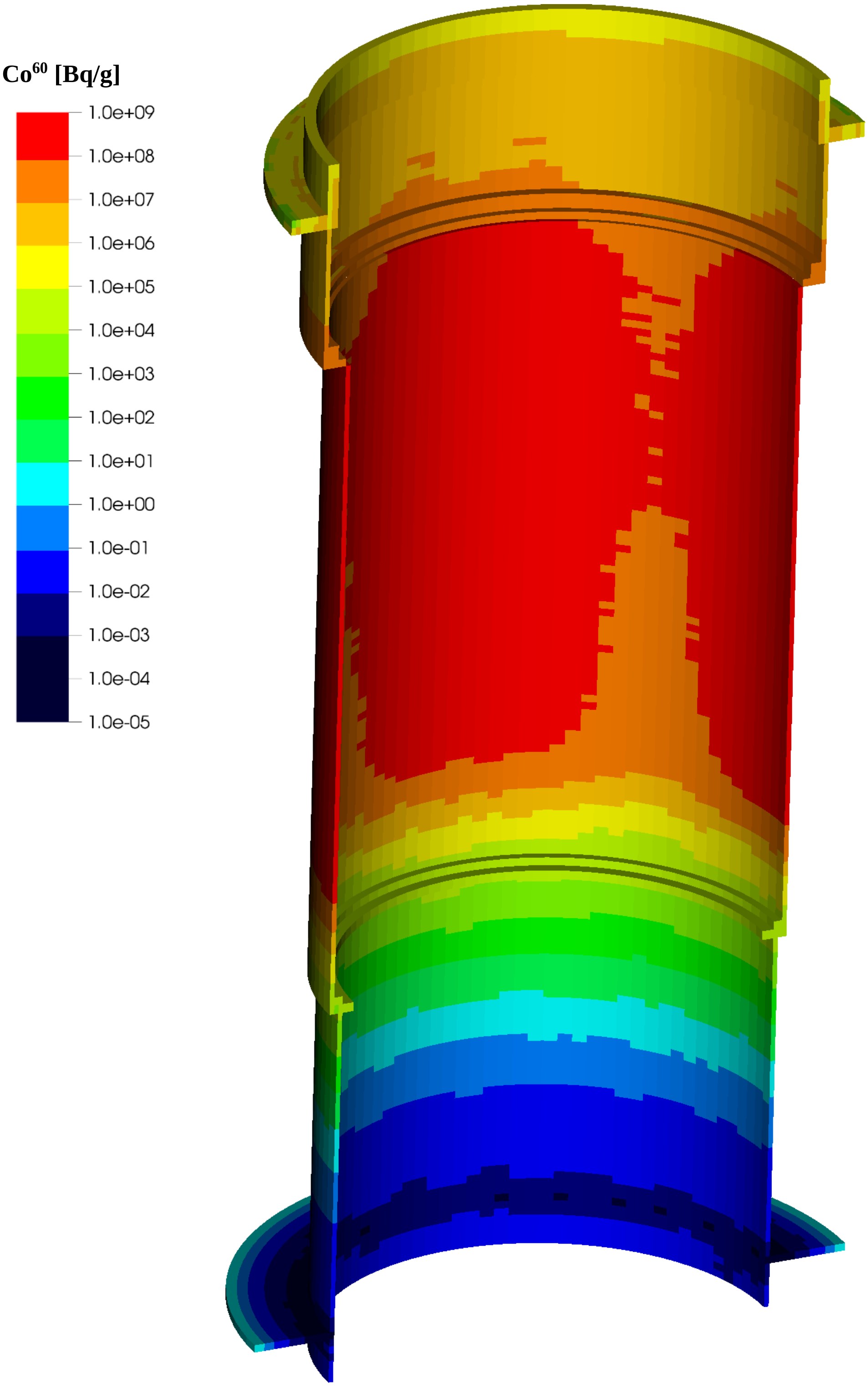

Figure 14: Co-60 activity distribution in the KKM core shroud

This is described in section 3.2.3.

The two example components show the two "extreme" cases - a rather homogeneous activation profile (with limited optimization potential) and a activation profile with a very large variation (with a large optimization potential). The other internals can be found in between.

Figure 15 shows the activation distribution of other components, specifically steam dryers, upper core grid, and fuel assembly feet, as well as a combined figure, including all the RPV internals (excluding fuel and control rods) and the RPV itself.

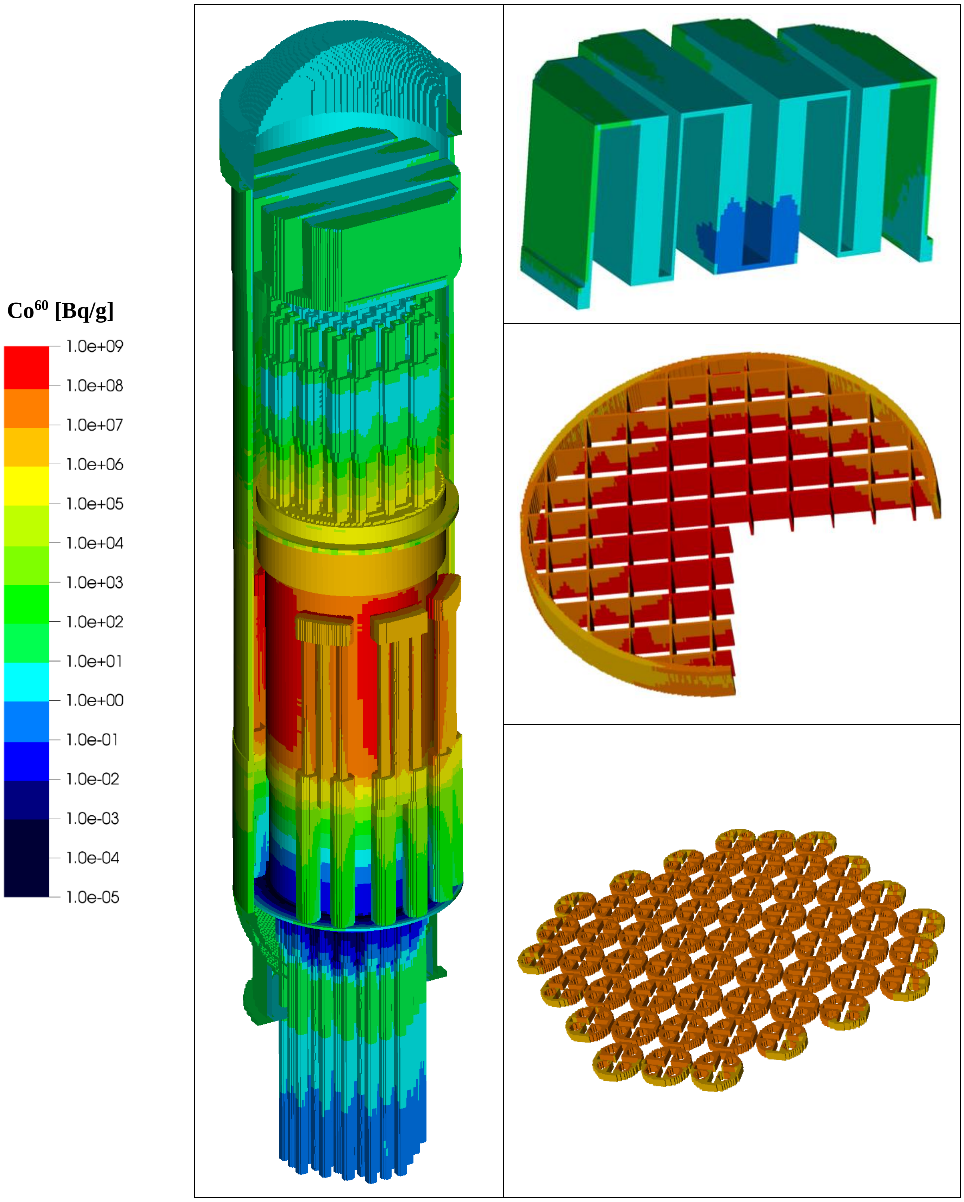

Figure 15: Component-wise activation characterization of KKM RPV and internals (with a close up view of steam dryers, upper core grid, and fuel assembly feet)

3.2.3 ALGOPACK Optimized Packaging

Detailed knowledge of component activation distribution provides the necessary input for segmentation and packaging planning. In order to ensure efficient component segmentation, and in general to optimize the packaging concept, an algorithm called *ALGOPACK* (Algorithm-Optimized Packaging) was developed.

For a given activation distribution data set originating from the Nagra Activation Analysis Methodology, ALGOPACK finds a packaging concept which minimizes the total container cost. The selection is based on the available LLW and ILW containers (as defined by the utility - see also section 3.5.1) and their corresponding volume and activity limits (acting as constraints).

This problem corresponds to the general description of a *two-dimensional vector bin packing problem with variable bin sizes* [96]. Following this description, the packing problem is first formulated in mathematical notation [97]. These can then be solved using existing solution algorithms [98]. However, compared to the generic cases, the segmentation and packing optimization problem at hand has some unique constraints. Specifically, it is expected that the component will be segmented in a single direction (e.g. from top to bottom), with the removed segment (after any further cutting, as required) being immediately placed inside the selected container before removing the next segment. It is also expected that a container will have to be fully filled (and closed) before another container can be selected, leading to a continuous sequential packaging. Note that in the future, this constraint is planned to be relaxed, with the number of simultaneously open containers, each being of any available container type, defined by the user. However, as the first step, only the (most likely) single open container assumption was implemented. The mathematical formulation of the problem and the aforementioned constraints were all incorporated into a custom solution algorithm, ALGPOPACK, written in Python [99].

Before the ALGOPACK calculation, the activation distribution data set is processed based on the chosen segmentation direction, reducing it into a single dimension (corresponding to the direction of segmentation). Consider for example the core barrel shown in figure 16. In order to convert it into a one-dimensional data set (going in the axial direction), the specific activities are homogenized across the radial and angular discretization (corresponding to the original activation mesh). The result is then a single-dimensional description of this component's activation profile. For each homogenized cell, referred to as node, it contains the average specific activity (for each nuclide), maximum specific activity (based on the maximum over all homogenized cells), and the total mass (based on the total mass of the activation cells represented by the node in question). Note that the node height, labeled h on figure 16, corresponds to the axial grid discretization dimensions, as defined during the activation calculation.

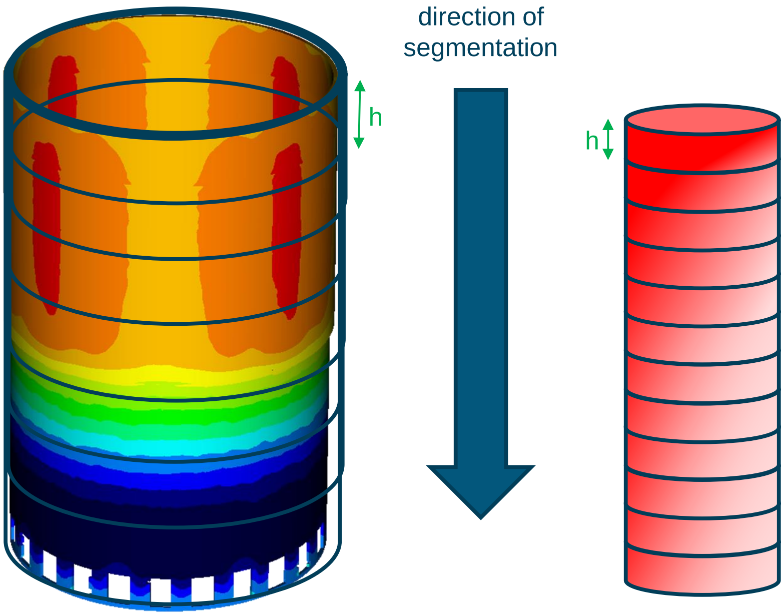

Figure 16: ALGOPACK: interpretation of the activation distribution data

The core challenge solved by ALGOPACK is the identification of the most preferential container, performed at the beginning of the segmentation process and following each closure of a full container. To identify the ideal container, dynamic programming is used to evaluate for each available container type the corresponding most-efficient packing (given the segments next in line to be packaged), as constrained by the volume and activity limits. The container is then selected, which contains the highest volume of packaged segments (while satisfying all constraints, including packing density and hotspot factor limit).

This is demonstrated in figure 17, where three potential MOSAIK cask options are compared. The algorithm loads each cask with nodes, checking the total mass and activity limits. The mass limits is based on the knowledge of the maximum certified cask mass (for transport) and a *user defined packing density*, based on prior experience (such as [100]). The activity limit is based on the certified cask maximum activities for the nuclides in question—for internals, this is generally only Co-60. Additional checks are carried out for the fulfillment of defined safety constraints. This may include a safety factor for activity values (to compensate for the uncertainty) and a hot-spot limit, defined as the ratio between the maximum specific activity (based on the single "hottest" cell in the current container loading) and the cask-average specific activity. This is done to avoid significant activity hotspots, which may lead to localized high dose rates on the surface of the cask.

The algorithm proceeds to load each cask until either the mass or the activity (including the additional safety checks) limit is reached. The script then evaluated how much mass could be fitted into each cask and picks the option that accepted the highest amount of mass. In the example in

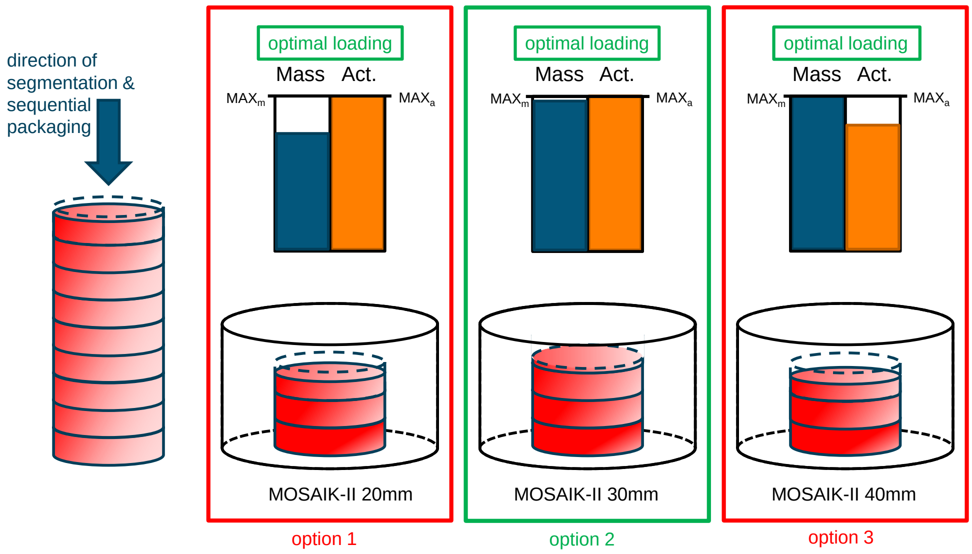

Figure 17: ALGOPACK: evaluation of the cask options

figure 17, option 2 fitted the highest amount of the component mass, and as such was chosen by the algorithm.

This procedure is then repeated until the whole component is packaged. The whole algorithm is represented in the form of a flow chart in figure 18.

In order to compare the performance of ALGOPACK against the manual method (based on splitting the component into sub-components and manually picking a cask type), a test case was developed. In this test, RPV internals based on KKM were activated and packaged (in accordance with the aforementioned limits). The activation calculation used literature values for material (and impurity) compositions and a generic irradiation history. Therefore, even though the components geometrically resemble the KKM internals, the results do not correspond to the KKM packaging concept. The test case results are summarized in table 5.

Table 5: Number of containers required to package selected BWR core internals. The numbers are reported as # MOSAIK casks / # LC-84 containers.

Component	Manual	ALGOPACK
Shroud	50/2	38/3
Core Support Plate	7/0	7/0
Core Sprays	2/0	2/0
Steam Separators	8/4	7/4
Steam Dryers	0/3	0/3

From these results it can be seen that in all cases the algorithm-produced results are as good or better than the manual method ones. The two approaches diverge as the size of the component grows and the algorithm finds the (global minimum) optimal number of container types, and there-

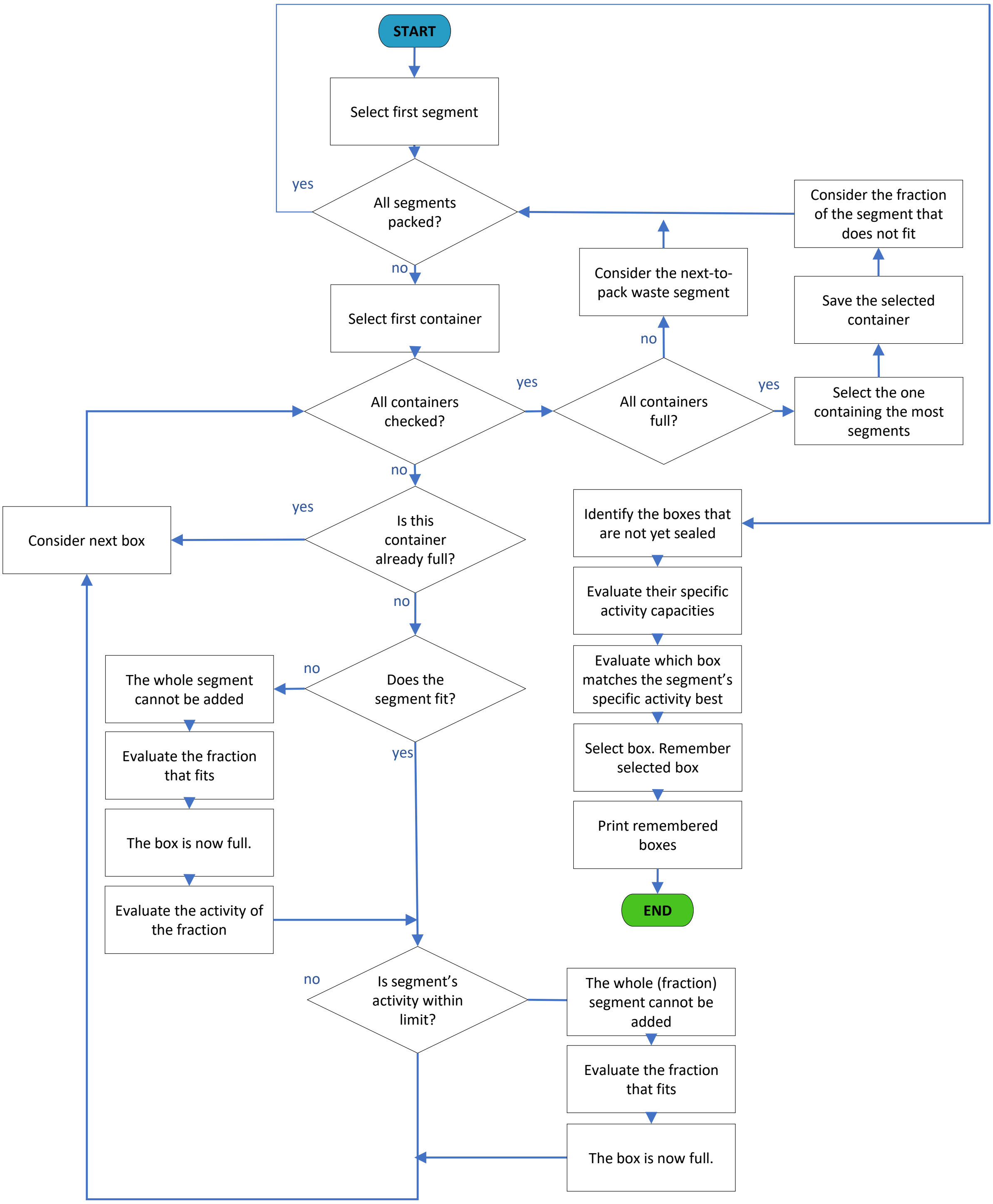

Figure 18: ALGOPACK: flow chart of the underlying algorithm

fore more efficient packaging.

It's important to note that the approaches were not constrained equally. While ALGOPACK strictly followed the defined hotspot and loading mass/activity limits, the manual approach allowed for "educated guess" of an approach feasibility, e.g. when the mass limit is exceeded by a very small fraction, deemed negligible in comparison to the coarsely approximately fill fraction.

It should be noted that, since the segmentation procedure has not yet been finalized, the defined boundary conditions are too expected to develop over time. Variations between the segmentation procedures of individual NPPs is also expected. As more information about the respective planned procedures will become available, ALGOPACK will evolve alongside.

3.3 VARIANCE REDUCTION

In a typical NPP MCNP model described in this chapter, the flux in regions of interest ranges by more than 16 orders of magnitude. This, together with the presence of numerous neutron streaming paths, leads to an extremely difficult neutron transport problem, requiring humongous amounts of computational time. In order to obtain precise results within a reasonable amount of time on a single-CPU workstations available at Nagra, it is imperative to accelerate the calculations.

For a stochastic code like MCNP this can be accomplished by biasing the random walk of the tracked particles in a way to more frequently sample those histories, which most contribute to the targeted result (tally), all while maintaining the statistical validity [101]. This is referred to as *variance reduction* (VR). In this section, the two most common methods of VR are explored: cell-splitting (section 3.3.1) and the (built-in MCNP) weight-window generator (section 3.3.2). This is followed by a description of more advanced VR techniques: hybrid-VR with the *ADVANTG* code (section 3.3.3) and the use of DXTRAN spheres (section 3.3.4).

3.3.1 Cell-splitting

One technique to preferentially drive particles into regions of interest involves splitting the geometry into sections and assigning them different importance values, such that they increase in the direction in which it's desirable for particles to move (e.g. through layers of shielding).

The individual cells are subdivided into a number of smaller cells, with importances (I) defined for each cell. When the tracked particle crosses the boundary between cell n and cell $n+1$, their relative importance is considered. If $I_{n+1} > I_n$ then the particle is split into $\frac{I_{n+1}}{I_n}$ particles, with their weight adjusted by $\frac{I_n}{I_{n+1}}$ (times the original weight). On the other hand, if $I_{n+1} < I_n$, then the tracked particle undergoes a Russian roulette, with a chance of survival of $\frac{I_{n+1}}{I_n}$. If it survives, its weight is increased by $\frac{I_n}{I_{n+1}}$. If it doesn't, its weight is set to 0 and the particle is no longer tracked.

This technique has been employed extensively over the history of MCNP [68, 101]. Its application is generally intuitive (at least for cases with a single predominant transport direction of interest) and quantifiable—the user can track the success of applied importance set by looking at the number of particles in each cell (cell populations)—which she ought to keep approximately constant. However, the use of this technique requires modification of the geometry, which increases the geometrical complexity of the model (with the number of cells often increasing by more than an order of magnitude) and potentially requires a lot of engineering time to implement these changes. As such, its use is nowadays generally restricted to simpler MCNP transport problems.

3.3.2 MCNP Weight Window Generator

In order to avoid the need to modify the geometry and in an effort to provide new features, the functionality of cell-splitting was later extended into a new technique—the *weight windows* (WW) [102]. Instead of splitting each cell into a number of smaller cells, the whole geometry is here overlaid with an independent, user-defined mesh structure. Each mesh cell is assigned a weight, which acts similar to the cell importance described previously, except that the initiation of splitting or Russian-roulette depends on the particle weight rather than the adjacent mesh cells. That is, each mesh cells has a bound of weights, with an upper and a lower bound. As such, splitting or Russian roulette only have to be performed when the particle weight falls outside of the bounds, rather than at each cell boundary. With the dependence on cell boundaries gone, the technique also introduces energy dependence. That is, weight-windows are space-energy dependent. The whole technique is summarized in figure 19 below.

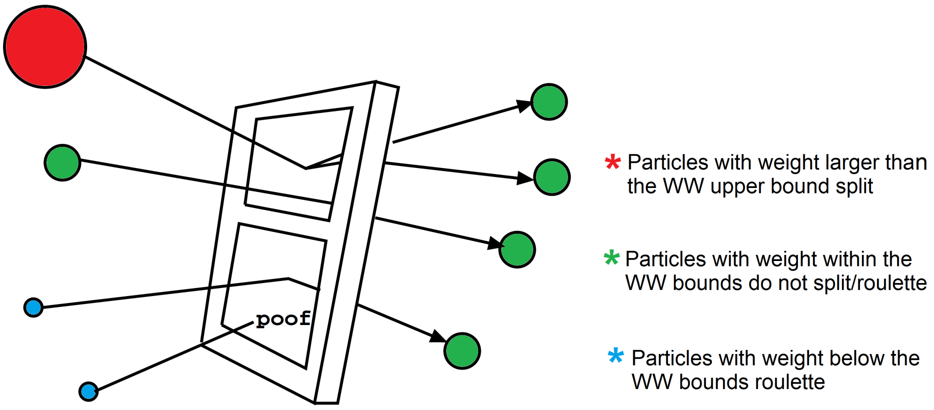

Figure 19: Weight window VR technique [68, 101]

Weight windows can be generated using a weight window generator (WWG) built into the MCNP [102]. In order for WWG to work, some tally response is required. This response is then used to calculate the importance of each (energy-space) mesh cell, depending on the (weight-weighted) fraction of the tally-scoring particles which have passed through this cell, producing an importance map, which is then used to define the individual weight bounds.

Since tally response is required to produce a WW map, which is (for complex problems, at least) required to obtain a tally response, the user might encounter a causality dilemma type of situation, struggling to get those first tally scores. In these cases, some geometry modification may be necessary—changing shielding density, for example. However, even after some tally response is achieved and the weight window map is generated, in general this first version is far from the most efficient possible one. WW generation thus becomes an iterative process, in which the user much repeatedly use a WW map to generate a better WW map.

The use of WWG is also, in some cases, prone to problematic behavior. In the *statistically pathological cases*, phase space may be insufficiently sampled, producing erroneous results [101]. Large scores may be created by very unlikely events and circumstances during the early particle histories. This pathology can then be transmitted to the WW generation. For example, if the user runs the simulation for a limited number of histories (to get the first response in the tally and define the first set of WW) and the tally scores do not include any particles coming from a rare but important path (e.g. particularly narrow streaming), the resulting WW map would prefer these establish paths and further neglect the rare paths, further decreasing the probability of those histories being sampled. The situation would then become worse with each iteration, leading to WW maps that suppress important streaming channels. To ameliorate such phenomena, MCNP features the ten statistical checks performed for each tally, providing the tools for the user to (better) understand the origin of the scores and the statistical behavior of the results. It's therefore imperative to study the results of these tests, most importantly the slope test and the variance of variance (VoV) test, especially in the early stages of the model design, when no previous results are available.

Another consequence of these pathologies is large weight gradients between adjacent (phase space) regions, which potentially lead to oversplitting problems and infinite particle histories. That is, a single particle history is split into an extremely large number of histories. One way to limit this behavior is to limit the number of secondary particles produced by each splitting event (or even per history). However, in the end, this problem can not be avoided completely. As such, it's crucial that the user inspects the used WW maps for any anomalies or steep gradients, and potentially (manually) corrects them.

3.3.3 ADVANTG

In an effort to address the limitations of WWG, specifically the need to get tally response in order to generate WW, and the iterative (and therefore time consuming) nature of the WW generation, ORNL has developed a hybrid variance reduction code *ADVANTG* (Automated Variance Reduction Generator) [92]. ADVANTG generates WW parameters based on a deterministic solution of the problem at hand.

Methods

In order to generate WW map optimized for a single tally response, ADVANTG uses the *CADIS* (Consistent Adjoint-Driven Importance Sampling) method [103].

Consider the time-independent neutron transport equation:

$$\begin{aligned}(\boldsymbol{\Omega}\cdot\nabla+\Sigma_t(\boldsymbol{r},E))\psi(\boldsymbol{r},E,\boldsymbol{\Omega}) \;=\; \\ \int_{4\pi} d\Omega' \int_0^\infty dE'\Sigma_s(\boldsymbol{r},E'\to E,\boldsymbol{\Omega}'\to\boldsymbol{\Omega})\psi(\boldsymbol{r},E',\boldsymbol{\Omega}') \;+\; s(\boldsymbol{r},E,\boldsymbol{\Omega}),\end{aligned} \tag{26}$$

where r is the position vector, Ω is the angular direction, E is energy, ψ is the neutron (angular) flux, Σ_t is the macroscopic total cross section, Σ_s is the double differential scattering cross section, and s is the source term.

The same equation can also be written using the transport operator $\boldsymbol{H}$:

$$\boldsymbol{H}\psi(\boldsymbol{r},E,\boldsymbol{\Omega}) \;=\; s. \tag{27}$$

In our case, since all operators and the functions on which they operate are always real [104], the quantity of interest is a detector response R, which can be defined as:

$$R=\langle\sigma_d,\psi\rangle, \tag{28}$$

where <> denotes integration over all the independent variables.

It is possible to define an operator $\boldsymbol{H}^\dagger$ that is adjoint to the transport operator $\boldsymbol{H}$, which will then operate on $\psi^\dagger$ (referred to as the *adjoint function*), such that

$$\langle\psi,\boldsymbol{H}^\dagger\psi^\dagger\rangle \;=\; \langle\psi^\dagger,\boldsymbol{H}\psi\rangle. \tag{29}$$

The relationship between them means that the detector response can also be defined as

$$R=\langle s,\psi^\dagger\rangle. \tag{30}$$

That is, the solution to the adjoint equation is orthogonal to the original (forward) transport equation and can be interpreted as the "importance" of neutrons within a particular system [104, 105].

This theory is utilized in the CADIS method to evaluate (space and energy dependent) WW boundaries, based on the adjoint solution. The weight targets are calculated as an inverse of the adjoint flux. That is, the higher the adjoint flux in the cell at position $\boldsymbol{P}$, the higher its importance (with regards to the tally contribution). Specifically,

$$w(\boldsymbol{P}) = \frac{R}{\psi^{\dagger}(\boldsymbol{P})}, \tag{31}$$

with lower weight boundaries defined as

$$w_l(\boldsymbol{P}) = \frac{2}{1+r}\frac{R}{\psi^{\dagger}(\boldsymbol{P})}, \tag{32}$$

where r is the ratio between upper and lower WW bounds.

However, this definition means that the detector response (R), which is to be evaluated by an VR-accelerated MCNP run, needs to be known for ADVANTG to determine the WW parameters. If an accurate solution was needed, this method would be useless. However, fortunately even coarse evaluations of the detector response can be used to produce effective VR parameters [92].

The methodology described up until this point optimizes the run for a single quantity of interest. In reality, most MCNP runs feature numerous quantities of interest, such as a single tally with multiple energy bins or multiple tallies. In this case, the *FW-CADIS* (Forward-weighted CADIS) method [106] is used.

In this method, first an adjoint source is constructed from all tallies of interest, weighted by the inverse of their individual responses. Specifically, the weights are defined as

$$s^{\dagger} = \frac{1}{R_1}\sigma_{d,1} + \frac{1}{R_2}\sigma_{d,2} + \cdots + \frac{1}{R_N}\sigma_{d,N}. \tag{33}$$

For this an additional Denovo calculation is required, to solve the forward flux and estimate the aforementioned responses.

When evaluating the relative weighting, for both energy and tally spatial volume, one can either evaluate the integrated response, or evaluate the detailed response. For example, for spatial weighting, the integral response option is *path-length weighting* and the detailed response is the *global weighting*.

The path-length weighting option maximized the overall (total) response of the tally. For the *i*-th cell the response R is defined as

$$R_i = \frac{1}{V_i}\int \sigma_i(E)\int_{V_i}\psi(\boldsymbol{r},E)\;dV\;dE, \tag{34}$$

where σ_i is the cross section associated with the response of the i-th tally.

Thus, the adjoint source used for the weighting is

$$s_i^{\dagger}(\boldsymbol{r},E) = \frac{f_i(\boldsymbol{r})\sigma_i(E)}{\int \sigma_i(E')\int_{V_i}\psi(\boldsymbol{r},E')\;dV\;dE'}, \tag{35}$$

where f is the indicator function, such that

$$f_i(\boldsymbol{r}) = \begin{cases} 1 & \text{for } \boldsymbol{r} \in V_i, \\ 0 & \text{otherwise.} \end{cases} \tag{36}$$

The other spatial weighting options seeks to produce a homogeneous response across the whole tally volume. That is, the number of contributions will be approximately constant across the whole tally volume, leading to a constant relative error.

Consider a tally of volume V, subdivided into N regions, each having volume $\Delta V = V/N$. Applying the path-length weighting to each of the N regions leads to the following adjoint source:

$$s^\dagger(\boldsymbol{r}, E) = \sum_{i=1}^{N} \frac{f_i(\boldsymbol{r})\sigma(E)}{\int \sigma(E') \int_{\Delta V} \psi(\boldsymbol{r}, E')\, dV\, dE'}. \tag{37}$$

In the CADIS method, the WW parameters are based on the ratio $\phi^\dagger/\langle\phi, q^\dagger\rangle$. As such, the adjoint source can be multiplied by a constant without any impact on the final results. Multiplying the denominator in the adjoint source definition by ΔV and assuming a large value of N leads to

$$s^\dagger(\boldsymbol{r}, E) = \frac{f(\boldsymbol{r})\sigma(E)}{\int \sigma(E')\psi(\boldsymbol{r}, E')\, dE'}, \tag{38}$$

where f is the indicator function for the tally volume.

The global weighting treatment can be applied to both cell tallies and mesh tallies of any size.

Application Procedure

ADVANTG utilizes the described CADIS and FW-CADIS methodology to define WW map for MCNP.

Firstly, ADVANTG must translate the MCNP combinatorial geometry into a structured Cartesian grid compatible with the three-dimensional discrete ordinates transport solver *Denovo* [37], which is used to solve adjoint (and forward, if necessary) flux. This is accomplished by a ray-tracing module of ADVANTG called *LAVA*, which defines the corresponding material mixtures for each mesh cell [92]. (Note that this is the same module, whose ray-tracing capability is used to define materials to be activated, as described in section 3.2.2.)

Once the Denovo problem is defined the solution is obtained (either of just the adjoint flux, or both adjoint and forward flux), calculating the WW parameters for each Denovo cell. These are then printed out into a WW map file, in identical format as used by WWG.

The CADIS method also defines an approach for biased source distribution sampling, preferentially sampling regions of high importance. However, due to the limitations of the version of ADVANTG used (3.0), specifically the limited support for cell rejection, the source definition employed at Nagra, is not compatible with the source biasing capability.

ADVANTG has been deployed at Nagra for the activation analysis problems since 2013 [73, 92, 107]. It was shown to produce WW maps significantly more efficient than those made with WWG [68, 83].

Oversplitting

The oversplitting issue described in the WWG section also applies to ADVANTG. This behavior slows down the overall calculation, particularly when running over multiple CPU threads. Due to the way (OpenMP) multi-threading is implemented in MCNP, new tasks are only assigned when all of the preceding tasks (given out to each CPU thread) are finished. As such, when oversplitting occurs on one thread, the other threads wait for the full history to finish, leading to very unbalanced CPU usage [87].

With ADVANTG-generated WW maps, oversplitting generally occurs due to problems with the Denovo solution. This can be discrepancy between the Denovo and MCNP geometry, or alternatively the inaccurate solution for the adjoint flux (for some energy grup flux).

The discrepancy between the Denovo mesh geometry and the MCNP combinatorial geometry can manifest by for example closed streaming paths, caused by a disagreement in the material density. This could be for example a narrow (millimeters-thick) air-filled ring gap surrounding a water-filled pipe passing through a long concrete shield, or alternatively a long air-filled pipe with small diameter passing though water. The structured Cartesian mesh (used by Denovo) is simply incapable of capturing the shape of the gap nor the pipe, and as such it is homogenized together with the surrounding material. This is illustrated (for the air-filled pipe example) in figure 20. In the top part of this figure, the air inside the pipe is homogenized together with the surrounding water, resulting in a cell with water of decreased density. The bottom part of this figure shows a bigger pipe. Here the central cell is correctly assigned as air (with no water). However, in the four neighboring cells the air is again homogenized with water, thereby decreasing the effective streaming path area. Ultimately, this closing of streaming paths leads to incorrect (sub-optimal) weights in the area.

An attempt to ameliorate this effect could be made by making the grid much finer in the vicinity of the pipe. However, since Denovo is fixed to use structured Cartesian mesh, one can only segment each axis once. As shown in figure 21, attempt to make a finer mesh in the center of the geometry results in a large number of extra highly-resolved cells (with very uneven aspect ratio), projected against each axis. This leads to a significant increase in the number of mesh cells (which in turn increases the RAM requirements). This is particularly the case when the pipe in question is

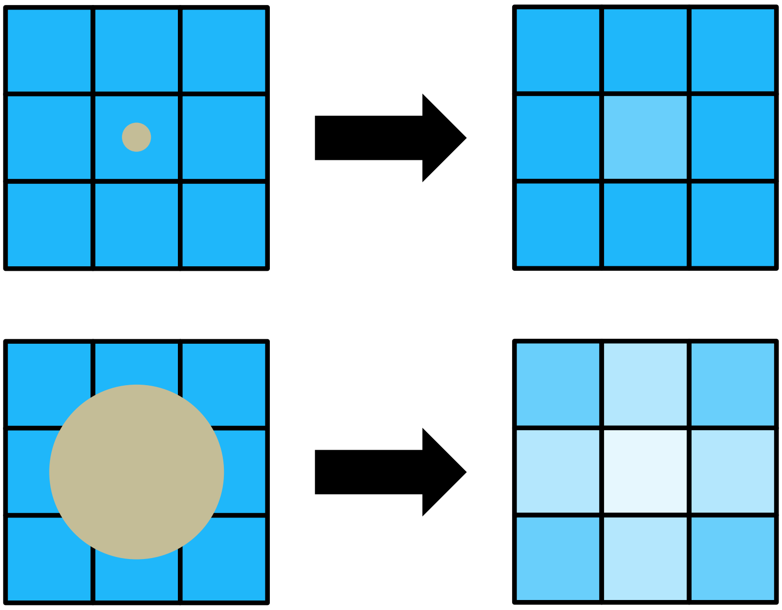

Figure 20: Material is homogenized in each Denovo cell. This may close or shrink streaming paths (compared to MCNP geometry).

not parallel to one of the three axes. Because of the structured mesh restriction, one would need to make the mesh finer for a much larger area—that is, for all X, Y, and Z values which at any point include the pipe cross section.

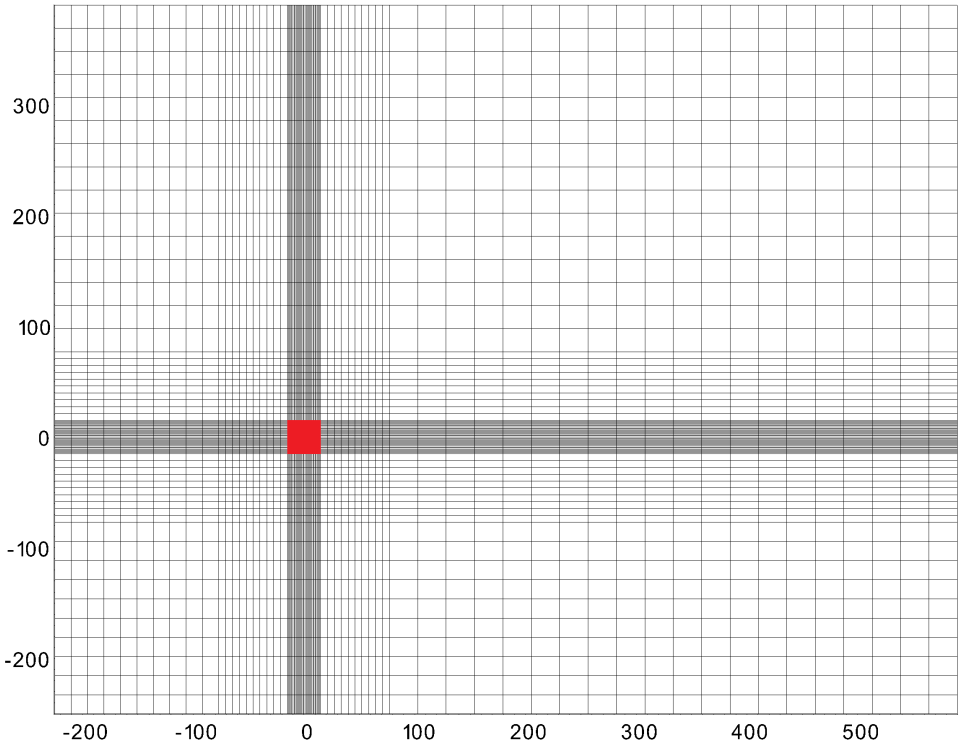

Figure 21: Structured mesh limitations. This mesh structure is necessary to create fine mesh for the central section (indicated in red).

Another potential technique, which was applied successfully in the past [108], involves the modification of the MCNP input provided to ADVANTG for geometry definition, such that the gap is made bigger. This increase in the gap size helps Denovo "see" the gap and assign better weights in this area. However, at the same time, the high importance is also assigned to the high-density (water or concrete filled) surroundings of the gap, because in the Denovo model this area was filled with air.

For example, when the Basel research reactor was simulated [108], it was necessary to capture the neutron streaming through a small but long air-filled pipe (diameter of 2.54 cm, length of 2.5 m) surrounded by water, since it was responsible for the vast majority of neutrons entering the room above the reactor. Applying the aforementioned methodology, the pipe diameter was increased for the Denovo calculation. Inevitably, high importance was also assigned to the water surrounding the pipe. This is illustrated in figure 22, where the tan-colored circle represents the real pipe diameter (in MCNP), and the nine cells around it represent the geometry seen by Denovo, with the central cell is composed entirely of air. In the MCNP model, only the tan-colored central circle area is occupied by air, with the rest filled with water. However, Denovo assigns high importance to the whole central section, thus leading to water-filled areas with high importance in the MCNP run.

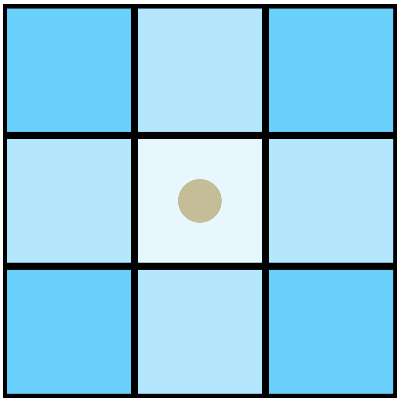

Figure 22: Air-filled pipe, as seen in MCNP (tan) and in Denovo (surrounding cells) geometries

Because of this, particles are considered important and split accordingly, even once they leave the pipe, decreasing the overall efficiency. As such, for optimal efficiency, a balance must be found between these two effects, finding the (problem-specific) *Goldilocks* radius. This is performed in an iterative trial-and-error fashion, with each case evaluated based on the computational efficiency of a given tally. In case of the Basel reactor, the optimal WW map performance was observed when the 2.54 cm pipe diameter was increased to to 8.54 cm.

In the end, these techniques provide the user with the tools necessary to influence the Denovo geometry and the resulting WW maps, which can be used when the discrepancy between Denovo and MCNP results in WW map that is inefficient (doesn't give sufficient importance to the important particles) or leads to oversplitting (maps with large weight gradients).

The second reason for oversplitting is the inaccurate solution for the adjoint flux in the lowest energy groups. This is generally caused by the mesh size being too big compared to the mean free path of neutrons at this energy—that is, of the lowest energy groups. If an accurate and complete deterministic solution (for all energy groups) is required, one would have to reduce the mesh size to avoid this issue. However, as described previously in this section, this increases the RAM requirements for the calculation. It may also lead to ray effects for fast energy group neutrons. Therefore, this inaccurate adjoint flux solution problem for thermal neutrons is generally solved by simply omitting several of the lowest energy groups from the Denovo calculation. That is, the number of energy groups Denovo uses is reduced. In the resulting WW map, the WW values assigned to the lowest used energy group are always automatically extended all the way to zero energy, thereby simply merging these lowest energy groups [92].

Defining a lower (than the default) limit of the maximum number of splits per event was (from user experience) found to have no effect on the frequency and severity of oversplitting. This is supported by experience described in [92].

Non-physical Flux Solutions

With the Denovo calculation being a deterministic one, it may potentially produce non-physical flux behaviors associated with deterministic transport codes, most importantly negative fluxes and ray effects.

Negative fluxes are caused by numerical phenomena. In this context, they are often caused by truncated anisotropic source expansions leading to negative scattering sources. To avoid negative sources, the Legendre scattering angle expansion order of at least 3 is used (i.e., P_3). However, they may also occur for positive sources, when the spatial discretization fails to yield a physical positive solution [38]. In the present methodology, spatial discretization is done using the step-characteristics discretization scheme, which when provided with positive sources is guaranteed to yield positive fluxes. It is also very tolerant of mesh cell aspect ratios and size, giving more flexibility to the user defining the mesh.

Ray effects are large non-physical spatial oscillations in the energy density [109] caused by the discrete ordinates angular approximation in which particles can only move along a discrete set of directions. Because of this, they sometimes do not reach regions which they otherwise would. This can be counteracted by refining the spatial meshing (making it coarser) or the angular meshing (making it finer, increasing RAM requirements).

In the end, it's crucial for the user to inspect the Denovo solutions and inspect them for any of the aforementioned non-physical phenomena, as well as large gradients in weight, and iteratively refine the VR parameter generation if necessary. Once running the MCNP simulation it is once again important to pay attention to the ten statistical checks for each tally of interest (just like for the WWG-generated WW maps, VoV and slope test being the most important). However, these tests have their limitations, and the use of elaborate VR parameters can challenge some of their underlying assumptions. Consider for the example the slope test, which estimates the number of score moments in the calculation. Specifically, it calculates the decline in the tally score with respect to decline in the number of histories. When calculating this, MCNP assumes [101] a Pareto fit for the tally scores probability density. However, in some cases (particularly with significant VR run augmentations) this fit doesn't match the real behavior and the slope test yields a value that is not representative of the tally. The user can overcome this by manually calculating the slope from the MCNP output (specifically *table 161*), thus checking if the test was actually passed. The manual determination of the slope is described in [110].

3.3.4 DXTRAN Spheres

DXTRAN is a deterministic transport method used to increase particle sampling in a volume of interest, defined by a sphere. The MCNP code then, at all source or interaction points, creates an additional particle, referred to as DXTRAN particle, which is deterministically scattered into the volume of a DXTRAN sphere (before undergoing any other interactions or escaping). The original (non-DXTRAN) particle undergoes its interaction and subsequent transport as normal, unless it enters a DXTRAN sphere, in which case it is killed. That is, the extra weight of the created DXTRAN particles is offset by the weight lost when non-DXTRAN particles are killed upon entering DXTRAN spheres.

The use of DXTRAN spheres is a challenging task since the implementation is problem-dependent and can introduce large weight fluctuations (for particle interactions just before and just after the DXTRAN sphere), particularly when the geometry inside the sphere is complex, or filled with material which leads to a lot of scattering. To counteract this, and maintain the efficiency and reliability of the calculation, one needs to deploy weight windows or nested DXTRAN spheres and avoid particles with excessive weights [72, 111].

This technique is particularly useful for problems in which there is a dominant direction (which the user would like to track). For example, this was the case for the modeling of the Basel research reactor, in which an air pipe, 2.5 cm in diameter, passed through 2.5 m of water, connecting the core with the room above. This was the source of virtually all the neutrons entering the room. In order to correctly determine the neutron flux in the room within a reasonable amount of computational time, DXTRAN spheres were employed to pull the particles in the desired direction, achieving significant improvements in computational efficiency [108].

However, most NPP models feature a large number of streaming paths, which all significantly contribute to the neutron transport to the areas of interest. As such, the potential to use DXTRAN spheres in these models is unfortunately low.

3.3.5 Techniques of Choice

The majority of VR techniques presented in this section are mutually exclusive: it wouldn't make sense to use cell splitting in combination with the built-in WWG nor ADVANTG, ADVANTG generates more efficient WW parameters than the WWG, and applying the WWG to the ADVANTG-generated WW map generally makes it less efficient. As such, and given that the ADVANTG-generated WW maps produce the most efficient VR parameters of these three techniques, the use of ADVANTG represents a clear choice for accelerating MCNP calculations.

The use of DXTRAN spheres requires significant amount of engineering time to implement, with its implementation being challenging and problem-specific. Nevertheless, the resulting speed up is often worth this time investment, particularly when coupled with an already efficient method like ADVANTG. However, in most NPP models, the number of important streaming paths is too great, and the application of DXTRAN is simply not an option. As such, for problems with predominant streaming (or transport, in general) directions of interest, DXTRAN spheres represent a powerful VR solution which can really speed up the calculation, but for the models in question, ADVANTG (used by itself) remains the top choice.

However, further improvements are always possible and ADVANTG is no exception.

Presently, the deterministic solver which ADVANTG relies on, Denovo, is limited to structured Cartesian mesh. As was described in this section, this sometimes leads to problems, with important streaming paths being closed and the geometry otherwise not being accurately represented. More flexibility with the mesh definition would therefore be very welcome. This could be simply more options with how the Cartesian mesh is defined, or even a completely unstructured mesh.

In cases where streaming occurs over a narrow but very long channel, the forced uniform discretization of angles is sub-optimal and RAM intensive. For such scenarios, the ability to define very fine angular discretization in the direction of the predominant streaming would allow generation of more efficient VR parameters.

Finally, with oversplitting frequently occurring for complex transport problems, additional tools to combat this pathology would be very useful.

These could, for example, provide finer user control over the creation of secondary particles (e.g. setting different limits for different regions) or the way these affect the CPU (through a more robust implementation of OpenMP). Admittedly, the solutions to these issues will likely have to focus on the MCNP itself, rather than just ADVANTG.

However, it bears repeating that while there are areas where improvements would be beneficial, ADVANTG already provides huge acceleration of the MCNP calculations, allowing the user to obtain well-converged solutions to most problem in the matter of days on single CPU workstations, even when large mesh tallies with detailed energy-group structure are involved.

3.4 VALIDATION

The usefulness of the activity predictions described in this section is constrained by the confidence in their results. As such, validation is of paramount importance. The validation process is split into two phases: neutron transport validation and activation validation.

3.4.1 Neutron Transport Validation

Methodology

Neutron transport is generally validated by in-situ sample activation campaigns [84, 112], in which small metal foils, stacked inside small cylindrical containers, are places at key locations (which typically lie on the neutron streaming paths or in representative locations in rooms) during a refueling outage and removed during the subsequent outage, thereby being activated during one whole cycle. The appearance of such a foil container, and a photograph demonstrating the placement (of another sample) are shown in figure 23.

(a) Container of foils

(b) Placement of a sample

Figure 23: Activation foils placed in KKB [87]

This motivated the selection of materials. Given the (in Switzerland) typical cycle length of one year, the chosen materials must have activation products with sufficiently long half-lives. Furthermore, in order to simplify the eventual analysis, the activation products must be easy to measure, preferably with gamma spectroscopy. Finally, the chosen foil materials must provide information about the energy distribution of the neutron flux. For this reason, cobalt, silver, and nickel were chosen. These foils predominately interact with neutrons at different (from each other) energies. Co-59, which undergoes an (n,γ) reaction, has an 836 b peak at 131 eV. When subjected to the neutron spectra representative of the space between the RPV and the bioshield, 70% of all Co-59 (n,γ) reactions took place at this peak energy (131 eV). Ag-109 undergoes an (n,γ) reaction with a 20500 b peak at 5.22 eV. When analyzed using the same energy spectrum as before, this peak was responsible for 60% of Ag-109 reactions [73]. Ni-58 undergoes an (n,p) reaction with a threshold of approximately 500 keV and majority of reactions occurring at even higher energies. As such, Ni-58 activation is representative of the fast neutron flux. Later on, additional foils made of Scandium were added to validation campaigns [87, 88]. In this case the relevant reaction is Sc-45 (n,γ) with a number of peaks in the keV range. The relevant cross sections are shown in figure 24.

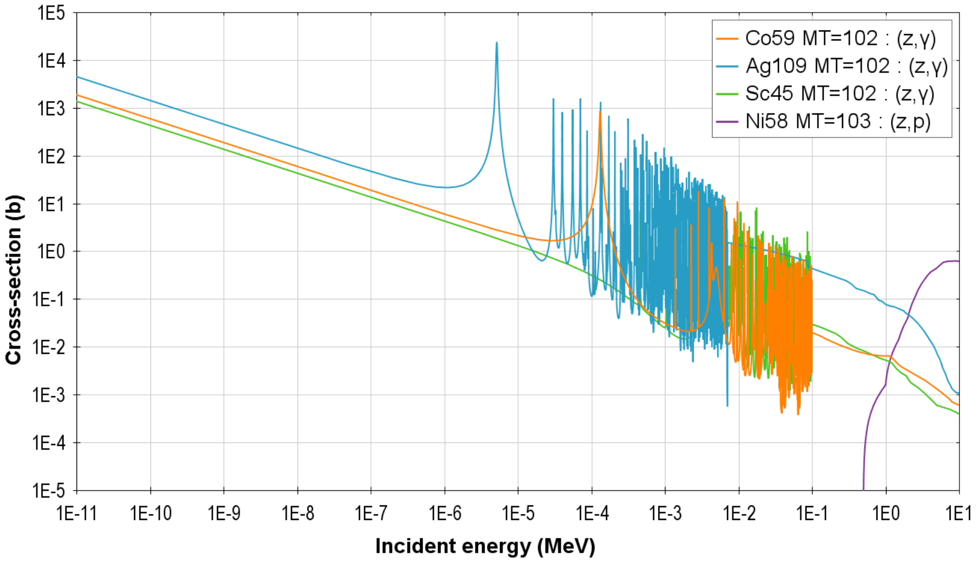

Figure 24: Cross sections relevant to validation foil activation

The foil thickness is determined based on the expected fluence, such that the resulting activation products deliver sufficient number of counts for a (gamma spectroscopy) measurement and at the same time not too high to require special radiological handling.

In order to compare the MCNP model with the foil measurements, the foil activation is calculated using the model. Specifically, the MCNP model is used to determine the reaction rates for the corresponding reactions, which are then combined with known cycle parameters (such as average power and cycle length) to determine the final activity of each corresponding foil.

However, given the very small size of each foil, obtaining good statistics requires a lot of computational time. Given the iterative nature of the validation process and the often large number of foil samples (e.g. 72 samples with up to three foils each are available for KKM alone [86]), it's desirable to speed up this calculation (beyond what is achieved with variance reduction, as described in section 3.3).

For this reason, the Generic Sample Activation Model (GSAM) was developed [113]. Instead of implementing very small cells representing the foils, a larger cell is created and the neutron flux distribution inside of it is captured. This is generally a sphere of five to seven centimeter diameter, centered at the known validation sample location. This neutron flux distribution is then used to define the source in a simple MCNP model representing the sample inside the aforementioned sphere.

The size of these cells is an important consideration. Larger cells allow faster result convergence, thereby reducing the computational time, while smaller cells more accurately capture the neutron flux observed by the sample (as they are less affected by volume averaging). Additionally, cell size may be restricted by the location itself. For example, a cell representing a sample in a thin channel cannot be thicker than the channel itself.

In the present methodology [113], when the flux is captured in the spherical cells, all directional information is lost and an assumed (homogeneous or directional) neutron direction is used. This may potentially change the results by changing the reaction rates of the simulated samples. While the impact is, for most cases, not expected to be major (given the targeted accuracy) [113], it ought to be kept in mind. It's advisable that the use of type-4 tallies with angular bins be explored in the future. However, this has not yet been tested.

The choice of the energy group structure to be captured by a tally and then output to GSAM is also very important. Tallies with a very large number of energy groups would decrease the error introduced by approximating the energy profile within each energy group, but at the same time require a very long time to converge, thereby defeating the sole purpose of GSAM. Furthermore, not all energy ranges are equally important for the reactions in question. To address this, a 25-group energy structure, referred to as *V25*, was developed [73], designed specifically to accurately capture the most important energy ranges while at the same time keeping the convergence reasonably fast.

In the end, the use of GSAM allows for a quicker calculation of foil activation. This comes at the cost of introducing additional uncertainty in the obtained result. This was quantified [113] to be in the order of 20% for a typical case.

Once both measured and MCNP-calculated foil activities (for the chosen activation products) are available, they can be compared.

Validation of KKM Flux

The original, rotationally-symmetric model of KKM was developed for the 2011 activation analysis [75]. Following the first flux validation attempts, large discrepancies were detected as close as the surroundings of the bioshield [73, 114]. Specifically, the flux was overestimated by as much as factor 6 in both the top and bottom of the inner side of the bioshield. The outer side, on the other hand, was significantly underestimated, leading to the calculated / measured foil activity (C/M) factors in the range of 0.2.

To address these discrepancies, the KKM model has been updated to implement a higher degree of detail inside the RPV [73], most importantly accurate core modeling capturing the exact variation of the void distribution in the core. This resolved the disagreement at the top of the inner side of the bioshield, with C/M factors newly in the range of 1.5 - 2.0 [73].

The underestimation on the outer side of the bioshield was identified to have been caused by the lack of bioshield openings in the model. In reality, the bioshield is penetrated in many locations with various water pipes, surrounded by air. Once these features were implemented, the C/M factors on the outside of the bioshield began to resemble the factors on the inside [86, 115].

The disagreement at the bottom of the bioshield has not been reconciled yet. It is believed to be caused by a combination of RPV internals (not being modeled in sufficient level of detail) and RPV insulation (believed to not have been present at the time of modeling, since confirmed to be present and filling part of the gap between the RPV and the bioshield) [73, 86].

The latest calculated C/M factors for the bioshield samples can be seen in table 6. The agreement is summarized graphically in figure 25.

Validation of KKB Flux

Even before the samples from the first KKB foil activation campaign were available (in summer 2018), the KKB model has been updated to add the level of detail foreseen to be necessary for good agreement (as well as the later detailed activation analysis), based on the lessons learned from other validation campaigns [68, 84, 85, 112]. The RPV internals were all modeled explicitly and in detail, the core power distribution was defined on the nodal level (like in KKM), and the surrounding concrete structures were accurately reproduced (to the best ability allowed by the available technical drawings) [87].

For the purposes of validation, 16 samples were selected as the primary focus, based on their location along the main neutron streaming paths leading to the adjacent rooms. These paths include the in-core instrumentation channel (3 samples), hot legs (5 sample), RPV upper head ring gap (4 samples), and the CR cluster assemblies (RCCA) area (4 samples).

Table 6: KKM flux validation results. Foil activity C/M values for the 14 selected validation samples on the inner and outer side of the bioshield.

Height (m)	Inner side			Outer side		
	^{60}Co	^{110m}Ag	^{58}Co	^{60}Co	^{110m}Ag	^{58}Co
17.8	2.0	1.5	1.4	1.9	N/A	2.0
16.8	2.3	1.8	1.3	1.3	N/A	1.0
15.8	1.5	1.1	1.2	1.2	N/A	1.3
14.8	1.7	1.5	1.6	1.2	N/A	1.6
13.8	1.7	0.9	0.8	1.2	1.2	1.3
13.0	1.6	0.8	0.7	1.2	1.2	1.2
12.0	1.5	1.0	0.9	1.8	1.5	1.6
11.0	1.9	1.3	1.3	1.7	1.6	2.0
10.0	2.5	1.9	3.7	2.5	1.9	3.7
9.0	3.0	2.0	3.7	3.0	2.0	3.7
8.0	4.1	4.7	3.0	4.1	N/A	3.0
7.0	3.6	3.4	2.6	3.6	N/A	2.6
6.0	4.1	3.4	3.1	4.1	N/A	3.1
5.1	4.9	4.1	5.7	4.9	N/A	5.7

The location and the calculated C/M factors for these samples can be seen in figure 26. In order to reduce the amount of information presented in the figure, the C/M factors of all foils within each given sample have been averaged into a single value. That is, only one value is reported per each sample. The exact C/M factors for all the foils can be found in table 7.

Table 7: KKB flux validation results. Foil activity C/M values for the 16 analyzed samples, grouped according to their location.

Sample	^{60}Co	^{110m}Ag	^{46}Sc	^{58}Co
R14	0.8	0.7	1.1	0.6
R15	1.0	0.9	1.5	0.4
R17	0.9	N/A	1.5	0.4
R19	1.0	N/A	1.4	0.6
R03	1.5	1.3	2.1	0.3
R04	1.5	1.2	2.0	0.7
R12	1.4	1.1	1.9	0.4
R13	1.3	0.9	1.9	0.4
R05	4.9	4.3	6.9	2.4
R07	4.8	4.8	7.0	2.9
R06	7.7	6.6	8.5	4.3
R08	5.2	4.8	7.6	3.0
R10	7.9	8.6	12.2	3.0
R11	1.8	1.8	2.0	1.8
R32	1.0	N/A	1.1	1.2
R33	0.9	N/A	1.1	0.7

From these results, it can be seen that the flux distribution in the immediate surroundings of the RPV (specifically the reactor cavity, the

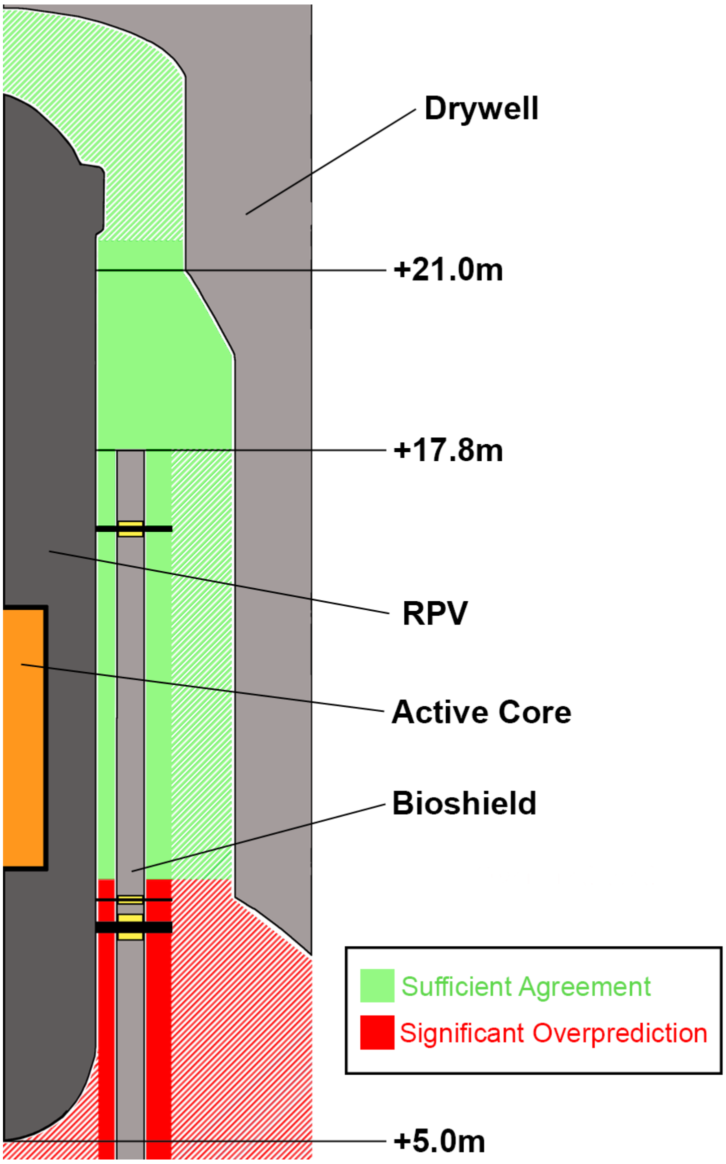

Figure 25: Graphical summary of the KKM validation results compared against the target agreement. Areas with solid green and red fill contain tested samples. The agreement in the areas with stripped fill is extrapolated based on the analyzed samples and knowledge of the streaming paths.

reactor pit, the RPV head, and the RCCA) are reproduced reliably.

This includes samples places along a very important streaming path passing through the ring gap between the RPV insulation and the bioshield. Neutrons passing this ring gap travel towards the reactor pit or alternatively the reactor cavity. In order to accurately capture this streaming, it was necessary to capture all the details of the RPV, its insulation and supports, as well as the bioshield and its liner, and all the cooling pipes and their flanges. This streaming path is reflected in the C/M values of the eight samples located above the RPV.

The (five) samples located at the ends of the hot leg penetrations (three on one hot leg, two on the other) show a significant overestimation of C/M

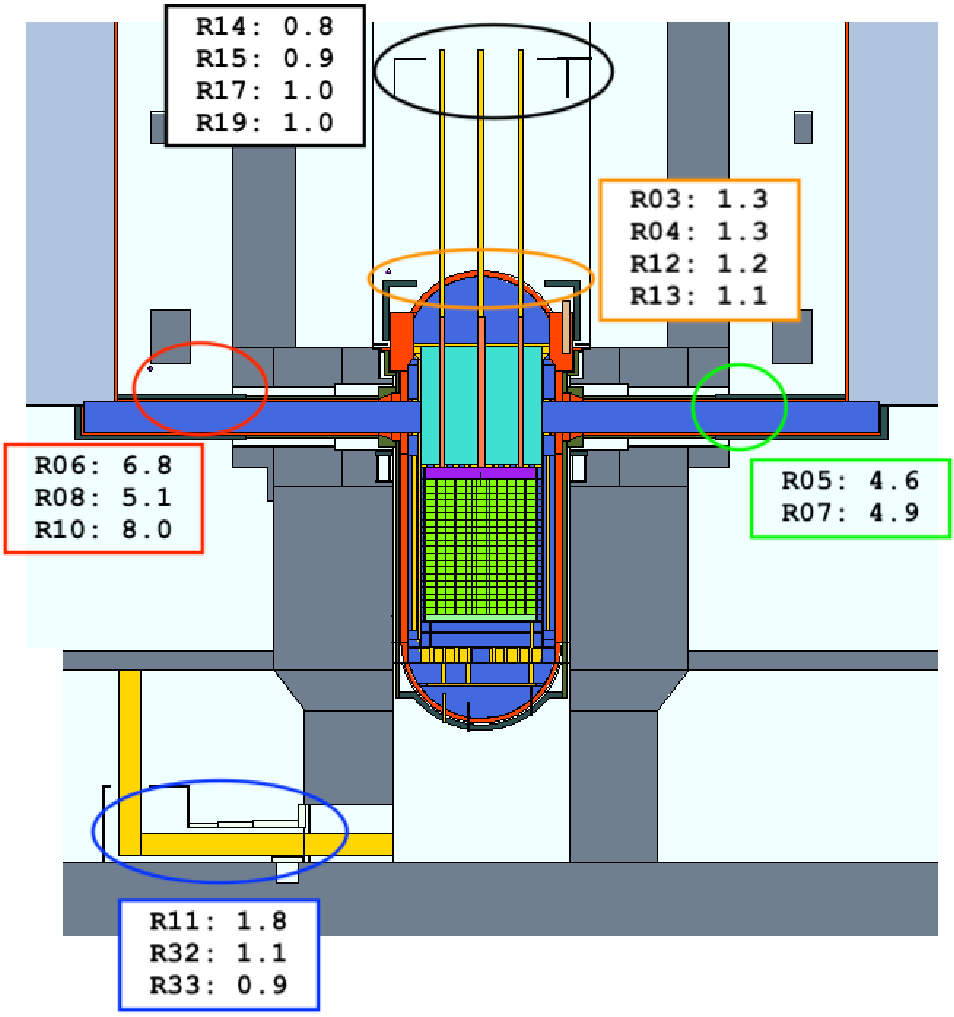

Figure 26: KKB validation results. Activity C/M values for the 16 analyzed samples, grouped according to their location. The C/M factors of all foils within each given sample have been averaged into a single value.

factor around 6. This area thus requires further analysis. It should be noted that these samples were found to be very sensitive to the modeling of the hot legs, including the insulation thickness and the exact geometry of the penetrations. Furthermore, given the good agreement in the reactor pit and cavity, the results strongly suggest that the disagreement stems solely from the hot leg penetrations themselves.

In order to ensure good agreement inside the instrumentation channel, represented by samples R11, R32, and R33, the guide tubes had to be modeled in at least coarsely to capture the associated streaming path at the bottom of the reactor cavity (circled in blue at the bottom left corner of figure 26).

General Approach Towards Validation Results Implementation

Once the flux validation results are calculated, they are compared against the target level of accuracy. This allows the user to gain insight into the model sensitivity to variations in chosen parameters and modeling approaches, thus building an understanding of the key streaming pathways for each plant. The calculated result is never scaled or otherwise adjusted based on the obtained C/M values. Instead, the deviation from the target level of accuracy is used to steer the updates of the MCNP NPP models. That is, areas in which the C/M factors are much larger than the target are re-visited and all supporting documentation for them is re-analyzed. Attempts are made to explain the larger-than-expected deviation through missing or additional streaming paths and the associated insufficient level of model detail, as well as through the presence of undocumented material (e.g. insulation) or differences in dimensions. All these would enable neutron transport towards or away from the area in question. As such, the possible explanations for the differences are tested against the existing technical drawings and discussed with the NPP staff familiar with the area in question.

The target accuracy is based on the expected impact of the activity overestimation on the subsequent applications of these results (see section 3.5)—that is, sensitivity. Most of the core internals are highly activated. As described in section 3.5.1, the *exact activity* determines the necessary shielding of the ILW casks into which these components will be placed. Therefore, significant overestimation of the activity will lead to overestimated shielding requirements, and therefore sub-optimal packing strategy and increased costs. On the other hand, e.g. concrete walls located far away from the reactor, such as the drywell in KKM, are only slightly activated. In this case the output of interest is the *total* volume of waste (material above clearance limits). However, given that the neutron flux inside concrete drops very quickly with depth, even a significant overestimation (e.g. C/M of 3) results in only marginal increase in activation depth and therefore total waste volume. As such, the decommissioning planning actions are less sensitive to the flux overestimation in this case.

Following this philosophy, the activation analysis methodology targets C/M between 1.0 and 1.5 outside the RPV (i.e., the closest *accessible* location (with respect to the core) where activation foils can be placed), between 1.5 and 2.0 further away from the core (such as the top of the bioshield or the reactor pit area below PWR RPVs), and between 2.0 and 3.0 for ever further away areas (such as the aforementioned KKM drywell or the pool area above PWR RPV head).

These target factors are also inherently linked to the systematic overestimation resulting from the empty room assumption. The further particles travel through these rooms, the higher the cumulative flux overestimation will be. For this reason, it's impossible to achieve a low C/M in these areas, without compensating for the (shielding-wise not-modeled) empty rooms.

This target agreement will also be applied to KKG and KKL models, as they are updated (in the future).

3.4.2 Activation Validation

The second phase of validation, evaluating the calculated activation inventories, is based on (mainly gamma, but also alpha and beta) spectroscopy of the actual activated materials. As such, it can only be performed to a very limited extent in operating plants before the final shutdown. That is, only if a removal of a sample from a material in question doesn't affect the reactor safety (e.g. small piece of bioshield concrete) or if the component is removed and replaced. The activation distribution of RPV internals described in section 3.2.2 cannot be fully validated before the final shutdown. Limited point-wise validation may be possible in case of internal component replacements.

Since none of the Swiss NPPs have been shut down yet, this validation step will mainly be performed on a full-scale plant after the final shutdown of KKM, currently scheduled for the end of 2019. However, the second phase of validation has been performed during the project to characterize the Basel research reactor.

Example Application: Basel Research Reactor

The light water pool-type AGN-211-P reactor was operated at the University of Basel from 1961 until 2013 for a total of 4,675 hours [108]. The maximum thermal power is 2 kW, corresponding to a centerline flux of 3.8e10 n cm^{-2} s^{-1}.

The reactor sits inside a 3.4-m-deep aluminum tank surrounded by concrete walls (made partially of baryte concrete) of 1 - 1.5 m thickness. The core is composed of 13 FAs, containing high-enriched (90%) metallic uranium plates. The FAs are surrounded by 29 graphite reflector elements. Both fuel and reflector assemblies end on the top with a lead element, providing additional upward-vertical shielding. The whole array rests on an aluminum support plate, fixed to a bridge structure (located above the pool) by four aluminum support columns. The core is covered by 2.5 m of water. The reactor has a narrow (25.4 mm in diameter) central experimentation channel, which represents the primary pathway for neutrons to stream from the core to the room above the tank. Figure 27 shows the whole reactor geometry, as represented by a University of Basel CAD model.

The reactor was shut down in 2013. The high-enriched uranium fuel has been removed and transported back to the USA in 2015. Afterwards, the decommissioning plan required the description of the nuclide vectors (i.e., the radiological inventory) associated with the activated components. To provide this information, the Nagra activation analysis methodology was applied to this research reactor. This represents the first ever application of the new ORIGEN-based automated methodology described in section 3.2.2.

As the first step, MCNP model of the Basel research reactor was used to calculate the nuclide vectors of all potentially-activated components [116].

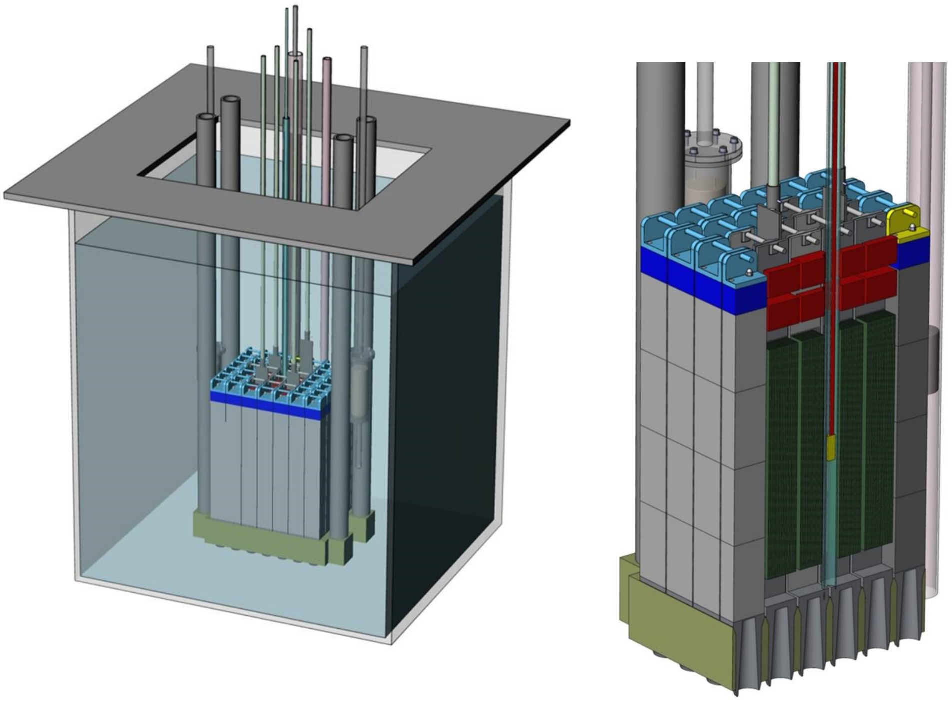

Figure 27: CAD model of the Basel research reactor, including a cut through the active zone [108]. (The CAD model is a property of the University of Basel.)

Afterwards, in order to validate these results, 15 samples were taken from the components in question [117] and analyzed with γ but also β spectroscopy [118]. Specifically, the samples were:

- **B1**: Graphite reflector
- **B2**: FA lead
- **B3**: Central streaming channel pipe (two samples, B3-1 and B3-2)
  - **B3-1**: core level
  - **B3-2**: above core
- **B4**: Core support plate
- **B5**: Aluminum tank floor
- **B6**: A drill core going below the tank floor, containing:
  - **B6-1**: Concrete (0 cm depth)
  - **B6-2**: Concrete (9 cm depth)
  - **B6-4**: Rebar (16 cm depth)
  - **B6-5**: Araldite
  - **B6-6**: Bitumen
- **B7**: Stainless-steel CR

- **B8**: Boral CR
- **B9**: Cadmium CR
- **B12**: Aluminum tank wall

Photographs of the selection of the samples are shown in figures 28–31.

Material composition (including impurities) was evaluated for a number of components (but not all). The aluminum alloys found in the research reactor showed a large variation in some of the impurity concentrations. For example, the highest measured Co concentration was 68.9 ppm, while the second highest concentration was 3.05 ppm, 22.3 times lower. This uncertainty in the exact concentration of important impurities proved to be the leading source of error for components, whose material composition was not directly analyzed.

The technical documentation of the Cadmium CR did not define its composition. Only the fact that it contains some amount of cadmium was known. Originally, it was assumed that the CR is composed of the AgInCd alloy, commonly used for PWR CRs. Consequently, large amounts of silver activation products (Ag-108m, Ag-110m) were predicted. However, these were not detected in the measurements, suggesting that the control rod is actually made of pure cadmium. The associated nuclide vector was therefore recalculated to reflect this fact, using cadmium with literature-based impurity vector as activation material.

Between the tank bottom and the concrete floor was a layer of Araldite (B6-5), followed by bitumen coating (B6-6). Given a variety of possible compositions and lack of detailed information, no nuclide vector was originally produced for these materials. The nuclide vector based on the measurements was created for the updated report. It should be noted that both Araldite and bitumen contained significant amounts of Ba-133. This indicates that a variety of Araldite containing barium was used (for example the one described in [119], which contains 30-60 % of barium sulphate). Given that Araldite was measured to have 100 times more Ba-133 than bitumen, the Ba-133 in bitumen is likely a result of contamination from Araldite (and potentially the concrete).

The tank wall was predicted to be well below the release limit. The γ spectroscopy of sample B12 showed Co-60 activity below the minimum detectable activity (MDA) of 0.02 Bq/g. No C/M factor was calculated.

For the purposes of validation, C/M factors were calculated for all measured nuclides in selected samples. The results are shown in table 8.

The uncertainty of the measurements is generally in the range of 10-30%.

Overall, the results are satisfactory, with C/M factors generally between 1.5 and 3.7 for components whose material composition was known. For

Figure 28: Sample B1: graphite reflector

Figure 29: Samples B3-1 and B3-2: central streaming channel pipe

Figure 30: Sample B4: core support plate

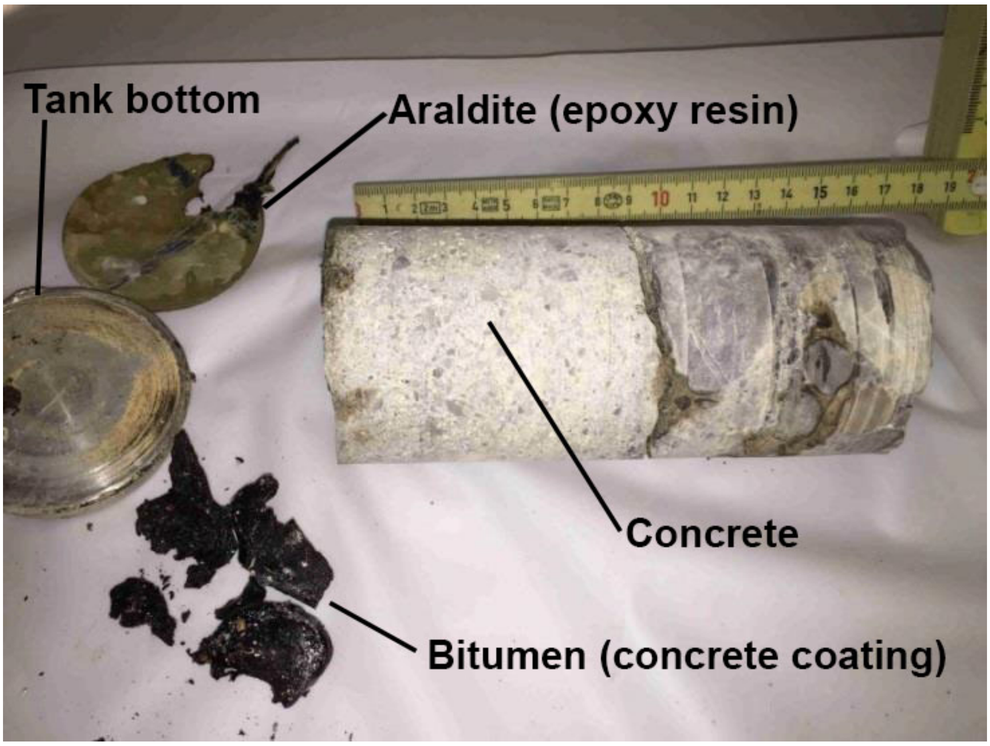

Figure 31: Drill core of the floor used for all B6 samples

Table 8: Basel reactor activation validation results

Sample	H-3	Mn-54	Fe-55	Co-60	Zn-65	Ba-133	Eu-152	Eu-154
B1	2.3							
B3-1		7.1		63	196			
B4			2.8	107	9.1			
B5				2.9	1.7			
B6-1	3.7	3.3		1.7		5.8	1.5	1.4
B6-2	2.3	2.3		2.1		6.4	1.8	2.0
B6-4		2.0	3.6	3.3				
B7				1.9				

cases where the composition was approximated using similar components or even literature values, the C/M factors are much larger. For example, the cobalt impurity in the central streaming channel and the core support grid aluminum were clearly overestimated, leading to a significant overestimation.

These cases highlight some of the major reasons why this validation step is required. No foil-activation flux validation has been carried out for Basel, making the activation validation the only validation step. However, even in cases where the flux validation was successfully carried out, activation validation is needed to provide additional information about the material composition. It provides information that can be used to infer whether the correct overall material composition was used (as demonstrated by the cadmium CR here), whether the correct impurity levels were used (as demonstrated by the highly overestimated Co-60 in the central streaming channel or the core support plate), or whether all the impurities were accounted for (as demonstrated by unexpected impurities being discovered in the graphite). Additionally, this validation step provides information about neglected mechanisms, such as diffusion—consider, for example, H-3 in concrete (hydrogen is very mobile).

In the end, all these validation results were used to adjust the predicted nuclide vectors [120]. That is, the always-conservative results are converted into best-estimate results. Note that while the measured values were used to scale the calculated activity of the measured nuclides, no attempt was made to infer the activity of the other calculated nuclides, which were not measured. In the future, in cases where one is certain about the material composition (e.g. if material analysis was carried out on this component) and therefore that the discrepancy comes entirely from the overestimation of the neutron flux, a case could be made to also scale nuclides, which were not directly measured. In the future, this type of activity scaling is expected to be applied for the NPP activity calculations once (enough) measurements are available.

Furthermore, nuclides, which were not originally expected to be present, were added. In cases where the measured activity fell below the MDA, the

MDA values were conservatively used.

The decommissioning concept for the Basel research reactor, including the description of the nuclide vectors of the activated components, has been accepted by ENSI in May 2018. The dismantling of the reactor is expected to be completed in 2020 [121].

Need for Measurements

This validation step of the Nagra Activation Analysis Methodology is generally comparable to an activation characterization based solely (or primarily) on measurements. Consider for example a research reactor decommissioning project, such as the one described in [122]. In this case, the aim was merely the quantification of the total amount of activated (and contaminated) material based on total activity values, rather than the determination of the full associated nuclide vector. To achieve this limited goal, *149 measurements* were carried out over the course of three weeks. The extent of activation was then approximated from these measurements [123].

In comparison, during the decommissioning project of the Basel research reactor, the Nagra Activation Analysis Methodology was employed to characterize the component activation (providing the full nuclide vector). The company in charge of the decommissioning still had to perform measurements. The main difference is that these measurements were for validation only. Therefore, the total number of measurements could be greatly reduced, since an order significantly fewer measurements are needed to validate the calculated activation distribution than to reconstruct the total activation profile for each component. In case of Basel, only *15 samples* were measured in total—an order of magnitude fewer measurements than in the previous example. Furthermore, many of these were collected at the same time—for example, a single drill core was used to create all six B6 samples (two layers of epoxy glue, three concrete samples and one rebar steel sample).

Activity measurements are still necessary, regardless of the characterization technique employed. However, when measurements are made solely for validation, a (relatively) small number of point-wise measurements is generally sufficient.

3.4.3 Validation Summary

Much like the NPPs they represent, the MCNP NPP models created under the Nagra Activation Analysis Methodology are complex. There are many areas which can significantly affect the final result: accurate representation of large components and other shielding, inclusion of all important streaming paths, or detailed core representation. Before the activation results can be used to make decisions, it's necessary to establish confidence in the models and their ability to accurately simulate the neutron transport in the respective NPPs.

Flux is validated using foil activation. That is, foils left to be activated inside the NPP for one cycle, afterwards compared against the MCNP-simulated foil activation. This method provides a good overview of the accuracy of the calculated flux throughout the model geometry, as well as an input for debugging and general improvements of the model. Foil activation campaigns have been carried out at KKM, KKG, and KKB, with the KKL campaign currently ongoing.

The calculated activation is validated by direct measurements of the actual activated materials. This method provides a cumulative feedback on the accuracy of the flux calculations as well as the material definition, since the calculated activities (which are compared to the measurements) are affected by both flux and the impurity (or base material) concentration in the given component. Once sufficient number of measurements are available, the calculated activity can be scaled to match more closely to the reality. However, this method generally cannot be applied for a still-operating NPP, since one is (for safety reasons) not allowed to remove parts of (most of) the activated components.

Together, these two techniques provide valuable feedback to the model designer, as well as (following an agreeable comparison) confidence to all users of the produced results.

3.5 RESULTS APPLICATION

Once the activation calculations are completed and the distributions of activation products in all analyzed NPP components are known, the results can be used for a variety of applications. Directly, this information can be used to decide on an optimum segmentation strategy and, afterwards, a corresponding packaging concept. These results could then be used to answer questions relating to total activated waste volume and its change over time, for example to investigate the effects of decay storage. Moreover, the activation results can also be used to define gamma source terms and analyze dose rate fields associated with the components in question, serving as a valuable input for decommissioning planning. All these applications are described in more detail in the remainder of this section.

3.5.1 Segmentation and Packaging Planning

Given the large variation in the activity, activated components may be classified as low-level or as intermediate-level waste. In many cases, the variation of activity within the component means that parts of it are LLW and parts ILW. In these cases, accurate knowledge of the activity distribution is integral to defining efficient segmentation.

In Switzerland, LLW components (or component parts) which pose only a limited radiological risk are packed into a concrete LLW container. Concrete components are packaged into an LC-86 container (pictured in figure 32) and steel components are packaged into an LC-84 container (which is identical to LC-86 except for one of its sides being shorter, resulting in lower overall volume). ILW components (or component parts) are packaged into MOSAIK casks, manufactured by GNS [124], shown in figure 33. Compared to LC-84/6, the MOSAIK cask offers significantly more shielding, which can be increased even further by adding (up to 120 mm of) optional lead shielding around the inner waste basket. This additional shielding comes at the expense of reduced inner volume and increased cost. The LC-84 container offers approximately an order of magnitude more inner volume, while costing an order of magnitude less than a MOSAIK cask.

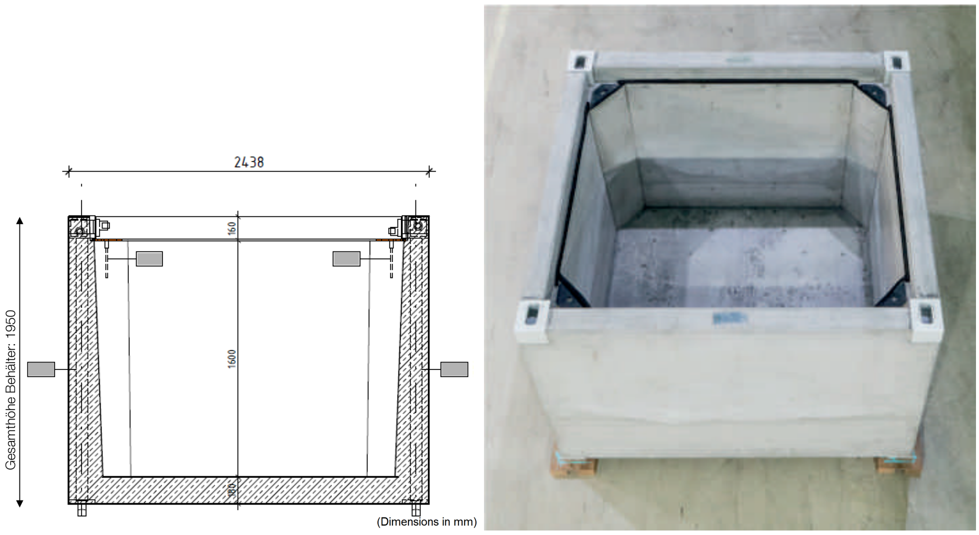

(a) Technical drawing

(b) Photo

Figure 32: LC-86 container (LLW). (Technical drawing from [125], photo provided by Nagra.)

For this reason it's very desirable to efficiently segment and package each component, so that as much of them as possible can be placed into an LLW container, or an ILW container with the thinnest possible inner shielding—that is, to minimize the total cost of containers.

This is directly addressed by the methodology described in section 3.2. Specifically, the activity distribution of the analyzed components coupled with the ALGOPACK solver (described in section 3.2.3) help find the most efficient way to pack the given activated waste.

However, the final segmentation approach will be limited by constraints imposed by the NPP operator. This includes the available cutting techniques and various limitations resulting from space limitations. For this reason it's highly desirable to integrate the activation characterization results into the existing CAD models used by the NPP, where it could be directly accessed

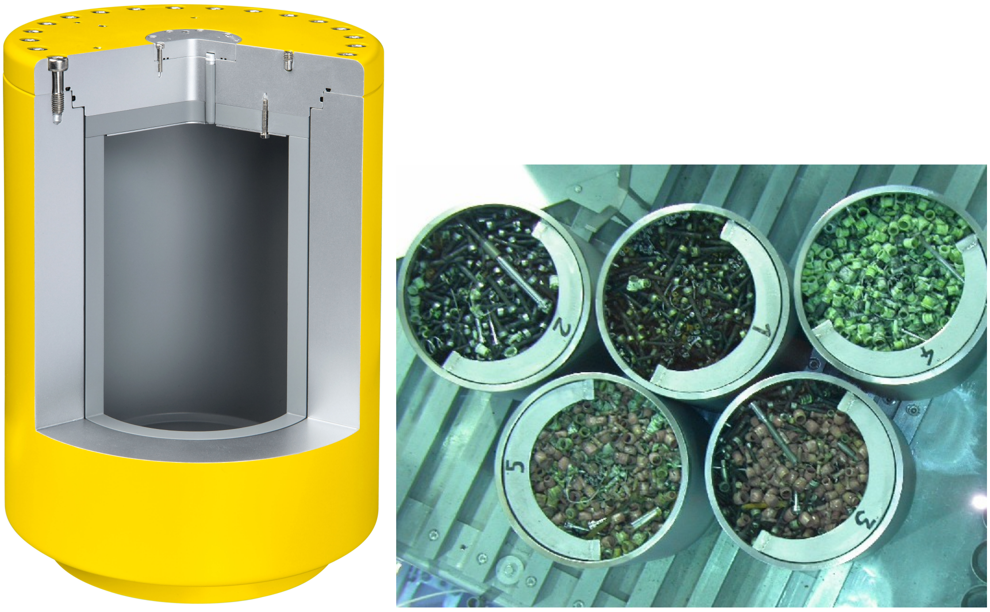

(a) 3D model (b) Inner basket

Figure 33: MOSAIK cask (ILW). (Photo from [100], 3D model ©GNS Gesellschaft für Nuklear-Service mbH.)

by the person planning segmentation. Efforts to set up such an integration are currently ongoing with KKM and KKB. Specifically, the post-processing module of the activation code was modified to output the data in a *PTX* file format [126] instead of the CSV. This is a plain-text picture format, where each pixel has three-dimensional spatial coordinates (in terms of x, y, and z) as well as color definition (in terms of RGB coordinates plus intensity). This file can then be imported into a Building Information Modeling software such as Autodesk Revit®, where it can be superimposed over the component and visualize the activation distribution.

3.5.2 Decay Storage Analysis

The calculated activation distribution, for any given decay time, can be used to evaluate the total volume of concrete above release limit. For example, figure 34 shows a comparison of KKM activated concrete after 5 years and after 35 years of decay. Beige color represents regions which are below the clearance levels (i.e., where the sum rule value is below one). Yellow-colored regions do not qualify for free release, but may qualify for limited release. In this example, limited release of concrete was assumed to be limited by sum rule value of 10. (That is, the yellow color represents areas where the sum rule value is between 1 and 10.) Finally, the red-colored region (doesn't qualify for limited release and) must be treated as radioactive waste.

Upon closer examination of figure 34, one can see artifacts on the edges of the spherical drywell bulb. These are caused by a combination of two factors: plotting threshold criteria and statistical uncertainty. The VisIt

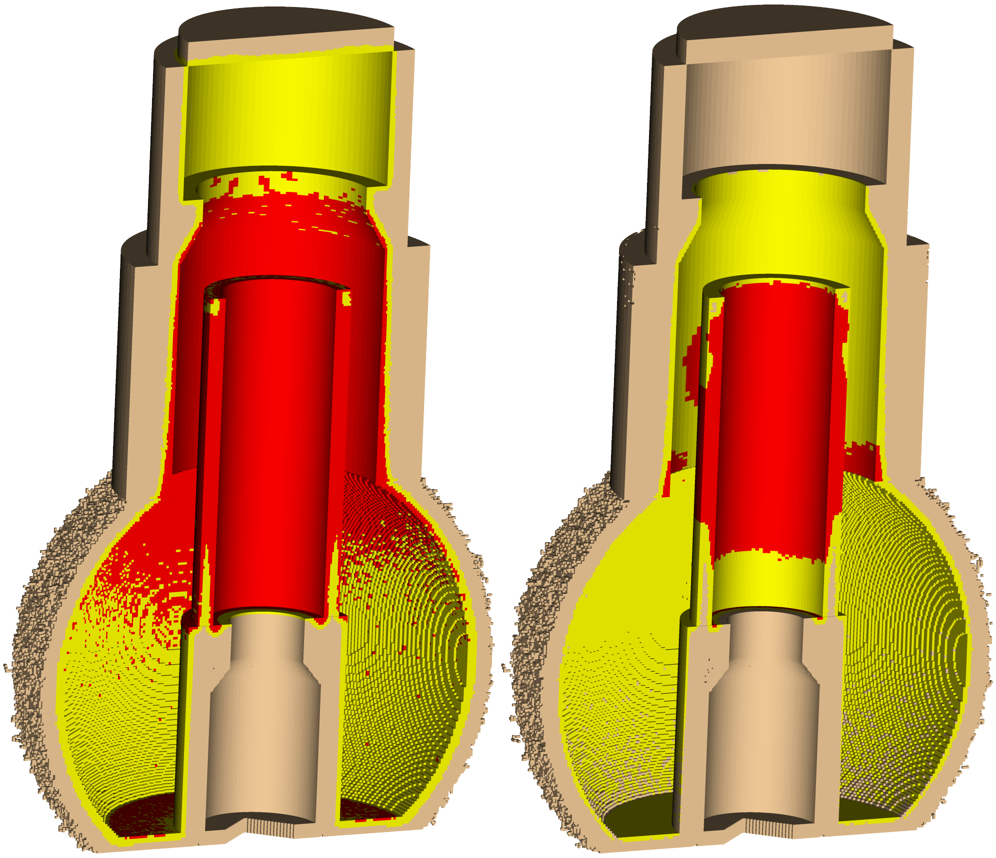

(a) 5 years decay (b) 35 years decay

Figure 34: KKM activated concrete volume. Beige: unlimited release, yellow: limited release, red: radioactive waste.

software used to visualize these results was set to only show cells with (total) activities above 10^{-10} Bq. This is the way air in between components is excluded. At this concrete depth, the activity falls below this threshold and the cells are no longer plotted. The exact depth varies, because the calculated flux has not fully converged, and the statistical uncertainties are still comparatively high. In the end, this variation in depth, coupled with the activity threshold for cell visibility, results in artifacts which create an uneven outer bulb surface.

The graphical representation is naturally also supported by the corresponding detailed numerical description using CSV files. Such comparisons can be used to evaluate the effects of decay storage or deferred dismantling.

3.5.3 Dose Rate Calculations

Most activated components contain activation products, which emit high-energy gammas, which then pose a significant risk to personnel working around these components. This is particularly the case during decommissioning, when the water from the RPV is drained, removing its shielding effect, and some of the internals removed from the RPV and placed on the working floor, where numerous workers are expected to be found. For this reason it's desirable to calculate the dose rate fields associated with the given components and therefore predict the radiological risk for the personnel and as an input for the planning of the necessary shielding layout for each decommissioning work stage.

Presently this is done manually by translating the activation analysis result into an MCNP source definition. As such, currently the capability to calculate cumulative dose rate fields is limited, and the effort is work-intensive. However, a project is ongoing to bring back original features of the used activation code (described in section 3.2.2) and use activation calculations to define the MCNP gamma source automatically.

3.6 FUTURE OUTLOOK

As a whole, the Nagra 2018 Activation Analysis Methodology offers a rich repertoire of tools to simulate the neutron transport, quantify the activation of all NPP materials, and answer a number of the associated questions.

The detailed three-dimensional MCNP models of NPPs capture all of the important neutron transport. The calculated neutron distribution is then validated with foil-activation based flux-measurement campaigns, quantifying the model's accuracy in predicting neutron flux and spectrum. The highly automatized, ORIGEN-based activation code sequence then uses these results to calculate the overall material activation, outputting results as detailed data sets as well as easy-to-understand three-dimensional component figures. Finally, the calculated activities will then also be validated against spectroscopy measurements of the actual activated materials.

The activation results are then used to answer associated questions. An optimization script, called ALGOPACK, has been developed to assist with component segmentation and packaging, aiming to optimize the number and type of waste canisters used to package each component. The activation results can also be used to quantify the total volume of waste (material above clearance limits) following decay of various durations, thus assisting with the decay storage planning. Finally, the activation results can be used to calculate gamma dose rates associated with the activation products, thus assisting with decommissioning planning (for picking the correct shielding and minimizing the overall dose to the workers).

The methodology is constantly developing, with improvements of existing tools and additional validation campaigns planned for the future.

While the currently employed VR tools offer a significant acceleration of the MCNP calculations, the complexity of the developed models continues to push the available computational resources to their limits. In order to fully benefit from the MCNP simulations potential, the VR techniques will still have to be improved (in some of the ways described in section 3.3.5).

Alternatively, the computational power available will have to be increased.

The current activation code sequence is still in development, with a number of updates planned for the future. Particularly notable is the automation of the gamma source definition, based on the calculated activation distribution and inventory, which will allow detailed gamma transport and dose rate calculation.

The focus of the present methodology is purely on activation. However, for completeness reasons, it is also desirable to include the expected contamination. While contamination is responsible for two orders of magnitude less activity than activation, its contribution is still significant, particularly for low-activated components (especially inside the RPV, such as the BWR steam dryers). If contamination is included in the final results, they will be complete and could directly be used for the packaging planning and documentation requirements without the need for any additional steps in between.

The second stage of validation (activation measurements) cannot be carried out to the desired extent for operating NPPs. As such, the first large-scale validation of the Nagra NPP model will only occur following the shutdown of KKM in 2019. This validation campaign is expected to provide a crucial insight into the accuracy of the carried out activation calculations.

The NPP operators are still deciding on the exact segmentation approaches they will employ during decommissioning. As the respective boundary conditions are clarified and more is known about the plant dismantling in general, the supporting tool-set can be extended to best assist the NPP segmentation needs. This will involve further updates for ALGOPACK, as well as development of new tools, should the need arise—for example, CAD visualization of the activation results for segmentation planning.

These future additions will continue improving the Nagra Activation Methodology and building on its utility. However, already now the high-fidelity results delivered cover the full nuclide vectors of activated components. Thanks to the validation, their accuracy is generally known. As such, these results provide an invaluable basis for informed decision making and an overall realistic and detailed decommissioning planning.

4 REACTOR WASTE

Reactor waste is mostly composed of components, which are located inside the RPV during operation. As such, they are subjected to high flux and therefore are expected to be strongly activated (much like reactor internals described in chapter 3). This category includes, among many others, control rods (CR), which are inserted and removed during operation to steer the power level, and LPRM (Local Power Range Monitor) detectors, which are moved around the core as part of neutron flux measurements. Unlike the activated components described in chapter 3, the position of these two components within the RPV is not fixed during operation.

For most of these components, there are no records detailing their exact positions within the core and the corresponding time duration. For this reason, the methodology described in chapter 3 cannot be directly applied. The necessary extension of this methodology is proposed in this chapter, based on dose rate measurements obtained after the component is no longer in use (and is stored in spent fuel pool), as well as the nuclide vector determination using the activation analysis methodology from chapter 3.

The aforementioned lack of information does not necessarily apply to CR, where movement records are kept. CR movements are an integral part of burnup calculations, since their presence has a strong effect on the neutron spectrum in their vicinity. For this reason, information about CR movement is collected as part of core studies. This information could then be used, together with detailed information about the core, to reconstruct the neutron flux individual CRs have been subjected to, and thus to calculate their activation. This approach has been employed for example at PSI [127, 128]. However, such a procedure is very work intensive, which given the associated uncertainties inherited from the uncertainties associated with the individual cycles and rod movement, as well as the major uncertainty of CR material impurities, makes this calculation approach only justified for some applications. Furthermore, it's useful to compare the results calculated with such a method against other (more pragmatic) calculation approaches based mainly on post-operational dose rate measurements. This method then has the additional benefit of also being applicable to other types of RA (i.e., not just CR). This way, the same systematic methodology, based on generalized dose rate measurements, and the developments described in chapter 3, is consistently used to characterize all RA. For all these reasons, the methodology described in this chapter is valuable and applicable, and has already been applied to the characterization of RA from KKM.

The general approach of the new methodology is described in section 4.1. The approach to assess the associated nuclide vector is then defined in section 4.2. When multiple dose rate measurements are available for a single component, this methodology can be further extended to give insight into the radionuclide distribution. This is described in section 4.3. The numerical instabilities sometimes observed within the associated calculations, and the techniques employed to treat them, are discussed in section 4.4. Finally, the methodology and its contribution towards a systematic RA characterization approach are summarized in section 4.5.

4.1 TOTAL ACTIVITY ESTIMATION

Dose rate measurements can be used to obtain information about the activity of the radionuclides contained within a given component. The measurements provided for this purpose vary in the degree of detail, from single measurements of a basket containing multiple pieces of the investigated component, to a number of axial measurements along each component.

The geometrical descriptions of the components are also of variable level of detail. Generally, technical drawings and exact mass descriptions are available. However, for some components, this the information is limited to a photo of the component in the spent fuel pool and an approximation of the mass and total quantity.

Naturally, the lower the quality of the component information, the higher the uncertainty about the calculated result, which will in turn require a higher degree of conservatism. The results will vary from rough approximations of total activity to a detailed distribution profile.

In order to be able to apply the here-described methodology, one must know the key nuclides for the gamma emission present in the investigated component. This could be based on prior experience (e.g., identification of Co-60 as key nuclide in cobalt-rich materials such as stellite), or it could be reconstructed using the activation analysis methodology—this is described in section 4.2.

Once the nuclides in question are know, one can calculate the total activity from the dose rate measurement. This is done by first creating a simple shielding model of the component in question and the corresponding detector (made in MCNP or MicroShield, a gamma ray shielding and dose assessment code [129]). This is illustrated in figure 35. The activity is set to 1 Bq and the dose rate is calculated.

Understanding that the ratio of the measured dose rate and the dose rate calculated for unit activity is equal to the real activity (in Bq), the total activity is calculated. For example, using the setup shown in figure 35, if gamma dose rate of 10 mSv/h is measured, the component activity would be equal to $\frac{1e{-}2}{1.62e{-}11} = 6.25e8$ Bq.

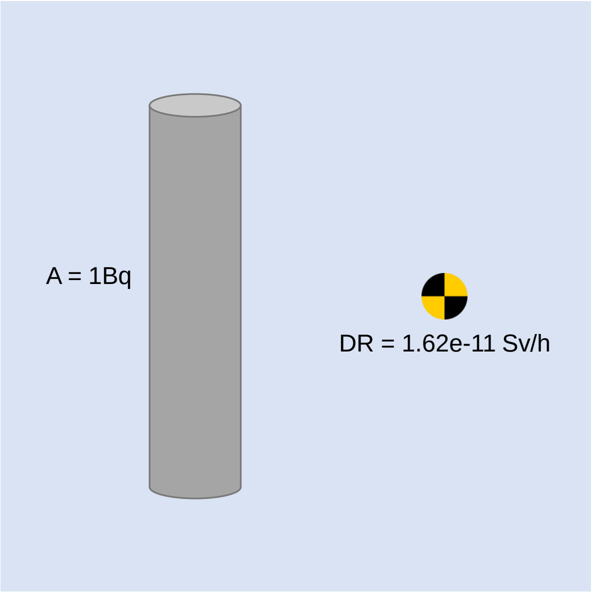

Figure 35: Illustration of the Microshield model used to relate activity to dose rate

It should be noted that this approach calculates the total activity (in Bq) rather than the specific activity (in Bq/g), which could be calculated using the knowledge of component mass, if available.

4.2 NUCLIDE VECTOR DETERMINATION

In cases where the (relative) nuclide vector of the component is not known, it's necessary to determine a likely one, before the total component activity can be determined. This is done by creating an MCNP model of the component in question (to the best ability, as limited by the available information) and activating it with a neutron spectrum representative of the component location within the RPV. This is done using a detailed model of the whole RPV, as developed for decommissioning waste characterization (as described in chapter 3). The neutron spectrum is obtained using a multi-group tally.

For most reactor waste components, the exact position in the RPV varies, therefore the flux shape too will vary. One could either use the most representative location (where the component likely spent most of the time) or capture a series of flux shapes at a number of likely locations, and proceed with the rest of the process for each of them, thus obtaining the expected range of each nuclide activity.

Once the neutron spectrum is obtained, it can be provided for the the activation calculation, performed according to the activation methodology described in section 3.2.

If the irradiation history is known, it can be directly used during the activation step. In other cases, the user must approximate which fraction of the NPP life (already input for the activation of decommissioning waste components) is relevant for the component in question.

The material definition, including impurities, is of paramount importance, as it will decide the exact nuclides present in the activated component.

Since the nuclide vector will later be scaled, only the nuclide activities with respect to each other are of interest—that is, the flux shape rather than magnitude are the focus.

The resulting nuclide vector features nuclides which are realistically expected to be found in the activated component. This vector can then be scaled to match the measured dose rate, following the approach described in section 4.1.

4.3 ACTIVITY DISTRIBUTION RECONSTRUCTION

So far the described approach assumed a single dose rate measurement per component. However, for many components, multiple dose rate measurements are available, allowing the reconstruction of the activity distribution, which is useful for for example segmentation planning.

In these cases, the dose rate measurements are often carried out close enough to each other for the same component segment to affect multiple dose rate measurements at once.

To illustrate the methodology applied to calculate the activity distribution using multiple dose rate measurements, consider the characterization of control rods.

Firstly, an MCNP model of the exact control rod design is created, exactly reproducing the shape and dimensions of the rod, as well as its inner structure. Figure 36 shows an example of such a model. The models are based on detailed technical drawings. See [130] for a (publicly available) illustration of the typical CR designs.

This MCNP model is then split into a number of axial zones, each assumed to have a homogeneously distributed activity throughout it. As an illustration, consider a hypothetical control rod, split axially into four segments, each with its own activity (A1-A4). In front of each segment, there is a known dose rate measurement (D1-D4). This is shown in figure 37.

The height of each rod segment doesn't necessarily have to correspond to the position of the dose rate measurement – only their total number has to match (here: four segments, four dose rate measurements).

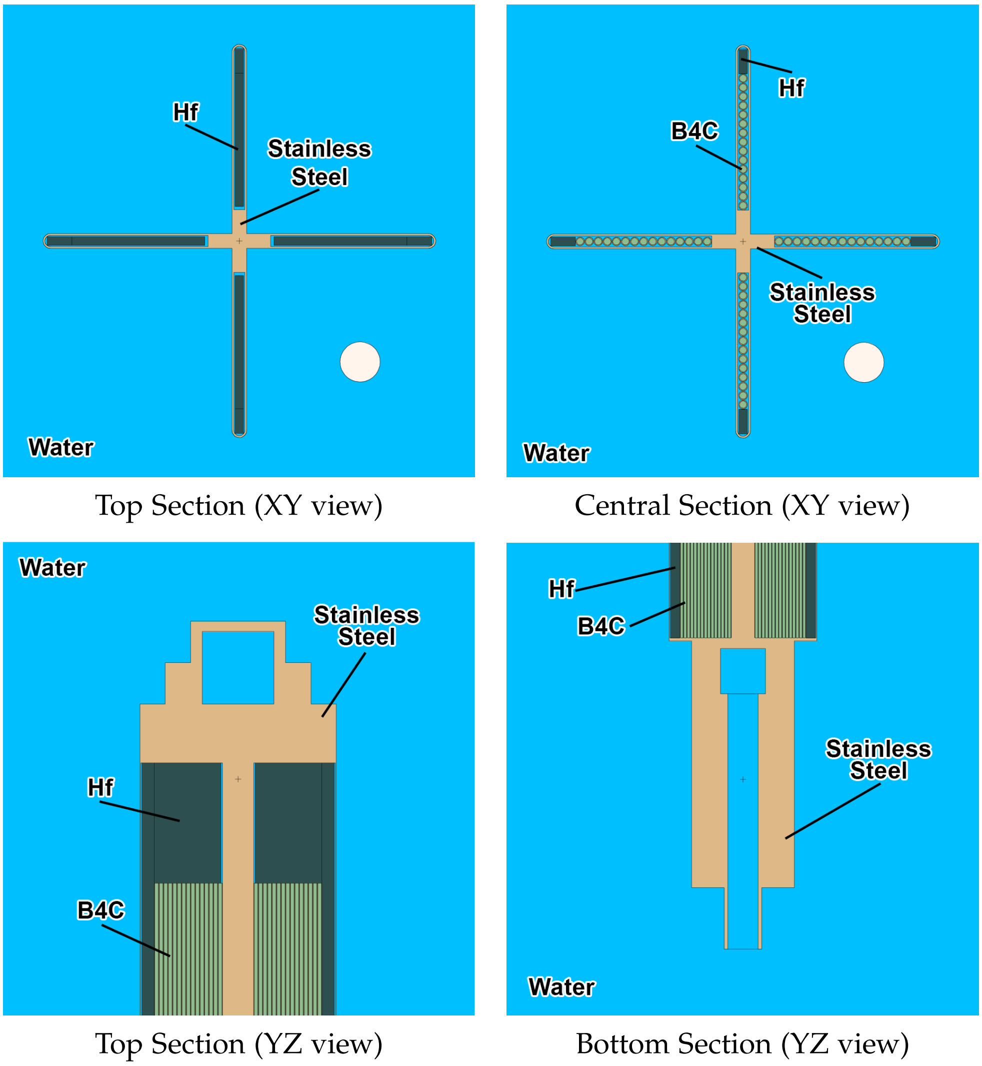

Top Section (XY view)

Central Section (XY view)

Top Section (YZ view)

Bottom Section (YZ view)

Figure 36: MCNP model of a control rod

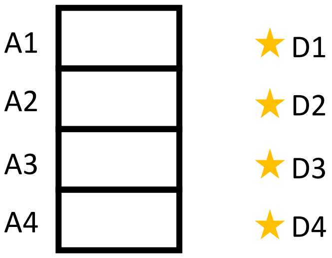

Figure 37: Axial zoning of a hypothetical control rod

The photons born in the first segment (A1) reach not just the corresponding closest detector (D1), but all detectors. This is shown in figure 38.

In order to investigate the extent to which the first segment (A1) affects all the dose rates, the source definition in the aforementioned MCNP model will be adjusted so that all photons originate from the activated materials within only this first segment. In this case this corresponds to stainless steel only, since boron carbide and hafnium are not significantly activated

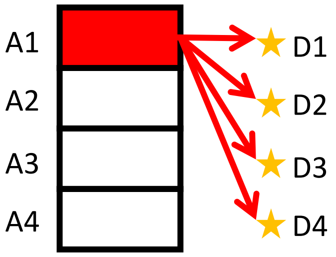

Figure 38: Dose rate contribution of a CR segment

(in comparison with stainless steel with a cobalt impurity, which thus dominates the overall CR activation).

The aforementioned model is then run to quantify all the dose rates (D1-D4) per Bq of A1. This approach assumes that the activity is homogeneously distributed within each segment. Repeating this process for all four rod segments (A1-A4) and adding up their respective contributions to the four dose rates (D1-D4) yields an expression for each dose rate in terms of the four activities:

$$D1 = c_{11}A1 + c_{12}A2 + c_{13}A3 + c_{14}A4, \tag{39}$$

$$D2 = c_{21}A1 + c_{22}A2 + c_{23}A3 + c_{24}A4, \tag{40}$$

$$D3 = c_{31}A1 + c_{32}A2 + c_{33}A3 + c_{34}A4, \tag{41}$$

$$D4 = c_{41}A1 + c_{42}A2 + c_{43}A3 + c_{44}A4. \tag{42}$$

This system of equations can also be expressed in matrix form, which can then be solved for the activities using matrix inversion, thus solving for total activity (in Bq) of each axial segment:

$$\vec{D} = \boldsymbol{C}\vec{A}, \tag{43}$$

$$\vec{A} = \boldsymbol{C}^{-1}\vec{D}. \tag{44}$$

The same approach applies to the actual CR characterization, with the only difference being the number of axial zones, which is larger than four. The exact number of zones depends on the user, though it cannot exceed the number of dose rate measurements (one dose rate measurement is needed for each axial zone) for the system of equations to be solvable. Inversely, it should also be noted that not all available dose rate measurements need to be used for the solution, with the unused ones available for example for validation.

Note that for cases where the individual dose rate measurements are taken at large distances from each other, and thus being representative of different parts of the component geometry, the matrix **A** becomes increasingly diagonally dominant, until it eventually becomes the identity matrix multiplied by a vector. At this point, each dose rate measurement is affected by only one section of the component.

An exploratory study was performed with Microshield, looking at underwater measurements of rod-like components with Co-60 source, such as the case shown in figure 35. It was found that for 40-cm-tall segments (corresponding to 40 cm intervals in measurements), 98.3% of the dose rate is caused by the direct contribution. As such, in cases where dose rate measurements are taken in intervals of 40 cm and larger, the characterization may be simplified by treating each 40 cm segment as a standalone component and applying the single-measurement methodology described in section 4.1.

The inverted **A** represents a general solution to the problem. As such, as soon as it's obtained, the activity profile can be automatically calculated from any set of dose rate measurement values. Therefore, only one set of calculations is needed per type of control rod, as long as the dose rate measurement locations are consistent.

Naturally, the same approach can be applied to other components, of any shape. This methodology has been used to characterize LPRMs and neutron sources.

The results produced are the total activities for each segment of the component in question. By knowing the mass of each segment, the activity concentration (in Bq/g) can then also be calculated.

4.4 NUMERICAL INSTABILITIES

When this methodology was applied to the characterization of BWR CRs, such as the one shown in figure 36, numerical instabilities were observed.

Specifically, the calculated activities would include values orders of magnitude higher than the expected values (based on previous CR characterization work), followed by negative activities (of the same magnitude) in the adjacent axial zone. This occurs because the defined methodology looks for an exact solution which leads to the exact provided dose rates. However, in reality, the measurements are associated with significant uncertainties. For example, if the value of D1 is not corresponding exactly to reality, this affects the activity of all neighboring axial segments. Furthermore, the homogeneous activity distribution assumption also affects this. This effect is particularly significant if the dose rate is large.

Attempts were made to overcome this by, instead of the simple matrix inversion, using an equation solver with additional constraints (activity must be positive) were unsuccessful, leading to axial zones with zero activity instead of negative activity. The best way to avoid these instabilities proved to be the modification of the axial zone definition. The system of equations was found to be most stable with segments no shorter than 10 cm. As such, if dose rate measurements are available at smaller intervals, these are not used for activity calculation. This resolution of 10 cm is sufficient for the purposes of control rod segmentation for waste packaging.

Another possibility is the direct post-processing of results. From previous experience, it is expected that the specific activity is highest at the top and decreases along the height. Note that this is observed for the specific activity, rather than activity, which may vary due to the variations in the mass. Based on this experience, in cases where the activity of a segment lower down is higher than the preceding segment just above it, their activity concentration is adjusted to be equal. The total activity for these segments is held constant. This procedure is shown in figure 39. (Note that the MCNP relative errors are not shown, as they are below 1% for all points shown.)

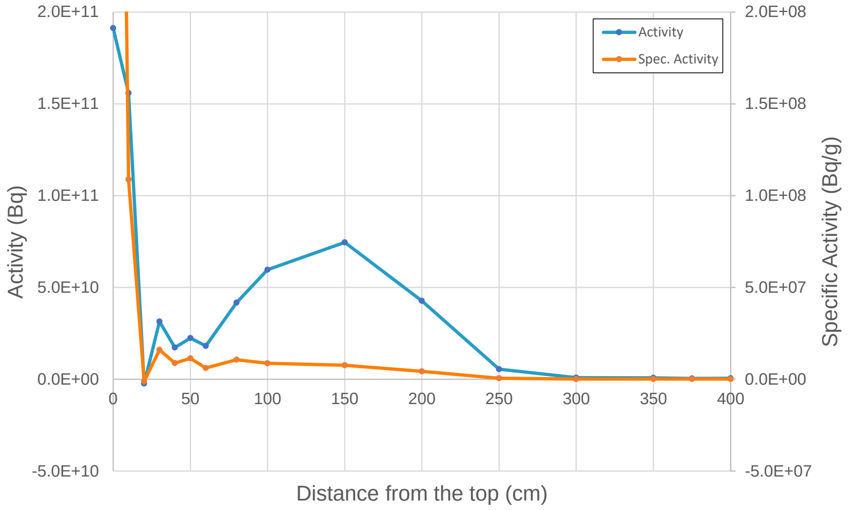

(a) Automatically calculated activity profile

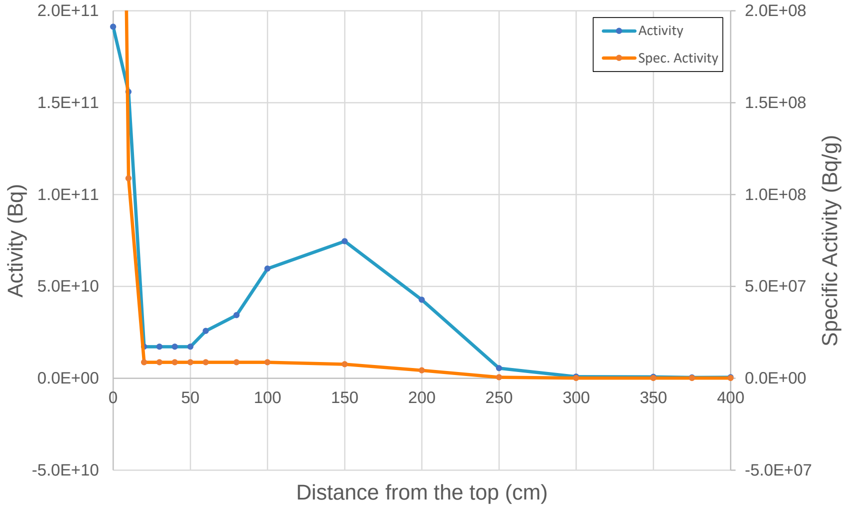

(b) Corrected activity profile

Figure 39: Numerical instabilities occurring during the characterization of some CR

Whenever this post-processing is applied, it's essential to validate the new activities against all available dose rate measurements. The resulting differences provide an insight into the accuracy of the final solution.

It bears repeating that this pathology was only observed for a fraction of the control rods analyzed. It was *not* observed during the characterization of other reactor waste components (such as LPRM).

4.5 OVERALL SUMMARY

The systematic general approach for reactor waste characterization presented in this chapter is based on the activation analysis methodology, originally developed for decommissioning waste characterization (as described in chapter 3), and as such benefits from all the developments done in this area. It also removes the need to create any new methodology or introduce new nuclear codes. Instead, the existing methodology is extended to accommodate the inherently more complex nature of the reactor waste components (e.g., control rods), which are not stationary, and for which the application of the irradiation history based approach would be very work intensive, or not possible at all due to insufficient irradiation information.

The presented approach for reactor waste characterization is based on both, the reconstruction of the total nuclide vector using the decommissioning waste characterization approach and the component dose rate measurements. The nuclide vectors are obtained using the neutron spectrum from a representative location (or a number of locations) from the full NPP model, coupled with the knowledge of the activated component's material composition and representative irradiation history. This vector is then interpreted to identify the nuclides responsible for the underwater gamma dose rate. Once this is known, one can pragmatically (using a simple Microshield model) link the dose rate to the activity of these gamma emitting nuclides, from which the full nuclide vector can be inferred.

In order to reconstruct the activity distribution from a component dose rate profile, a novel approach to reconstructing the activity distribution has been developed. A detailed MCNP (or Microshield) model of each (significantly different) component is created, and then used to quantify the contribution of each component segment to every single dose rate measurement. This relation can then be inverted, automatically calculating the activities of each (similar) component segment based on a given dose rate profile.

In the end, one obtains the component's total nuclide inventory, spatially resolved with the resolution based on the number of dose rate measurements, this providing the ability to carry out a detailed, hi-fidelity characterization of reactor waste components, while also benefiting from a much shorter engineering time (compared to conventional individual component characterization methods).

5 CONCLUSION

The objective of the work described in this thesis was the significant improvement of Nagra's most important radioactive waste characterization methodologies: for spent fuel, NPP (nuclear power plant) decommissioning waste, and reactor waste. The resulting high-fidelity nuclide inventories will decisively support the future waste disposal research and development, as well as serve the NPP decommissioning planning in general.

For spent fuel characterization, a new Polaris-based methodology has been demonstrated and its speed compared to the old TRITON-based approach. The methodology was then benchmarked against the industry-standard code sequence (Studsvik CMS), in order to confirm that, when the necessary fuel data is available, either one of these codes can be used to provide detailed nuclide vectors for the spent fuel.

For decommissioning waste, every step of the old characterization methodology has been further developed and improved upon. This includes a new, detailed, fully three-dimensional approach to NPP modeling and the development of a new activation sequence (based on the ORIGEN depletion solver), which outputs highly-resolved component-wise activation distribution and visualization. This methodology was then extended to provide additional applications of the method's results, specifically for algorithm-optimized packaging concepts and waste volume minimization through decay storage and free release analyses.

For reactor waste, the aforementioned decommissioning waste characterization methodology has been tailored to accommodate the more complex nature of the non-stationary components of this waste stream (such as control rods). A systematic general approach, based additionally on component dose rate measurements, allows for a more efficient and flexible characterization of the variety of reactor waste.

For each waste stream, directions for further improvements, and their requirements, have been identified.

All in all, the aforementioned developments serve as an important foundation in the ongoing transition from a conservative approach towards a superior best-estimate plus uncertainty (BEPU) waste characterization, which is vital for accurate safety analysis studies, as well as waste and cost minimization.

The results produced by these methodologies will form the basis for the next version of MIRAM (the Swiss Model Inventory of Radioactive

Materials), MIRAM2020, which is to be used for the repository general license application (RBG), to be submitted in 2024. They will also be used as part of the next Swiss NPP decommissioning cost study, KS2021. At the same time, the obtained results are already being provided to the Swiss NPPs planning their decommissioning, specifically Mühleberg (KKM) and Beznau (KKB), allowing detailed component-wise segmentation strategies and packaging concepts decision making, finally leading to notable cost reduction for the utilities.

Appendices

A ON THE USE OF COLOR

The methodology improvements described in this thesis lead to an increased level of detail available. This allows additional applications of the outputs and improves the overall information available to the user. However, at the same time, this renders the characterization results harder to present. For example, the activation analysis methodology presented in chapter 3 outputs, for each single component, hundreds of thousands of cells, each containing cell mass and a full nuclide vector. The amount of information can be overwhelming. As such, graphical representation of the selected quantities becomes increasingly important, turning into the primary way the user looks at the data (with additional processing accomplished by computer programs). Consequently, it's important to consider how exactly these figures are defined, and whether they are transmitting the information effectively. This section aims to start the discussion on best practices.

In general, visual representations of data sets are often pseudocolored to add additional information. This could represent a wide range of information types: heights above sea level on a map, shapes and object depth on a medical image (such as computed tomography scan), or energy information on an astronomical radiation chart. These colors are interpreted using a color map (provided in the figure legend). Most such maps are constructed by varying some color property, which can then be associated with low and high (numerical) values.

When picking a color map to use for a figure, it's important to first establish what type of information the figure is supposed to convey. For this, it's convenient to establish two separate types of such information: *numerical value information* and *form information* [131]. Numerical value information refers to quantitative data associated with each point on the figure, such as the specific activity or temperature in this location. This is sometimes called *metric values* in order to avoid confusion with the term *value* as defined in color theory, where it means *intensity*. Form information describes the shape of the surface, thereby aiding the three-dimensional visualization of the two-dimensional figure. This information allows easy identification of local minima and maxima, as well as any other changes in the surface gradient.

The main challenge for extracting metric information from a pseudocolored figure is the accuracy (and speed) with which a reader can interpret the corresponding color (in reference to the color map in the legend) without error. However, as the next section (A.1) demonstrates, this is a challenging task for many reasons. In scientific literature, pseudocolored plots most commonly use the *rainbow color map*, which is also the default in the majority of visualization toolkits [132]. However, numerous researchers argue that this color map is rarely the optimal choice [132–134]. The issues highlighted are outlined in section A.2. Recommendations for better color maps and the suggested color space to be used for color map creation are described in section A.3.

A.1 RELEVANT OPTICAL ILLUSIONS

Josef Albers wrote in his influential book *Interaction of Color* that "if one is not able to distinguish the difference between a higher tone and a lower tone, one should not make music. If a parallel conclusion were to be applied to color, almost everyone would prove incompetent for its proper use." [135] Without special tools, it's impossible to perceive a color other than in relation to other colors. As such, the perception of colors is always affected by the surrounding colors and other conditions (such as the lighting). Clearly, color perception is an intricate matter, subject to many challenges and perceptual biases. This section aims to highlight a selection of such biases deemed relevant for a definition of a suitable color map.

In ophthalmology, the most readable fonts are composed of letters which are easily differentiated from each other (because people don't read individual letters but rather words as a whole) [135]. Similarly, it's important to be able to distinguish between individual colors of a color map. However, this is often challenging, with one color sometimes looking like two different colors, and two colors sometimes looking alike.

The effect when the contrast of a perceived color is affected by the colors surrounding it is called *simultaneous contrast*. For example, a neutral gray square is perceived as lighter when surrounded by dark gray, and darker when surrounded by light gray. Ultimately, one color appears as two different colors. This is demonstrated in figure 40.

This effect could also be used to make two different colors look alike, as shown in figure 41. At the first glance, the two squares in the center appear to be of the same color. However, their comparison side by side (done on the right side of the image) clearly shows that they are not.

In this case, the background subtracts its hue from the colors located on top of it, whose perception it influences. This could be explained by recognizing that the perception of color is affected by *hue* and light (*luminance*). It can be concluded that the relative light-dark relationship between colors, as well as differences between them in hue, could be diminished or completely hidden. Biologically, this effect is believed to be caused by the balance of signals sent by the cone receptors and their effect on the cortical opponent processing channels. [131].

Another example of the surrounding of the color influencing its perception is the *Bezold effect* (named after Wilhelm von Bezold), which occurs

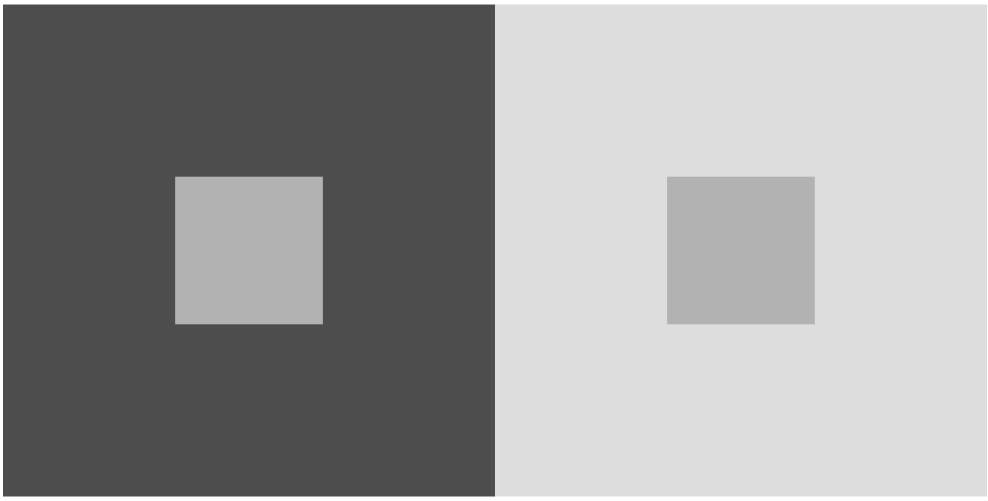

Figure 40: Example of the simultaneous contrast. Both small squares are of the same color (even though the appear to be different).

when small areas of color are surrounded by another color. This is demonstrated in figure 42, where small (brick-like) areas of red are surrounded by either black (on the left) or white (on the right) background. Rather than the two colors being perceived individually, they are *assimilated* together and substituted by a perceived combined color. This is referred to as *optical mixture* [135].

It's not only the directly adjacent colors which can influence one's color perception. *Successive contrast* is the effect where a color acts as an after-image, biasing the perception of colors viewed afterwards [136]. This is demonstrated in figure 43.

If one stares intently at the center of the red circle for 30 seconds and afterwards quickly shifts focus to the white circle, it will appear as blue-green instead of white. There are two competing biological explanation for this effect. One suggests that the cause is the tiring of the red-sensitive cones, which then send weaker signals upon viewing of the white circle [135]. Another argues that the red-sensitive cones are equally strained when viewing the white circle as when viewing the red one, and instead the prolonged exposure to the red color increases the *sensitivity* of the green- and blue-sensitive cones [137].

Due to these biases, when the reader is trying to understand a pseudo-color map, the perception of color at any point of the map is affected by the surrounding colors. These contrast effects are most prominent in cases with smooth color gradients—exactly the case for all continuous color maps. However, some color maps will be more susceptible to these biases than others [131].

Other than these optical illusions, which affect the majority of the population, it's important to also consider a condition which affects only a fraction of the population—*color blindness* (color vision deficiencies). Color

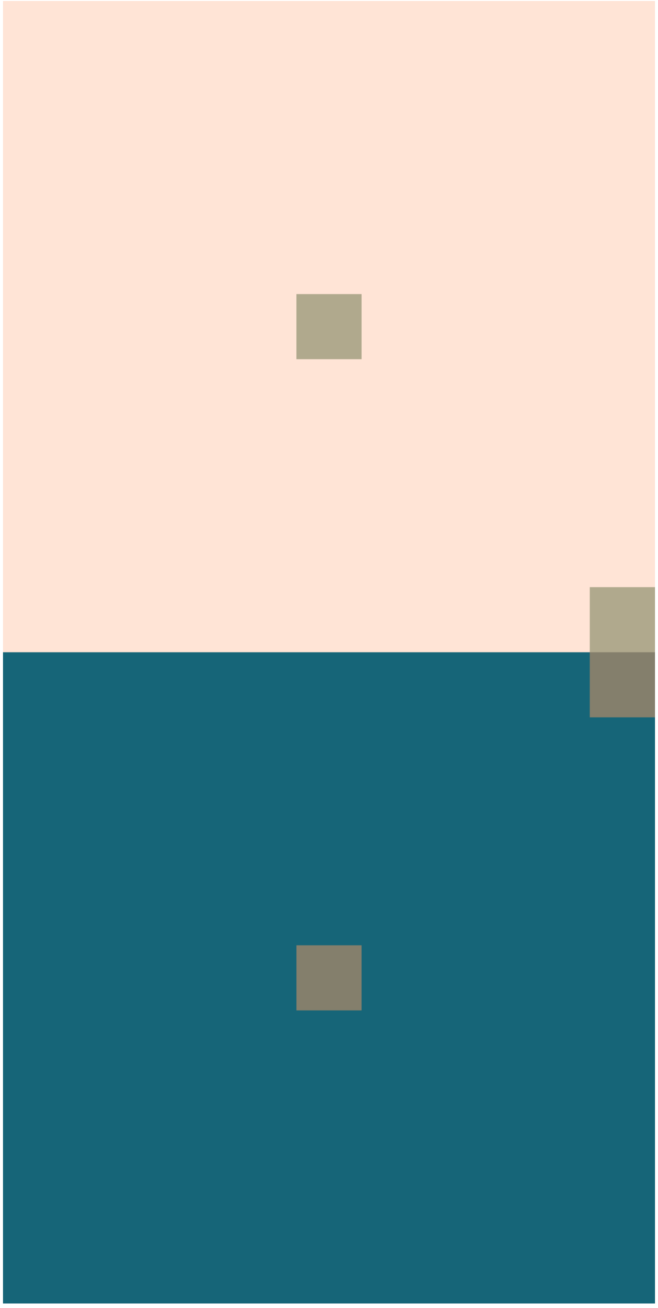

Figure 41: Example of the simultaneous contrast. The two squares are of different color (even though the appear to be of the same color).

blindness refers to genetic conditions, which decrease one's ability to differentiate between colors. Three types of colorblindness are considered here: *Protanopia* (deficient red cone), *Deuteranopia* (deficient green cone), *Tritanopia* (deficient blue cone). People with either of these types have *dichromatic* color vision—that is, only two (out of three) types of cones are working properly. Protanopia and Deuteranopia are the most common, with prevalence in the order of 8% for men and 0.5% for women of Northern European descent [138].

Based on the current understanding of the effects of these types of color blindness, it is possible to simulate how a person affected by either one of

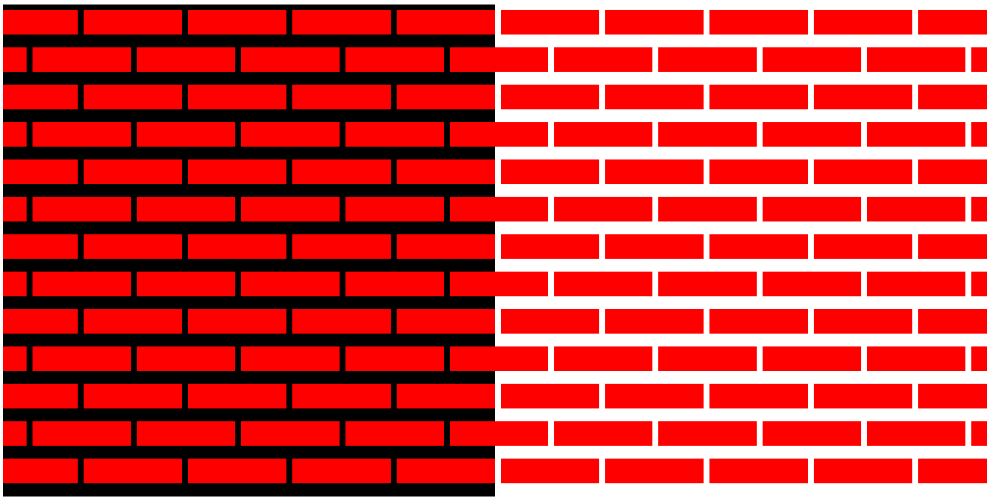

Figure 42: Bezold effect

these types of color blindness would perceive a given image [139]. This allows one to consider whether the designed color map would still be readable by a colorblind person, or whether it would be confusing. A good color map will maintain its readability for all three of these types of color blindness. This will be considered in the subsequent sections discussing proposed color maps.

A.2 ISSUES WITH THE RAINBOW COLOR MAP

As outlined at the beginning of this chapter, the commonly-used rainbow color map suffers from issues that make it non-ideal choice for most figures, leading numerous researchers from actively discouraging its use [132–134].

An ideal color map should be ordered in a perceptually-meaningful and intuitive way. For example the variations in luminance on a grayscale map, going from light shades (for high values) to dark shades (for low values) can be naturally interpreted by the reader. The ordering of the rainbow color map is based on the wavelength of the colors, which do not correspond to any perceptual order. In experiments [140] where people were asked to order red, yellow, green, and blue tokens, the resulting order varied from person to person. This demonstrates that the rainbow color map isn't naturally intuitive and requires constant reference to a legend, even for determining the relative order.

As illustrated in section A.1, the human visual perception is affected by hue and luminance (at the same time) [135, 141]. As can be seen in figure 44, which shows the visible light spectrum in grayscale (using Gray Gamma 2.2 profile [142] to simulate the human luminance perception), the rainbow color map has many sharp jumps in luminance, which the reader will perceive as abrupt changes in the values represented by the color. The rainbow color map also features large isoluminant portions. The differences between values in the range corresponding to these regions will

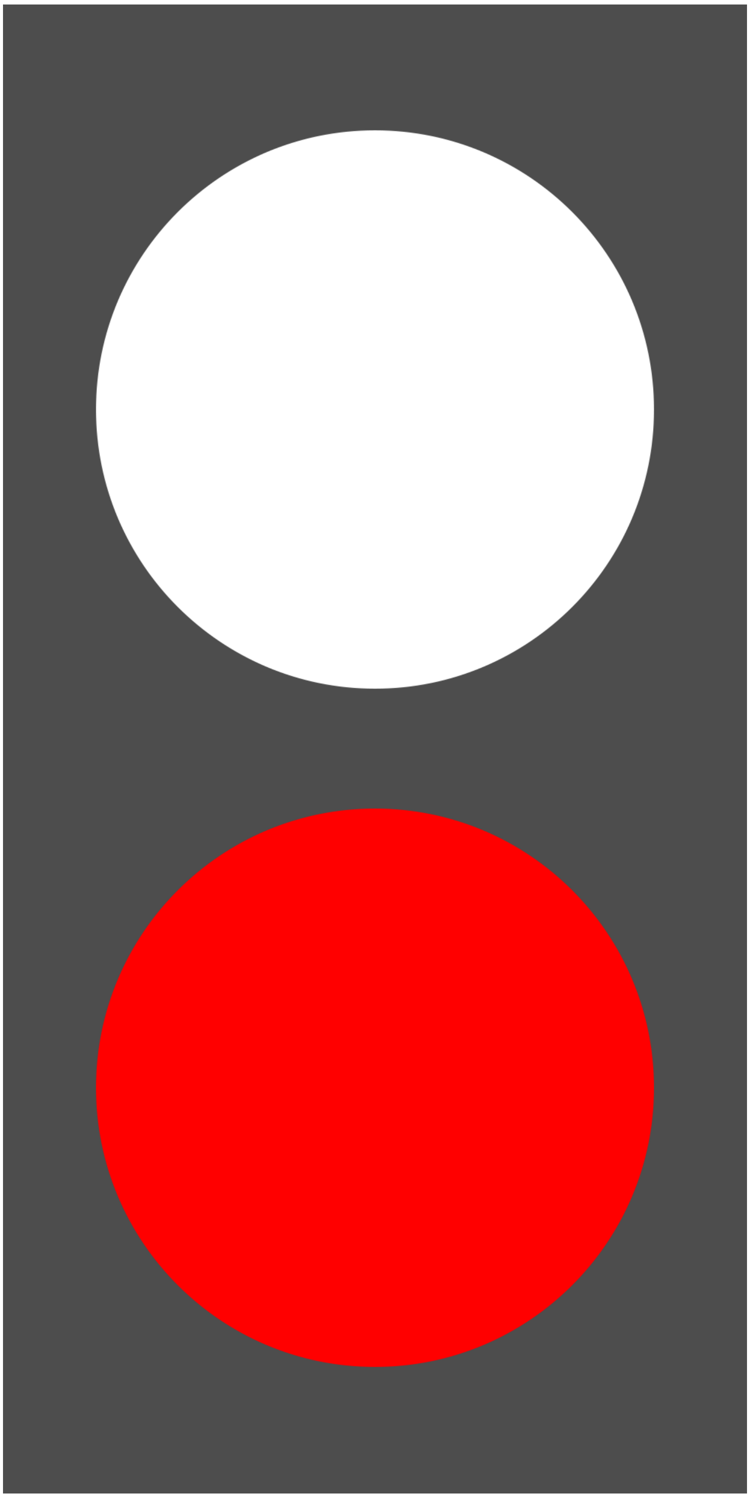

Figure 43: Example of the successive contrast

be obscured, with the reader perceiving large differences as small.

This tendency to mislead the reader with unintuitive changes in luminance can also be demonstrated using the spatial contrast sensitivity function [143, 144], as shown in figure 45 (originally from [132]). The x-axis represents (increasing) frequency, the y-axis represents (decreasing) contrast. The left side (a) uses the luminance-varying grayscale map, while

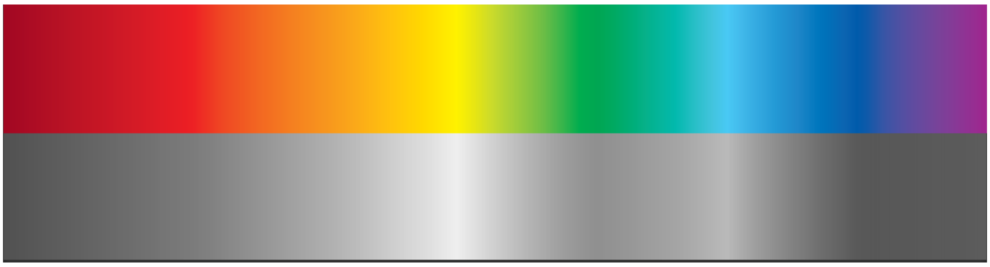

Figure 44: Visible light spectrum and its perceived luminance (using Gray Gamma 2.2 profile)

the right side (b) uses the rainbow color map. Clearly, the details can be differentiated at lower contrasts with the grayscale map than with the rainbow color map.

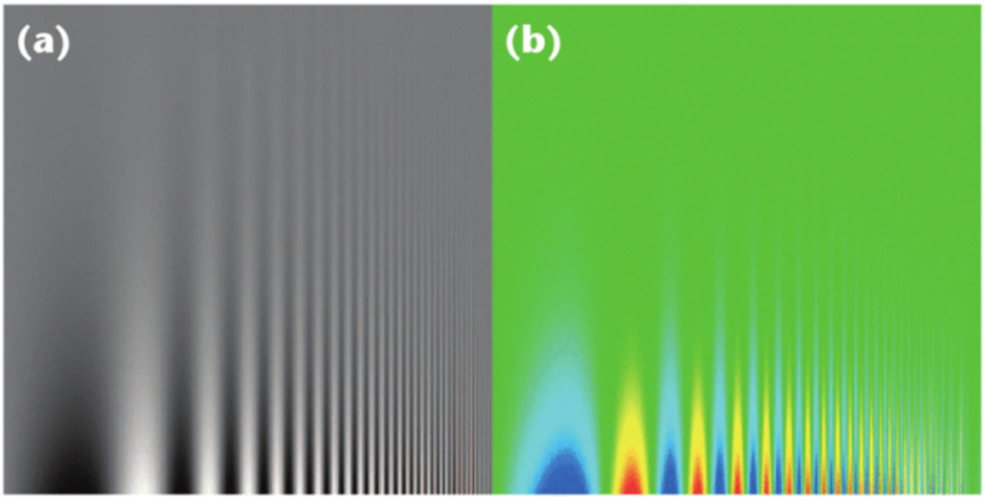

Figure 45: Spatial contrast sensitivity function in (a) grayscale and (b) rainbow color map. (© 2007 IEEE, from [132].)

Overall, the rainbow color map confuses and mislead the readers, failing the goal of the color map defined at the beginning of this chapter.

A.3 RECOMMENDATIONS FOR COLOR MAPS

The previous section (A.2) has demonstrated that the rainbow color map has numerous issues, due to which its use is generally discouraged. This conclusion necessitates the follow-up on what should be used instead of it. However, the answer is complex and problem-dependent. An attempt was made to collect recommendations which apply to the type of figures included in this thesis.

Published recommendations (such as [131]) suggest that a right color map should be suited to the underlying data, preferably chosen using an interactive tool for trial and error custom color map creation.

In general, when analyzing color maps, it's useful to transition away from the wavelength-based RGB spectrum and instead refer to colors in the *hue-chroma-luminance* (*HCL*) space, which is based on the human color perception [145, 146]. HCL color space is shown in figure 46. HCL-based color maps with user-defined variation in hue, chroma, and luminance can be automatically created using the *HCL Wizard* interactive tool [147].

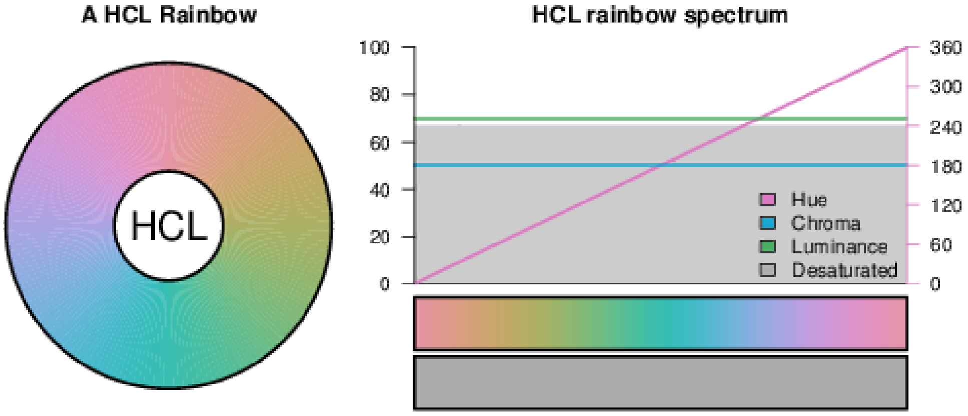

Figure 46: HCL "color rainbow" (🅭🅯 [147])

Note that when the HCL color palette is converted into grayscale, as shown in figure 46, the whole palette becomes a single shade of gray. That is because, on this figure, the color palette is shown for a particular luminance. As such, would would not simply use this palette as shown here.

For two-dimensional figures, such as flux maps (which show a single slice through the geometry), the color map should [131] increase monotonically in luminance, while at the same time cycling through a range of hues. Such color maps could be automatically created using the *cubehelix* color palette system [148]. The advantage of this approach is that, thanks to the increase in luminance, the information will be preserved even in case of a black and white printing or when viewed by a reader suffering from colorblindness.

Figures of three-dimensional objects whose surface is colored based on a color map, such as the figures showing activation of individual components, present a bigger challenge. The previous recommendation of value differentiation through a luminance gradient conflicts with the natural human perception's use of luminance for depth perception, interpreting object's three-dimensional shape [131, 132]. Some sources recommend that the color maps used in these cases should be isoluminant and instead differentiate values through changes in saturation and hue [132]. This is particularly relevant for two-dimensional figures showing three-dimensional features, such as a relief map, as well as the metric information. However, without the variation in luminance, the colors become very difficult to distinguish.

A.4 APPLICATION TO FLUX DISTRIBUTION MAPS

Based on these recommendations, an investigation was carried out, attempting to find a suitable color map for flux distribution maps, produced as part of MCNP NPP modeling described in chapter 3. The investigated maps were created using a variety of tools described in the previous section, most notable the *HCL Wizard* [147]. This section will use KKM as an example. A similar comparison carried out for KKB can be found in [87].

Since the rainbow color map was used for flux maps in the past, it's useful to evaluate the presented new color maps against it. Figure 47 shows the (total) neutron flux in KKM, visualized using the rainbow color map. For comparison, three potential replacements are presented:

- *HCL Rainbow*, which is an attempt to create a rainbow-like (blue-to-red) color map using the HCL color palette, can be seen in figure 48.
- *Viridis* is shown in figure 49.
- *Plasma* is shown in figure 50.

Clearly, all three of these replacements offer a superior ability to resolve between the values in the middle of the legend range. Regions which appear to be simply green in the rainbow color map, such as the bulb region of the drywell, are represented using a number of mutually-distinguishable colors in other color maps.

It should be noted that while the rainbow color map is continuous, the other color maps are discrete, defined using 14 discrete colors. This is a result of user experience, observing that continuous color maps are harder to read than the discrete ones. Note that the exact number of colors used (14) in these examples doesn't exactly match the number of orders of magnitude of the plotted flux map (11). This is caused by a modification of the flux range shown (done to highlight important streaming details), which was carried out after the discrete maps were prepared. Naturally, these color maps can also be defined with any number of discrete colors - both lower and higher than the 14 used here.

In the end, the plasma color map offers arguably the best contrast throughout the whole range (from the tested color maps), thus best fulfilling the goals defined at the beginning of this chapter. As can be seen in figure 51, showing the spectral specifications of the plasma color map, it follows the recommendations defined in section A.3. Furthermore, by utilizing a consistent increase in luminance, this color map also maintains readability in grayscale, as well as when viewed by a color blind person (of any of the three types defined in section A.1). This is demonstrated in figure 52, showing the simulated colorblind perception and grayscale of the continuous version of the plasma color map. As such, its use is recommended for all data visualization in two-dimensional space.

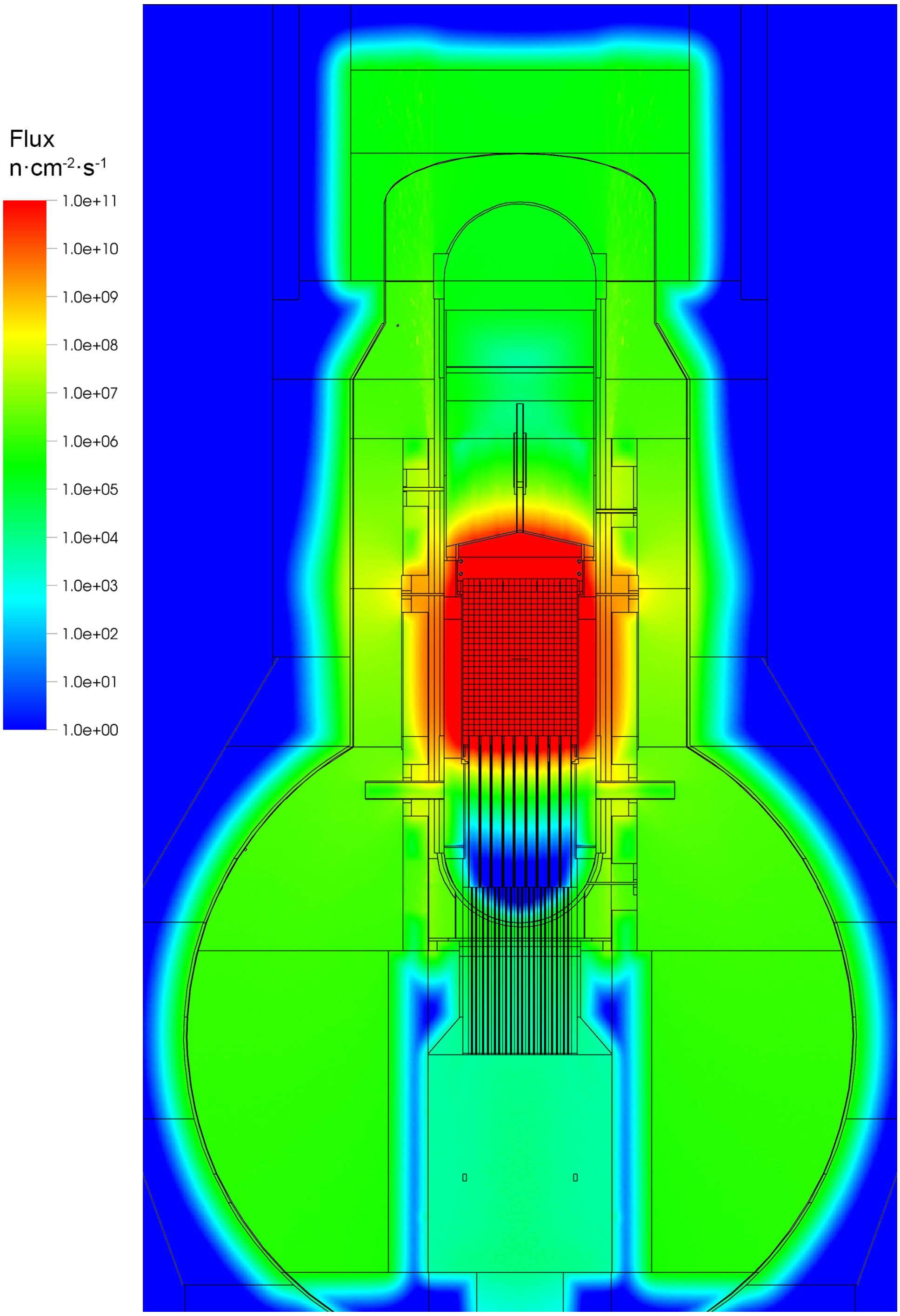

Figure 47: KKM (total) flux distribution with the *Rainbow* color map

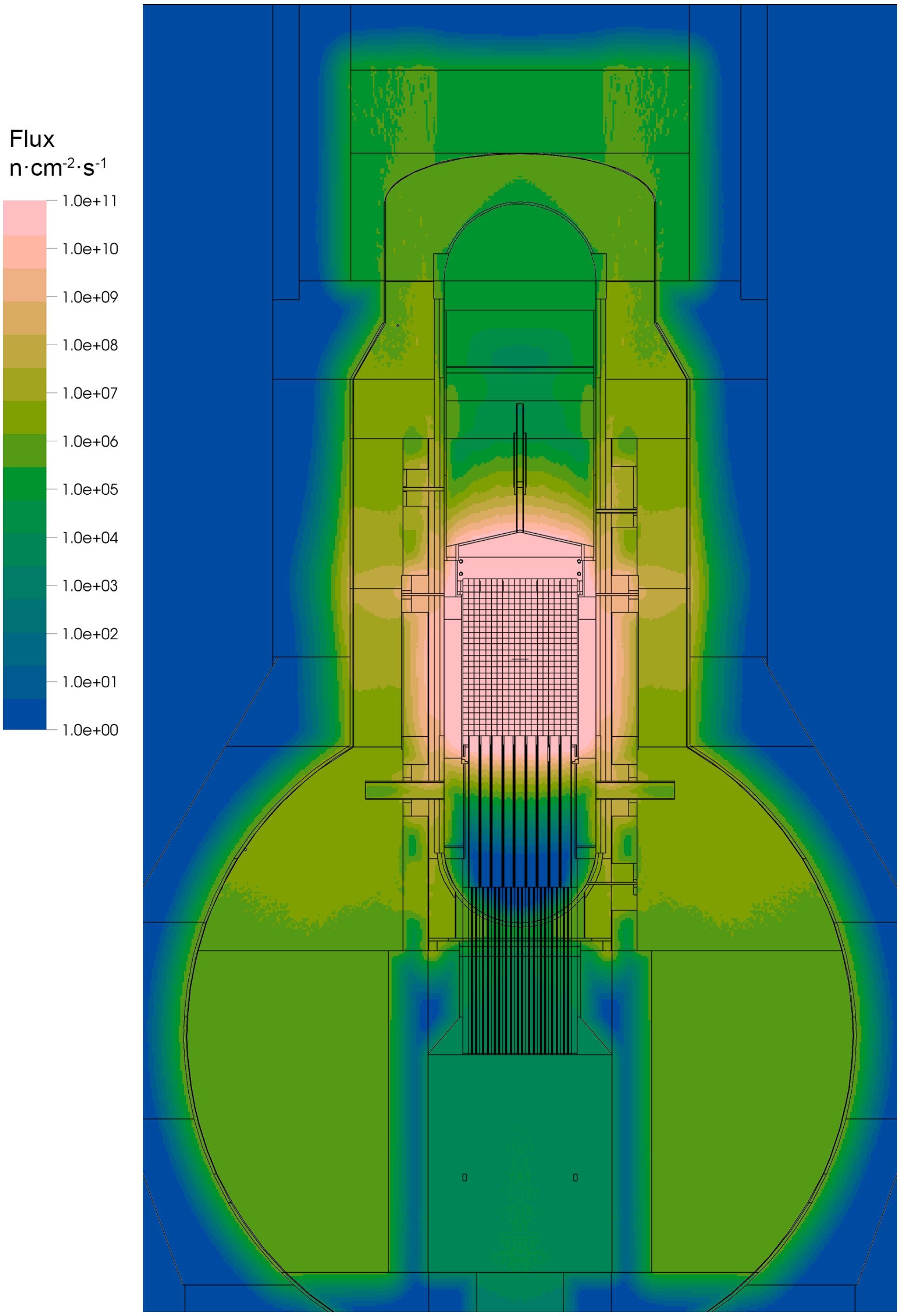

Figure 48: KKM (total) flux distribution with the *HCL Rainbow* color map

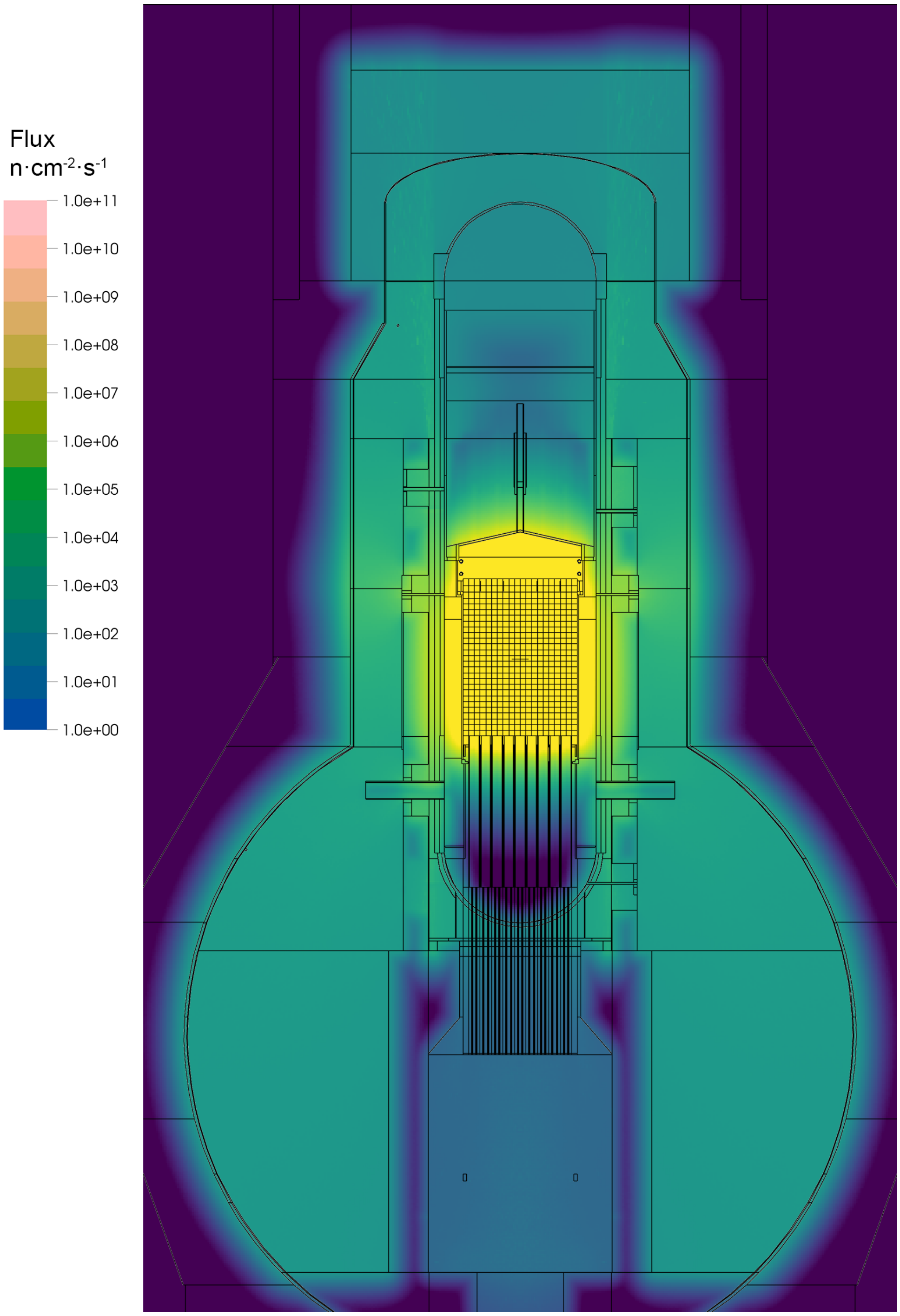

Figure 49: KKM (total) flux distribution with the *Viridis* color map

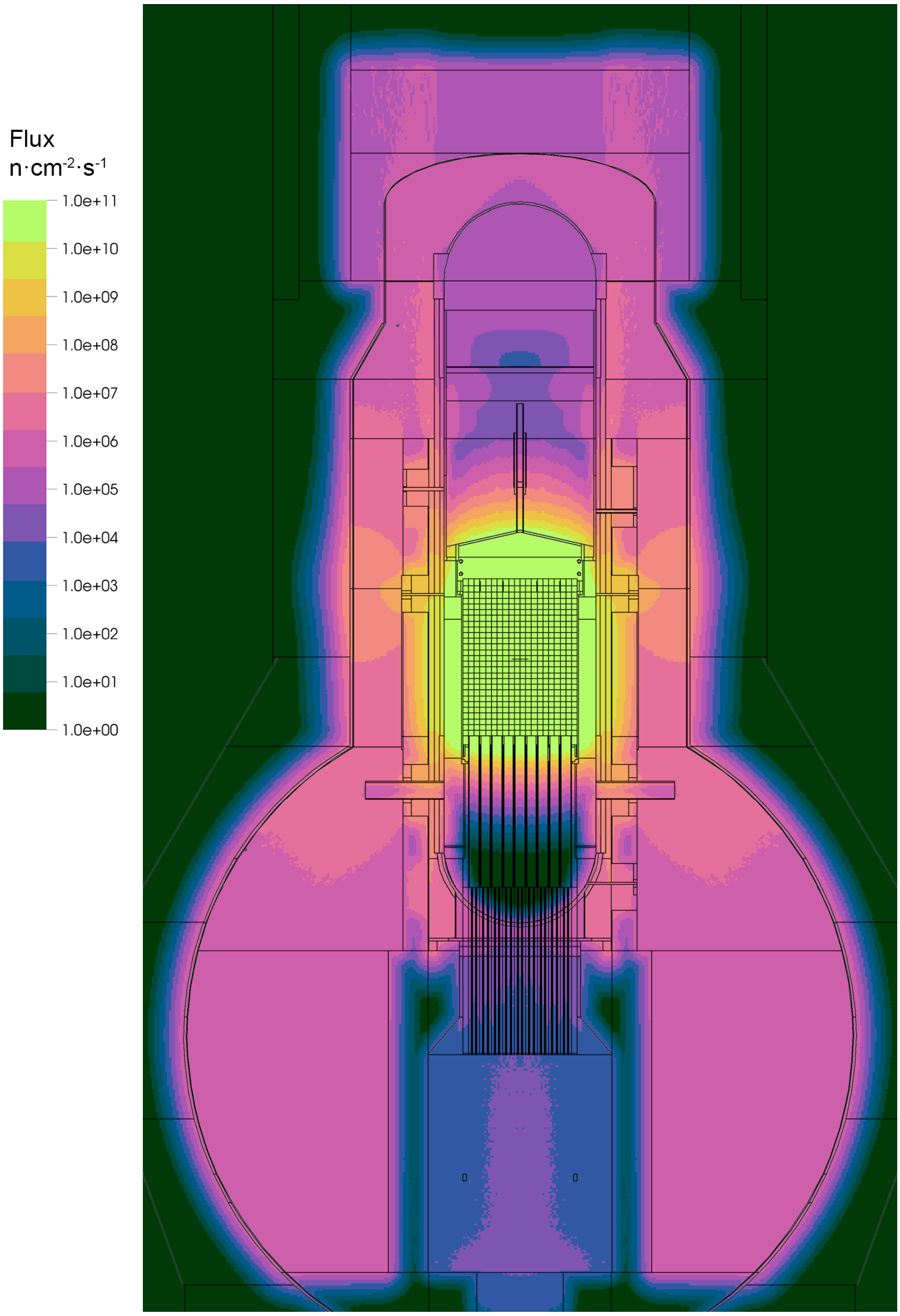

Figure 50: KKM (total) flux distribution with the *Plasma* color map

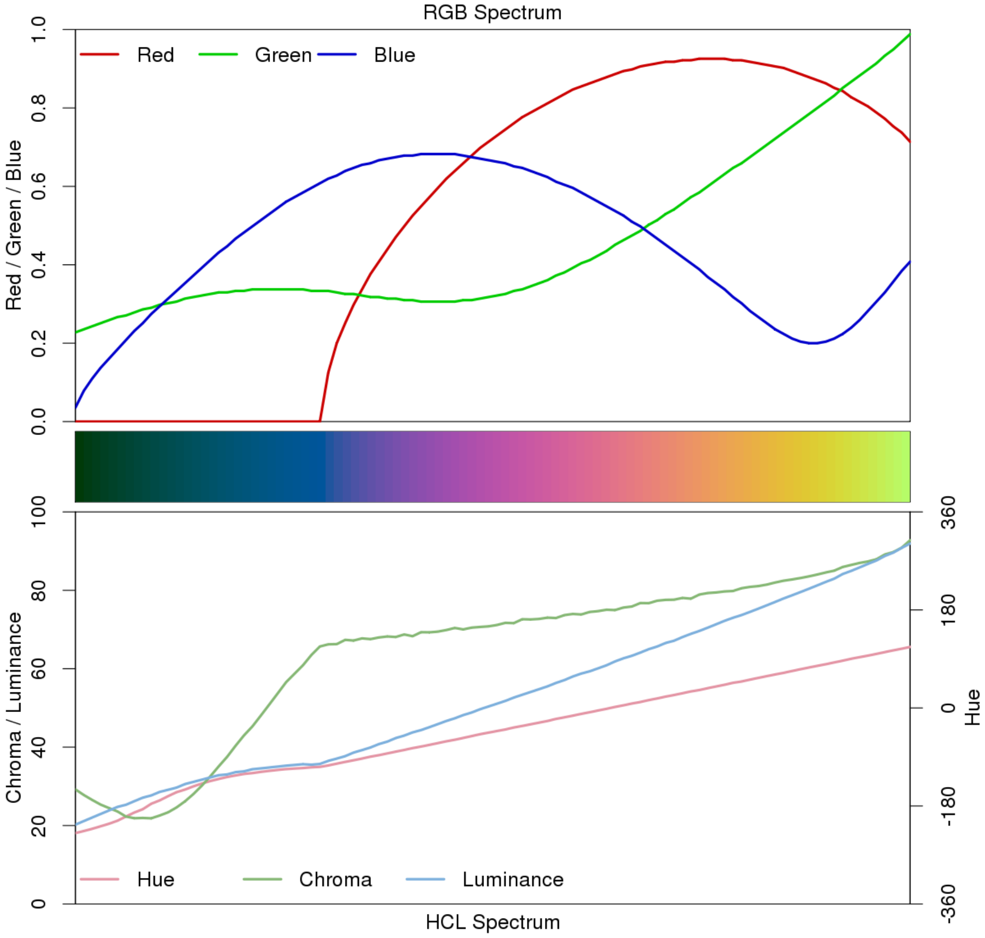

Figure 51: Proposed *Plasma* color map (continuous) spectral information (generated using [147])

Initial applications of the plasma color map were met with skepticism, emphasizing that despite its many flaws, the rainbow color map remains the industry standard, and the one that people expect to see. However, it is this author's strongly-held belief that once the novelty of the plasma color map wears of, its superior contract will outweigh the familiarity of the rainbow color map.

Recommendations for color maps to be used in three-dimensional space, such as component-wise activation maps, are currently in development. However, the recommendation of using a discrete color map over a continuous one also apply here.

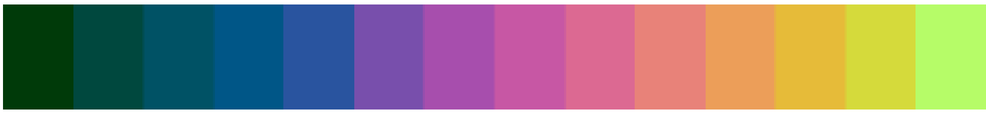

(a) normal vision

(b) protan vision

(c) deutan vision

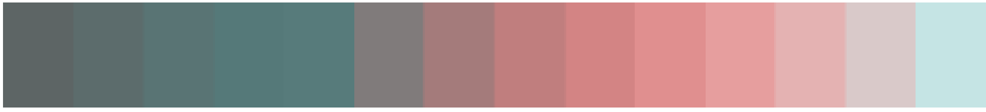

(d) tritan vision

(e) grayscale

Figure 52: Proposed *Plasma* color map (14-step discrete), as viewed with different types of color vision deficiencies

BIBLIOGRAPHY

[1] IAEA. *Nuclear Power Reactors in the World*. 2018 Edition. International Atomic Energy Agency, 2018-06-30. ISBN: 978-92-0-101418-4. URL: `https://www-pub.iaea.org/books/IAEABooks/13379/Nuclear-Power-Reactors-in-the-World` (visited on 2018-09-19).

[2] OECD/IEA. *World Energy Outlook 2014*. International Energy Agency, 2014. ISBN: 978-92-64-20805-6. URL: `https://www.iea.org/publications/freepublications/publication/WEO2014.pdf` (visited on 2018-09-19).

[3] IAEA. *Status of the Decommissioning of Nuclear Facilities around the World*. Tech. rep. IAEA, 2004. URL: `https://www-pub.iaea.org/MTCD/Publications/PDF/Pub1201_web.pdf`.

[4] IAEA. *Joint Convention on the Safety of Spent Fuel Management and on the Safety of Radioactive Waste Management*. Tech. rep. IAEA, 1997. URL: `https://www.iaea.org/sites/default/files/infcirc546.pdf`.

[5] Die Bundesversammlung der Schweizerischen Eidgenossenschaft. *Bundesgesetz über den Umweltschutz (USG)*. 1983-10-07. URL: `https://www.admin.ch/opc/de/classified-compilation/19830267/index.html` (visited on 2018-09-01).

[6] Die Bundesversammlung der Schweizerischen Eidgenossenschaft. *Kernenergiegesetz (KEG)*. 2003-03-21. URL: `https://www.admin.ch/opc/de/classified-compilation/20010233/index.html` (visited on 2018-08-01).

[7] Der Schweizerische Bundesrat. *Stilllegungs- und Entsorgungsfondsverordnung (SEFV)*. 2007-12-07. URL: `https://www.admin.ch/opc/de/classified-compilation/20070457/index.html` (visited on 2018-08-01).

[8] STENFO. *Jahresbericht 2017*. Tech. rep. STENFO, 2018-06-28. URL: `http://www.stenfo.ch/sites/default/files/documents/2018-08/Jahresbericht%202017%20EntsF_VK_genehmigt%20am%2028.%20Juni%202018.pdf` (visited on 2018-09-19).

[9] swissnuclear. *Kostenstudie 2016 (KS16)*. Tech. rep. Fachgruppe Kernenergie der swisselectric, 2016-10-31. URL: `http://www.swissnuclear.ch/de/downloads/217.html` (visited on 2018-09-19).

[10] Nagra. *Annual report 2017*. Tech. rep. Nagra, 2017. URL: `https://www.nagra.ch/display.cfm/id/102774/disp_type/display/filename/e_gb_2017.pdf` (visited on 2018-09-19).

[11] IAEA. *Classification of Radioactive Waste*. Tech. rep. General Safety Guide No. GSG-1. IAEA, 2009. URL: `https://www-pub.iaea.org/MTCD/Publications/PDF/Pub1419_web.pdf`.

[12] IAEA. *Application of the Concepts of Exclusion, Exemption and Clearance*. STI/PUB/1202. 2004. ISBN: 92-0-109404-3. URL: `https://www-pub.iaea.org/books/iaeabooks/7118/Application-of-the-Concepts-of-Exclusion-Exemption-and-Clearance`.

[13] Der Schweizerische Bundesrat. *Strahlenschutzverordnung (StSV)*. 2017-04-26. URL: `https://www.admin.ch/opc/de/classified-compilation/20163016/index.html` (visited on 2018-08-01).

[14] Der Schweizerische Bundesrat. *Kernenergieverordnung (KEV)*. 2004-12-10. URL: `https://www.admin.ch/opc/de/classified-compilation/20042217/index.html` (visited on 2018-08-01).

[15] Nagra. *Modellhaftes Inventar für radioaktive Materialien MIRAM 14*. Tech. rep. NTB 14-04. Nagra, 2014.

[16] BKW. *Stilllegung Kernkraftwerk Mühleberg*. Tech. rep. BKW, 2018. URL: `https://www.bkw.ch/stilllegungsbroschuere` (visited on 2018-09-19).

[17] ENSI. *Freimessung von Materialien und Bereichen aus kontrollierten Zonen*. Tech. rep. ENSI-B04/d. ENSI, 2009-08. URL: `http://static.ensi.ch/1330592503/ensi-b04_d.pdf` (visited on 2018-10-31).

[18] Bundesamt für Energie. *Sachplan geologische Tiefenlager - Konzeptteil 2011*. Tech. rep. BFE, 2011-11-30. URL: `http://www.bfe.admin.ch/php/modules/publikationen/stream.php?extlang=de&name=de_687132619.pdf` (visited on 2018-09-30).

[19] IAEA. *Status and Trends in Spent Fuel and Radioactive Waste Management*. IAEA Nuclear Energy Series NW-T-1.14. Vienna: International Atomic Energy Agency, 2018-03-27. 57 pp. ISBN: 978-92-0-108417-0. URL: `https://www.iaea.org/publications/11173/status-and-trends-in-spent-fuel-and-radioactive-waste-management`.

[20] M. Morales Gutierrez. "Development and Validation of 2D and 3D SCALE LWR Fuel Assembly Models for Burnup Calculations and Activation Studies". MSc Thesis. ETH Zürich, 2015.

[21] S. Caruso and A.-L. Panadero. "Development and Validation of Ad Hoc ORIGEN-ARP Libraries for Very High Burnup UO2 PWR Fuel with SCALE/TRITON". In: *Proceedings of the PHYSOR 2014 Conference*. 2014. DOI: `10.11484/jaea-conf-2014-003`.

[22] S. Caruso. "From a Conservative Approach to a BEPU Implementation for Spent Nuclear Fuel Characterization and Safety Assessment from the Perspective of Geological Disposal". In: *Proceedings of the BEPU 2018 Conference*. BEPU2018 KN-E3. 2018.

[23] ORNL. *Scale: A Comprehensive Modeling and Simulation Suite for Nuclear Safety Analysis and Design*. ORNL/TM-2005/39. Version 6.1. Available from Radiation Safety Information Computational Center at Oak Ridge National Lab. as CCC-785. Oak Ridge National Lab., 2011.

[24] Stefano Caruso. "Estimation of the radionuclide inventory in LWR spent fuel assembly structural materials for long-term safety analysis". In: *EPJ Nuclear Sciences & Technologies* 2 (2016), p. 4. DOI: `10.1051/epjn/e2015-50057-8`.

[25] Mark D. DeHart and Stephen M. Bowman. “Reactor Physics Methods and Analysis Capabilities in SCALE”. In: *Nuclear Technology* 174.2 (2011-05), pp. 196–213. DOI: 10.13182/nt174-196.

[26] C. L. Dembia, G. D. Recktenwald, and M. R. Deinert. “Bondarenko method for obtaining group cross sections in a multi-region collision probability model”. In: *Progress in Nuclear Energy* 67 (2013-08), pp. 124–131. DOI: 10.1016/j.pnucene.2013.02.001.

[27] Mark D. DeHart, Ronald E. Pevey, and Theodore A. Parish. “An extended step characteristic method for solving the transport equation in general geometries”. In: *Nuclear science and engineering* 118.2 (1994), pp. 79–90.

[28] M. D. DeHart. “A Discrete Ordinates Approximation to the Neutron Transport Equation Applied to Generalized Geometries”. PhD thesis. Texas A&M University, 1992. URL: https://www.osti.gov/servlets/purl/10173922 (visited on 2018-08-01).

[29] Tanay Mazumdar and S. B. Degweker. “Solution of neutron transport equation by Method of Characteristics”. In: *Annals of Nuclear Energy* 77 (2015-03), pp. 522–535. DOI: 10.1016/j.anucene.2014.12.029.

[30] Stewart Schlesinger. “Terminology for model credibility”. In: *Simulation* 32.3 (1979), pp. 103–104.

[31] P. Grimm, I. Günther-Leopold, and H. D. Berger. “Burnup calculations and chemical analysis of irradiated fuel samples studied in LWR-PROTEUS phase II”. In: *Proceedings of the PHYSOR 2006 conference*. 2006.

[32] S. Caruso and F. Jatuff. “Design, development and utilisation of a tomography station for γ-ray emission and transmission analyses of light water reactor spent fuel rods”. In: *Progress in Nuclear Energy* 72 (2014-04), pp. 49–54. DOI: 10.1016/j.pnucene.2013.09.007.

[33] S. Caruso et al. “Comparison of optimised germanium gamma spectrometry and multicollector inductively coupled plasma mass spectrometry for the determination of 134Cs, 137Cs and 154Eu single ratios in highly burnt UO2”. In: *Nuclear Instruments and Methods in Physics Research Section A: Accelerators, Spectrometers, Detectors and Associated Equipment* 589.3 (2008-05), pp. 425–435. DOI: 10.1016/j.nima.2008.03.005.

[34] B. T. Rearden and M. A. Jessee. *SCALE Code System, Version 6.2.3*. Oak Ridge National Lab. 2018-03. DOI: 10.2172/1426571.

[35] Matthew Anderson Jessee et al. “POLARIS: A New Two-Dimensional Lattice Physics Analysis Capability for the SCALE Code System”. In: *Proceedings of the PHYSOR 2014 Conference*. 2014.

[36] Mark L. Williams and Kang Seog Kim. “The Embedded Self-Shielding Method”. In: *Proceedings of the PHYSOR 2012 Conference*. 2012.

[37] Thomas M. Evans et al. “Denovo: A New Three-Dimensional Parallel Discrete Ordinates Code in SCALE”. In: *Nuclear Technology* 171.2 (2010-08), pp. 171–200. DOI: 10.13182/nt171-171.

[38] Elmer E. Lewis and Warren F. Miller Jr. *Computational Methods of Neutron Transport*. Amer Nuclear Society, 1993. ISBN: 0-89448-452-4.

[39] J. Rhodes, D. Lee, and K. Smith. *CASMO-5/CASMO-5M – A Fuel Assembly Burnup Program Methodology Manual*. SSP-08/405. Studsvik Scandpower. 2008.

[40] Ian C. Gauld et al. “Integral nuclear data validation using experimental spent nuclear fuel compositions”. In: *Nuclear Engineering and Technology* 49.6 (2017-09), pp. 1226–1233. DOI: `10.1016/j.net.2017.07.002`.

[41] F. Michel-Sendis et al. “SFCOMPO-2.0: An OECD NEA database of spent nuclear fuel isotopic assays, reactor design specifications, and operating data”. In: *Annals of Nuclear Energy* 110 (2017-12), pp. 779–788. DOI: `10.1016/j.anucene.2017.07.022`.

[42] T. Bahadir, R. M. Ferrer, and J. D. Rhodes. *CMSLINK5 User's Manual*. SSP-10/437. Version Rev 5. 2015.

[43] S.-Ö. Lindahl, T. Bahadır, and G. Grandi. *SIMULATE-5 Methodology*. SSP-10/465. Studsvik Scandpower. 2011.

[44] A. Noël, R. Vielma, and A. DiGiovine. “Modernization of Kernkraftwerk Beznau's core monitoring system with Studsvik's Gardel system”. In: *Proceedings of the ICAPP 2007 Conference*. INIS-FR–08-0263. 2007.

[45] S. Caruso. “On-line Core Monitoring at the BEZNAU PWRs”. In: *Proceedings of the IYNC 2008*. 2008.

[46] A. DiGiovine and A. Noël. “GARDEL-PWR: Studsvik's Online Monitoring and Reactivity Management System”. In: *Proceedings of Advances In Nuclear Fuel Management III*. 2003.

[47] A. Noël et al. “GARDEL BWR on-line monitoring experience at Cooper and Monticello”. In: *Transactions of the American Nuclear Society and the European Nuclear Society* 97 (2007-11), pp. 737–738. ISSN: 0003-018X. URL: `https://www.studsvik.com/SharepointFiles/GARDEL%20BWR%20On-line%20Monitoring%20Experience%20at%20Cooper%20and%20Monticello.pdf`.

[48] M. Edenius and K. Smith. “Studsvik core management system”. In: *Nuclear Europe Worldscan* 11 (1991), p. 22. ISSN: 1016-5975.

[49] G. Grandi and L. Belblidia. “Studsvik CMS Capability for Reactivity Initiated Accidents”. In: *LWR Fuel Performance Meeting, Top Fuel 2013*. Vol. 1. 2013, pp. 489–496. URL: `https://www.researchgate.net/profile/Gerardo_Grandi/publication/287187032_Studsvik_CMS_capability_for_reactivity_initiated_accidents/links/56f2cd3b08ae38d7109a501d/Studsvik-CMS-capability-for-reactivity-initiated-accidents.pdf`.

[50] OECD/NEA. *Fuel Safety Criteria in NEA Member States*. Tech. rep. NEA/CSNI/R(2003)10. Nuclear Energy Agency, 2013. URL: `https://www.oecd-nea.org/nsd/docs/2003/csni-r2003-10.pdf`.

[51] IAEA. *Periodic Safety Review for Nuclear Power Plants*. IAEA Safety Standards Series SSG-25. Vienna: International Atomic Energy Agency, 2013. ISBN: 978-92-0-137410-3. URL: `http://www-pub.iaea.org/books/IAEABooks/8911/Periodic-Safety-Review-for-Nuclear-Power-Plants`.

[52] N. Horelik et al. "Benchmark for Evaluation and Validation of Reactor Simulations (BEAVRS), v1.0.1". In: *Proceedings of the M&C 2013 Conference*. 2013.

[53] V. Bykov et al. "Solution of the BEAVRS Benchmark using CASMO-5 / SIMULATE-5 Code Sequence". In: *Proceedings of the PHYSOR 2016 Conference*. 2016.

[54] Min Ryu et al. "Solution of the BEAVRS benchmark using the nTRACER direct whole core calculation code". In: *Journal of Nuclear Science and Technology* 52.7-8 (2015-05), pp. 961–969. DOI: `10.1080/00223131.2015.1038664`.

[55] J. D. Rhodes et al. *CASMO5 User's Manual*. SSP-07/431 Rev 5. Studsvik Scandpower. 2012-10.

[56] S. Børresen and A. Becker. "Calculation of Neutron Emission from Spent LWR Fuel Assemblies: SNF Method and Validation". In: *Proceedings of the PHYSOR 2008 conference*. 2008.

[57] A. Becker and G. Anton. "SNF: Spent Fuel Analyses based on CASMO/SIMULATE In-Core Fuel Management". In: *Proceedings of the Advances in Nuclear Fuel Management IV (ANFM 2009) Conference*. 2009.

[58] A. Becker, G. Anton, and S. Børresen. "SNF Calculations of Spent Fuel Source Terms for Fuel Pools and Storage Casks". In: *Transactions of the American Nuclear Society and the European Nuclear Society* 97 (2007), pp. 211–212. ISSN: 0003-018X.

[59] S. Børresen. "Spent Nuclear Fuel Analyses based on In-Core Fuel Management Calculations". In: *Proceedings of the PHYSOR 2004 conference*. 2004.

[60] S. Børresen, T. Bahadır, and M. Kruners. "Validation of CMS/SNF Calculations against preliminary CLAB Decay Heat Masurements". In: *Transactions of the American Nuclear Society* 91 (2004), pp. 435–436. ISSN: 0003-018X.

[61] T. Simeonov, J. M. Hykes, and J. D. Rhodes III. *SNF User's Manual*. SSP-11/328 REV7. Studsvik Scandpower. 2018-03.

[62] SKB. *Radionuclide transport report for the safety assessment SR-Site*. Tech. rep. TR-10-50. Version Updated 2015-05. Svensk Kärnbränslehantering AB, 2010-12. URL: `http://www.skb.se/upload/publications/pdf/TR-10-50.pdf` (visited on 2018-08-01).

[63] J. C. Tait and J. R. Theaker. *Light element radionuclides in used fuel and their potential contribution to postclosure safety assessment*. Tech. rep. AECL-11431, COG-95-440. Atomic Energy of Canada Limited, 1996-09. URL: `http://www.iaea.org/inis/collection/NCLCollectionStore/_Public/28/076/28076922.pdf?r=1`.

[64] M. B. Chadwick et al. “ENDF/B-VII.1 Nuclear Data for Science and Technology: Cross Sections, Covariances, Fission Product Yields and Decay Data”. In: *Nuclear Data Sheets* 112.12 (2011-12), pp. 2887–2996. DOI: `10.1016/j.nds.2011.11.002`.

[65] J. J. Herrero et al. *Criticality Safety Assessment for Geological Disposal of Spent Fuel using PSI BUCSS-R Methodology*. Tech. rep. NAB 17-23. Nagra, 2017-10.

[66] IAEA. *Review of Fuel Failures in Water Cooled Reactors*. International Atomic Energy Agency, 2010. ISBN: 978-92-0-102610-1. URL: `https://www-pub.iaea.org/books/iaeabooks/8259/Review-of-Fuel-Failures-in-Water-Cooled-Reactors` (visited on 2018-09-24).

[67] IAEA. *Radiological Characterization of Shut-Down Nuclear Reactors for Decommissioning Purposes*. Tech. rep. Technical reports series No. 389. IAEA, 1998. URL: `https://www-pub.iaea.org/MTCD/Publications/PDF/TRS389_scr.pdf`.

[68] Manuel Pantelias Garcés. “Activation Neutronics for the Swiss Nuclear Power Plants”. PhD thesis. ETH Zürich, 2013. DOI: `10.3929/ethz-a-010206697`.

[69] Richard Hanzel, Tibor Rapant, and Jaroslav Svitek. “Radiological characterisation on V1 NPP technological systems and buildings - Contamination”. In: *Workshop on Radiological characterisation for decommissioning - Compilation of abstracts, papers, presentations and posters*. NEA-WPDD–2012-04-17-19. OECD/NEA. 2012. URL: `https://inis.iaea.org/collection/NCLCollectionStore/_Public/45/073/45073602.pdf` (visited on 2018-09-24).

[70] U. Hesse and K. Gewehr. *GRSAKTIV: Ein Programmsystem zur Berechnung der Aktivierung von Brennelement- und Core-Bauteilen*. Tech. rep. GRS-A-2249. Gesellschaft für Anlagen- und Reaktorsicherheit, 1995.

[71] Manuel Pantelias Garcés. “Monte Carlo Simulation for Reactor Pressure Vessel Activation Analysis”. MSc Thesis. ETH Zürich, 2010-04.

[72] C. J. Werner, ed. *MCNP Users Manual - Code Version 6.2*. LA-UR-17-29981. 2017. URL: `https://laws.lanl.gov/vhosts/mcnp.lanl.gov/pdf_files/la-ur-17-29981.pdf`.

[73] V. Bykov. “Enhancement and Validation of the NPP Mühleberg MCNP Activation Simulations for Swiss Decommissioning Planning”. MSc Thesis. ETH Zürich, 2014.

[74] U. Hesse and K. Hummelsheim. *GRSAKTIV-II: Ein Programmsystem zur Berechnung der Aktivierung von Brennelement- und Core-Bauteilen in Vielgruppendarstellung*. Tech. rep. GRS-A-3002. Gesellschaft für Anlagen- und Reaktorsicherheit, 2001.

[75] Ben Volmert and Manuel Pantelias. *Stilllegungsstudie 2011: Radiologische Inventare der aktivierten Grundmaterialen des KKM*. Tech. rep. NAB 11-12. Nagra, 2011-11.

[76] Ben Volmert and Manuel Pantelias. *Stilllegungsstudie 2011: Radiologische Inventare der aktivierten Grundmaterialen des KKL*. Tech. rep. NAB 11-11. Nagra, 2011-11.

[77] Ben Volmert and Manuel Pantelias. *Stilllegungsstudie 2011: Radiologische Inventare der aktivierten Grundmaterialen des KKB*. Tech. rep. NAB 11-13. Nagra, 2011-11.

[78] Ben Volmert and Manuel Pantelias. *Stilllegungsstudie 2011: Radiologische Inventare der aktivierten Grundmaterialen des KKG*. Tech. rep. NAB 11-14. Nagra, 2011-11.

[79] Pavol Zvoncek. "Comparison and Suitability Analysis of Codes for NPP Ex-Core Activation Calculations". MSc Thesis. ETH Zürich, 2012.

[80] J. C. Evans et al. *Long-lived activation products in reactor materials*. Tech. rep. NUREG/CR-3474. Pacific Northwest National Lab., 1984-08. DOI: `10.2172/6776358`.

[81] Ronald J. McConn et al. *Compendium of Material Composition Data for Radiation Transport Modeling*. Tech. rep. PNNL-15870 Rev. 1. Pacific Northwest National Laboratory, 2011-03. DOI: `10.2172/1023125`.

[82] DIN. *DIN 25413-1:2013-04: Classification of shielding concretes by proportion of elements - Part 1: Neutron shielding*. 2013.

[83] Byungho Jung. "PWR structures activation forecasts using Monte Carlo neutron transport simulations". MSc Thesis. ETH Zürich, 2018.

[84] Manuel Pantelias and Benjamin Volmert. "Activation Neutronics for a Swiss Pressurized Water Reactor". In: *Nuclear Technology* 192.3 (2015-12), pp. 278–285. DOI: `10.13182/nt15-13`.

[85] Ben Volmert et al. "MCNP neutron streaming investigations from the reactor core to regions outside the reactor pressure vessel for a Swiss PWR". In: *Progress in Nuclear Science and Technology* 4 (2014), pp. 481–485. DOI: `10.15669/pnst.4.481`.

[86] Valentyn Bykov, Ben Volmert, and Andreas Pautz. "Enhancement and Validation of BWR MCNP Activation Simulations for Swiss Decommissioning Planning". In: *Proceedings of ANS Student Conference 2015*. 2015.

[87] Paolo Pisano. "Application and Validaiton the Nagra Activation Calculation Methodology to the Beznau NPP and Development of a Packaging Concept for RPV and Internals". MA thesis. EPFL, 2018.

[88] A. Scolaro. "Implementation of the Nagra Activation Calculation Methodology for the Gundremmingen Nuclear Power Plant". MSc Thesis. EPFL, 2016.

[89] Ahmad M. Ibrahim et al. "The Multi-Step CADIS Method for Shutdown Dose Rate Calculations and Uncertainty Propagation". In: *Nuclear Technology* 192.3 (2015-12), pp. 286–298. DOI: `10.13182/nt15-1`.

[90] V. Bykov et al. “Nagra Activation Analysis for the Optimization of NPP Decommissioning and Component Segmentation Strategy”. In: *Proceedings of the PHYSOR 2018 Conference*. 2018, pp. 2227–2237.

[91] D. Cokinos et al. *Pressure-Vessel-Damage Fluence Reduction by Low-Leakage Fuel Management*. Tech. rep. Brookhaven National Lab., 1983-01-01.

[92] Scott W. Mosher. *ADVANTG – An Automated Variance Reduction Parameter Generator*. ORNL/TM-2013/416. Oak Ridge National Lab, 2013.

[93] W. A. Wieselquist. “The SCALE 6.2 ORIGEN API for High Performance Depletion”. In: *Proceedings of the M&C 2015 Conference*. 2015-01.

[94] Hank Childs et al. “VisIt: An end-user tool for visualizing and analyzing very large data”. In: *High performance visualization–enabling extreme-scale scientific insight* (2012), pp. 357–372.

[95] Valentyn Bykov. *Activation Analysis of KKM*. Tech. rep. NAB 18-16 Rev. 1. Nagra, 2018-12.

[96] Silvano Martello and Paolo Toth. *Knapsack Problems: Algorithms and Computer Implementations (Wiley Series in Discrete Mathematics and Optimization)*. Wiley, 1990. ISBN: 0471924202.

[97] David Pisinger and Jens Egeblad. *Heuristic approaches for the two- and three-dimensional knapsack packing problems*. Tech. rep. 2006/13. Datalogisk Institut, University of Copenhagen, 2006.

[98] Bernard T. Han, George Diehr, and Jack S. Cook. “Multiple-type, two-dimensional bin packing problems: Applications and algorithms”. In: *Annals of Operations Research* 50.1 (1994-12), pp. 239–261. DOI: 10.1007/bf02085642.

[99] Python Software Foundation. *Python Programming Language, version 3.7*. 2018. URL: https://www.python.org (visited on 2018-08-01).

[100] B. Bitterli, D. Braun, and W. Hummel. “Core-Schrott-Konditionierung im Kernkraftwerk Gösgen (COSKO)”. In: *Proceedings of KONTEC 2007*. 2007.

[101] X-5 Monte Carlo Team. *MCNP - A General N-Particle Transport Code, Version 5*. LA-CP-03-0245. 2003.

[102] Lianyan Liu and Robin P. Gardner. “A Geometry-Independent Fine-Mesh-Based Monte Carlo Importance Generator”. In: *Nuclear Science and Engineering* 125.2 (1997-02), pp. 188–195. DOI: 10.13182/nse97-a24265.

[103] John C. Wagner and Alireza Haghighat. “Automated Variance Reduction of Monte Carlo Shielding Calculations Using the Discrete Ordinates Adjoint Function”. In: *Nuclear Science and Engineering* 128.2 (1998-02), pp. 186–208. DOI: 10.13182/nse98-2.

[104] G. I. Bell and S. Glasstone. *Nuclear Reactor Theory*. 1970-10.

[105] James J. Duderstadt and E. Hamilton. *Nuclear Reactor Analysis*. John Wiley & Sons, Inc., 1976-01-02. 672 pp. ISBN: 0471223638.

[106] John C. Wagner, Douglas E. Peplow, and Scott W. Mosher. "FW-CADIS Method for Global and Regional Variance Reduction of Monte Carlo Radiation Transport Calculations". In: *Nuclear Science and Engineering* 176.1 (2014-01), pp. 37–57. DOI: `10.13182/nse12-33`.

[107] Manuel Pantelias and Scott W. Mosher. "Monte-Carlo, Hybrid and Deterministic Calculations for the Activation Neutronics of Swiss LWRs". In: *Transactions of the American Nuclear Society* 109 (2013).

[108] E. Vlassopoulos et al. "Neutron Streaming Investigations with Classic and Hybrid Monte Carlo Variance Reduction Methods for the AGN-211-P Research Reactor in Basel". In: *Proceedings of the PHYSOR 2016 conference*. 2016.

[109] K. D. Lathrop. "Ray Effects in Discrete Ordinates Equations". In: *Nuclear Science and Engineering* 32.3 (1968-06), pp. 357–369. DOI: `10.13182/nse68-4`.

[110] Thomas Booth. *MCNP Slope Estimate Discussion*. Tech. rep. Los Alamos National Laboratory, 2006-03. DOI: `10.13140/RG.2.2.16836.42880`.

[111] T. E. Booth, K. C. Kelley, and S. S. McCready. "Monte Carlo Variance Reduction Using Nested Dxtran Spheres". In: *Nuclear Technology* 168.3 (2009-12), pp. 765–767. DOI: `10.13182/nt09-a9303`.

[112] B. Volmert et al. "Validation of MCNP NPP Activation Simulations for Decommissioning Studies by NPP Neutron Activation Foil Measurement Campaigns". In: *Proceedings of the 15th International Symposium on Reactor Dosimetry (ISRD-15)*. 2014.

[113] Yiman Yan. "An MCNP Generic Sample Activation Model for Validation of the Nagra NPP Activation Methodology". MSc Thesis. EPFL, 2013-07.

[114] Manuel Pantelias and Ben Volmert. "Activation Neutronics for a Swiss PWR: Simulations and Validation". In: *Proceedings of 18th Topical Meeting on the Radiation Protection & Shielding Division of ANS (ANS RPSD 2014)*. 2014.

[115] Manuel Pantelias, Valentyn Bykov, and Benjamin Volmert. "Activation Neutronics for a Swiss PWR and BWR". In: *Proceedings of the ANS Annual Meeting 2015*. 2015.

[116] Ben Volmert, Miguel Morales, and Valentyn Bykov. *Aktivierungsrechnungen für den Basler Forschungsreaktor AGN-211-P - Phase 1: Ergebnisse vor der Gesamt-Validierung durch radiologische Messungen*. Tech. rep. NPB 16-07. Nagra, 2016.

[117] J. Thiess. *Demontage und Rückbau der Reaktoranlage AGN-211-P: Probenahme- und Meßprogramm*. Tech. rep. AGN_IGN_DD0_PM16_A02. IGN, 2016-11-30.

[118] J. Eikenbeg. *Prüfbericht: Materialproben Universitätsreaktor – Nuklidspezifische Analyse, Beta, Gamma*. Tech. rep. EJ96-2016-550. PSI, 2016-09-15.

[119] Huntsman Advanced Materials Americas. *Material Safety Data Sheet ARALDITE 2014 A US*. 2011-09-22.

[120] Ben Volmert, Miguel Morales, and Valentyn Bykov. *Aktivierungsrechnungen für den Basler Forschungsreaktor AGN-211-P - Phase 2: Konsolidierte Ergebnisse nach Einbezug der radiologischen Messdaten*. Tech. rep. NPB 17-10. Nagra, 2017.

[121] ENSI. *Gutachten zum Stilllegungsprojekt des Reaktors AGN-211-P der Universität Basel*. Tech. rep. ENSI 23/1120. ENSI, 2018-04-17.

[122] Richard L. Holm. "Decommissioning the University of Illinois Nuclear Research Laboratory". In: *Journal of Nuclear Energy Science & Power Generation Technology* s1.01 (2013). DOI: `10.4172/2325-9809.s1-004`.

[123] K. E. Taylor and R. L. Holm. "A Multi-Phased Sampling Effort to Characterize a University TRIGA Research Reactor". In: *Proceedings of the WM'06 Conference*. 2006. URL: `http://www.wmsym.org/archives/2006/prof6251.html` (visited on 2018-09-28).

[124] G. Gestermann. "MOSAIK 20 Years of Experience with a Cask System for Transportation, Conditioning and Storage of Radioactive Waste". In: *Proceedings of the 14th Int. Symp. on the Packaging and Transportation of Radioactive Materials*. 067. 2004.

[125] S. Fromknecht and R. Borsutzky. *Entwicklung von Lagerbehältern aus Beton: Lagerbehälter LC-86*. Tech. rep. LC86/10.02. Hochtief, 2017-11-07.

[126] Leica Geosystems. *Cyclone pointcloud export format - Description of ASCII .ptx format*. 2015-04-29. URL: `https://w3.leica-geosystems.com/kb/?guid=5532D590-114C-43CD-A55F-FE79E5937CB2` (visited on 2018-09-28).

[127] H. Ferroukhi et al. "Towards a reference numerical scheme using MCNPX for PWR control rod tip fluence estimations". In: *Proceedings of the PHYSOR 2012 Conference*. American Nuclear Society. 2012-04.

[128] A. Vasiliev et al. "Nuclear Data Library Effects on Fast to Thermal Flux Shapes Around PWR Control Rod Tips". In: *Nuclear Data Sheets* 118 (2014), pp. 575–578. ISSN: 0090-3752. DOI: `10.1016/j.nds.2014.04.139`.

[129] Grove Software. *MicroShield Version 11*. 2013. URL: `http://radiationsoftware.com/wp-content/uploads/2013/06/mshielddesc2.pdf`.

[130] IAEA. *Control assembly materials for water reactors: Experience, performance and perspectives*. Tech. rep. IAEA-RECDOC-1132. IAEA, 2000-02. URL: `https://www-pub.iaea.org/MTCD/Publications/PDF/te_1132_prn.pdf` (visited on 2018-09-19).

[131] C. Ware. "Color sequences for univariate maps: theory, experiments and principles". In: *IEEE Computer Graphics and Applications* 8.5 (1988-09), pp. 41–49. DOI: `10.1109/38.7760`.

[132] David Borland and Russell M. Taylor Ii. "Rainbow Color Map (Still) Considered Harmful". In: *IEEE Computer Graphics and Applications* 27.2 (2007-03). Ed. by Theresa-Marie Rhyne, pp. 14–17. ISSN: 0272-1716. DOI: `10.1109/MCG.2007.323435`.

[133] Adam Light and Patrick J. Bartlein. “The end of the rainbow? Color schemes for improved data graphics”. In: *Eos, Transactions American Geophysical Union* 85.40 (2004), p. 385. DOI: `10.1029/2004eo400002`.

[134] B. E. Rogowitz and L. A. Treinish. “Data visualization: the end of the rainbow”. In: *IEEE Spectrum* 35.12 (1998-12), pp. 52–59. DOI: `10.1109/6.736450`.

[135] Josef Albers. *Interaction of Color*. Yale University Press, 2013. 144 pp. ISBN: 978-0300179354.

[136] Hazel Rossotti. *Colour: Why the World Isn’t Grey*. Princeton University Press, 1985. ISBN: 0-691-02386-7.

[137] David Briggs. *The dimensions of colour*. 2007. URL: `http://www.huevaluechroma.com` (visited on 2018-08-01).

[138] Bang Wong. “Points of view: Color blindness”. In: *Nature Methods* 8.6 (2011-06), pp. 441–441. DOI: `10.1038/nmeth.1618`.

[139] Hans Brettel, Françoise Viénot, and John D. Mollon. “Computerized simulation of color appearance for dichromats”. In: *Journal of the Optical Society of America A* 14.10 (1997-10), p. 2647. DOI: `10.1364/josaa.14.002647`.

[140] Colin Ware. *Information visualization: perception for design*. Elsevier, 2012.

[141] Bernice E. Rogowitz and Alan D. Kalvin. “The "Which Blair Project": A Quick Visual Method for Evaluating Perceptual Color Maps”. In: *Proceedings of the Conference on Visualization ’01*. VIS ’01. San Diego, California: IEEE Computer Society, 2001, pp. 183–190. ISBN: 0-7803-7200-X. URL: `http://dl.acm.org/citation.cfm?id=601671.601699`.

[142] Matthew Anderson et al. “Proposal for a Standard Default Color Space for the Internet–sRGB”. In: *Proceedings of the 4th Color and Imaging Conference*. Society for Imaging Science and Technology, 1996.

[143] K. E. Higgins et al. “Spatial contrast sensitivity: Importance of controlling the patient’s visibility criterion”. In: *Archives of Ophthalmology* 102.7 (1984), pp. 1035–1041. DOI: `10.1001/archopht.1984.01040030837028`.

[144] Jyrki Rovamo, Rauli Franssila, and Risto Näsänen. “Contrast sensitivity as a function of spatial frequency, viewing distance and eccentricity with and without spatial noise”. In: *Vision Research* 32.4 (1992), pp. 631–637. ISSN: 0042-6989. DOI: `https://doi.org/10.1016/0042-6989(92)90179-M`.

[145] Achim Zeileis, Kurt Hornik, and Paul Murrell. “Escaping RGBland: Selecting colors for statistical graphics”. In: *Computational Statistics & Data Analysis* 53.9 (2009-07), pp. 3259–3270. DOI: `10.1016/j.csda.2008.11.033`.

[146] Reto Stauffer et al. “Somewhere Over the Rainbow: How to Make Effective Use of Colors in Meteorological Visualizations”. In: *Bulletin of the American Meteorological Society* 96.2 (2015), pp. 203–216. DOI: `10.1175/BAMS-D-13-00155.1`.

[147] Reto Stauffer, Jason C. Fisher, and Achim Zeileis. *Graphical User Interface for Choosing HCL Color Palettes*. Ed. by Reto Stauffer. 2016. URL: `http://hclwizard.org/hclwizard/` (visited on 2018-08-01).

[148] D. A. Green. "A colour scheme for the display of astronomical intensity images". In: *Bulletin of the Astronomical Society of India* 39 (2011-03), pp. 289–295.

CURRICULUM VITAE

Valentyn Bykov

https://orcid.org/0000-0003-4726-1868
@ valentyn@vbykov.eu

WORK EXPERIENCE

Current
2016

Nagra
Nuclear Engineer
Working on further development of the Nagra Activation Analysis Methodology, radiation transport calculations for dose rate and criticality assessments, setup and maintenance of the unit's computational workstations and the associated network components, supervision and training of MSc students and interns.

2016

Oak Ridge National Laboratory
Visiting Scientist
Implementation of the activation code sequence MSX for decommissioning waste characterization.

2014-2016

Paul Scherrer Institute
PhD Student
PhD-affiliated work, including depletion calculations with CASMO and SIMULATE.

2013-2016

Nagra
Intern, MSc Thesis Student, PhD Student
Development of Nagra NPP models, radiation transport calculations for dose rate assessments.

2011-2012

Nuclear Chemistry Research at the Univeristy of Illinois
Research Assistant
Researcher, co-author of publications, funding proposals and a patent application, working on CRUD removal in Chemical & Volume Control System, under prof. Barclay Jones.

2009-2011

Nuclear Materials Research at the Univeristy of Illinois
Research Assistant
Laboratory assistant, trained to perform X-ray reflectivity and diffraction, including data analysis, working on material analysis of thin uranium films (Nuclear Energy Research Initiative research), under Prof. Brent Heuser.

EDUCATION

2014-2018 PhD in Energy
Swiss Federal Institute of Technology in Lausanne
Thesis title: High Fidelity Determination of Nuclide Inventories for Decommissioning and Radioactive Waste Disposal.

2012-2014 MSc in Nuclear Engineering
Swiss Federal Institute of Technology in Zürich
Thesis title: Enhancement and Validation of the NPP Mühleberg MCNP Activation Simulations for Swiss Decommissioning Planning.

2008-2012 BSc in Nuclear, Plasma, and Radiological Engineering
University of Illinois at Urbana–Champaign
Thesis title: *Hannah*: Highly Enriched Uranium NaK Modular Reactor.

SKILLS

Nuclear Codes

- **Monte Carlo**: MCNP, Serpent
- **Variance Reduction**: ADVANTG
- **Fuel Depletion**: CASMO/SIMULATE, TRITON, Polaris
- **Basic Shielding**: Microshield

Programming

- Python
- MATLAB
- C

Languages

- **English** Fluent / Native-Like
- **Czech** Fluent / Native-Like
- **Russian** Fluent
- **German** Intermediate (Goethe C1 Diploma)

LIST OF PUBLICATIONS

- **V. Bykov**, S. Mosher, B. Volmert, A. Scolaro, M. Pantelias, A. Pautz "Nagra Activation Analysis for the Optimization of NPP Decommissioning and Segmentation Strategy." Proc. PHYSOR 2018, Cancun, Mexico, April 22 – 26, 2018 (CD-ROM).
- **V. Bykov**, A. Vasiliev, H. Ferroukhi, A. Pautz "Solution of the BEAVRS benchmark using CASMO-5 / SIMULATE-5 code sequence." Proc. PHYSOR 2016, Sun Valley, Idaho, USA, May 1 – 5, 2016 (CD-ROM).
- E. Vlassopoulos, **V. Bykov**, D. Siefman, B. Volmert, M. Pantelias. "Neutron Streaming Investigations with Classic and Hybrid Monte Carlo Variance Reduction Methods for the AGN-211-P Research Reactor in Basel." Proc. PHYSOR 2016, Sun Valley, Idaho, USA, May 1 – 5, 2016 (CD-ROM).
- **V. Bykov**, B. Volmert, A. Pautz. "Enhancement and Validation of BWR MCNP Activation Simulations for Swiss Decommissioning Planning." ANS 2015 Student Conference.
- **V. Bykov**. "Enhancement and Validation of the NPP Mühleberg MCNP Activation Simulations for Swiss Decommissioning Planning." MSc Thesis, ETH Zurich. 2014. http://dx.doi.org/10.3929/ethz-a-010261946.
- M. Pantelias, **V. Bykov** and B. Volmert, "Activation Neutronics for a Swiss PWR and BWR", American Nuclear Society Annual Meeting 2015, San Antonio, TX, USA, June 7-11, 2015
- **V. Bykov**, J. Křepel, A. Pautz. "Molten Salt Fast Reactor Blanket Design and Proliferation Resistance Assessment." Proc. ASME ICONE22 45950, vol. 5, V005T17A061, July 07, 2014. ICONE22-31026.
- J. Křepel, **V. Bykov**, K. Mikityuk, B. Hombourger, C. Fiorina, A. Pautz. "Molten Salt Reactor with Simplified Fuel Recycling and Delayed Carrier Salt Cleaning." Proc. ASME ICONE22 45936, vol. 3, V003T05A015, July 07, 2014. ICONE22-30396.